SLAC-124
UC-34
(EXP)

NEUTRAL PION AND ETA PHOTOPRODUCTION FROM HYDROGEN AT HIGH ENERGIES

JAMES R. JOHNSON

STANFORD LINEAR ACCELERATOR CENTER
STANFORD UNIVERSITY
Stanford, California 94305

PREPARED FOR THE U.S. ATOMIC ENERGY
COMMISSION UNDER CONTRACT NO. AT(04-3)-515

September 1970

ABSTRACT

Measurements have been made of the process $\gamma p \rightarrow \pi^o p$ for photon energies from 4 to 18 GeV and four-momentum transfers t between -0.1 and -1.4 $(GeV/c)^2$. The reaction $\gamma p \rightarrow \eta p$ has been studied between 4 and 9 GeV for t-values from -0.3 to -1.4 $(GeV/c)^2$.

The experiment was carried out at the Stanford Linear Accelerator Center (SLAC) by passing the SLAC photon beam through a target containing gaseous hydrogen for small momentum transfers and liquid hydrogen for higher t-values. The recoil protons were analyzed and detected in the SLAC 1.6 GeV/c spectrometer, and the "missing mass" of the neutral product was calculated from kinematics.

π^o photoproduction cross sections decrease rapidly with increasing $|t|$ beyond $|t| = 0.1$, show a local minimum or "dip" around $|t| = 0.5$ and a secondary maximum for $|t| \approx 0.85$, then fall off smoothly out to $|t| = 1.4$. The energy dependence appears close to E_0^{-2}, becoming only gradually steeper with increasing $|t|$, contrary to some theoretical predictions. The energy dependence of η production is consistent with E_0^{-2}, but the t-dependence shows only a smooth decrease with $|t|$ and no sign of a dip at $t=-0.5$ $(GeV/c)^2$. A simple t-channel exchange model cannot then explain both processes with the same assumptions, even though the quantum numbers of the two mesons are the same except for isospin.

ACKNOWLEDGEMENTS

I would like to thank Dr. David M. Ritson for supervising this stage of my education in physics. His patience and individual attention as my adviser are much appreciated. In addition, I learned a great deal by working with Drs. Robert Anderson, Roy Weinstein, and Bjorn Wiik, and I am grateful for their encouragement.

The large-scale experiment described in this thesis required the efforts of a considerable number of people. The physicists and graduate students involved, at various times and to various degrees, included R. Anderson, D. Gustavson, I. Overman, D. Ritson, B. Wiik, and myself of the Stanford Linear Accelerator Center; W. G. Jones and D. Kreinick from the California Institute of Technology; F. Murphy from the University of California, Santa Barbara; R. Weinstein and M. Gettner from Northeastern University; R. Talman from Cornell University; D. Worcester from Harvard University; and J. Walker from the National Accelerator Laboratory. Technical support was provided by SLAC staff members, particularly technicians J. Grant, J. Escalera, J. Schroeder, D. McShurley, and A. Filippi; A. Golde and the end-station crew; and the Spectrometer Facilities Group.

I wish to thank Mrs. Barbara Ault for her help in preparing this thesis, and the National Science Foundation for four years of financial support. The experiment itself was supported by the U. S. Atomic Energy Commission.

TABLE OF CONTENTS

LIST OF TABLES

LIST OF FIGURES

I. INTRODUCTION

Experiments on the interactions of elementary particles have been carried out at ever-increasing center-of-mass energies since the first particle accelerators were developed. As each energy range is studied, interest shifts to the next higher band, and larger machines are built to look for changes in the behavior of the interactions. The two-mile-long, 20 GeV Stanford linear accelerator presently represents the culmination of this trend for the study of electron- and photon-induced interactions: it is presently the highest-energy, highest-current electron accelerator, and photon beams of comparable energy produced at proton synchrotrons are of much lower intensity.

In the energy range of the SLAC machine one can do a number of experiments for which there are (or once were) comparatively firm theoretical predictions. In particular, the currently important theory of Regge poles (Ref. 1), which attempts to interpret particles and resonances as originating from poles in the complex angular momentum plane, predicts certain simple behavior for scattering amplitudes at energies large compared to the mass of the proton. For example, the energy dependence is expected to be approximately $\frac{d\sigma}{dt} \sim E_0^{2\alpha(t)-2}$, where $\alpha(t)$ gives the Regge poles in the particular amplitude, E_0 is the beam energy, and t is the square of the four-momentum transfer. For π^o and η photoproduction, t-channel exchange is expected to dominate at high energies, and since π^o and η are even under charge conjugation and the photon is odd, the exchanged particle must be odd under C. Thus only ρ^o, ω, ϕ or B^o mesons can contribute, and from comparison of the coupling constants the ω should dominate π^o photoproduction and ρ^o exchange should be strongest in the case of the η. Given that $\alpha(t)$ is similar for ρ^o and ω, one might expect the two processes to be similar and to resemble $\pi^- p \rightarrow \pi^o n$ charge-exchange

scattering, for which only ρ exchange is permitted. Thus $d\sigma/dt$ versus t should show a sharp dip or local minimum at $t \approx -0.5$ $(GeV/c)^2$ and strong shrinkage of the forward peak with increasing energy (Ref. 2).

It was desired to check these predictions at SLAC energies. Previous to this experiment, very little was known about η photoproduction above 2 GeV although results have since been reported (Ref. 3). Measurements of forward π^o photoproduction had been made at the Deutsches Electronen-Synchrotron (DESY) (Ref. 4) and the Cambridge Electron Accelerator (CEA) (Ref. 5) between 2 and 5.8 GeV. The π^o results were reasonably consistent with the model described above. This experiment now provides a single consistent set of measurements of π^o photoproduction at energies up to 18 GeV for t-values between -0.1 and -1.4 $(GeV/c)^2$, and of η photoproduction up to 9 GeV for t between -0.3 and -1.4 $(GeV/c)^2$.

The experiment was performed using the conventional SLAC photon beam: the primary electron beam produced bremsstrahlung on passing through a thin sheet of aluminum, the remaining electrons were deflected away by sweeping magnets, and the photons continued through collimators to the hydrogen target. The photon flux was measured by various monitors which were calibrated periodically against a calorimeter. Protons recoiling from the hydrogen target were analyzed in momentum and production angle by the SLAC 1.6 GeV/c magnetic spectrometer. Cross sections were determined by fixing the spectrometer momentum, varying the observed proton angle, and noting the change in proton yield at threshold for photoproduction of π^o or η. ρ^o and ϕ cross sections were also measured (Ref. 6) but are not reported as part of this thesis.

The experimental resolution was not sufficient to separate π^o photoproduction from proton Compton scattering, $\gamma p \rightarrow \gamma p$. A separate but closely related

experiment was done to measure the Compton cross sections, by making a coincidence between the 1.6 GeV/c spectrometer and a shower counter to detect the scattered photon (Ref. 7). Although interesting in its own right, this measurement will be treated, for the purposes of this thesis, simply as a correction to the π^0 results. Basic features of the experiment will be mentioned, where appropriate, in what follows.

II. APPARATUS

A. Beam Line

1. SLAC

The Stanford Linear Accelerator is described in detail in Ref. 8. It is basically made up of pieces of cylindrical copper waveguide arranged in a straight line approximately 10,000 feet in length. Power from a number of large klystron tubes is fed into the waveguide; the cavity is so designed as to propagate an electromagnetic wave mode having a longitudinal electric field component and a phase velocity equal to that of light (c). Electrons are accelerated along the waveguide by the electric field and very quickly attain (due to their low mass) a velocity negligibly different from c, after which they remain in phase with the wave and continue to gain energy at up to 2 MeV per foot traveled. Due to limitations on the klystron power output, and heat dissipation problems, the machine is not run continuously but rather in short bursts or pulses, each approximately 1.6 microseconds long, at 360 per second.

The accelerator, as presently operated, is capable of a maximum output energy of slightly over 20 GeV and a maximum average electron current in the machine of approximately 30 microamperes. The high intensity makes it possible to measure small cross sections in a reasonable length of time, but also puts stringent requirements on the experimental apparatus: since up to several hundred kilowatts of beam power may be brought into the experimental area, the beam transport system, targets, and beam monitors must be designed to handle large amounts of heat without affecting their performance, and the entire area must be well shielded to protect personnel. Furthermore, the low duty cycle means that instantaneous beam rates are extremely high, so that counters must be heavily shielded to prevent saturation by room background, and the

resolving times of electronic circuits must be kept very small if the full beam intensity is to be used.

2. Beam transport

The "beam switchyard" is shown schematically in Fig. 1. Collimated electron bunches from the machine are deflected by pulsed magnets (PM1-5) to the different beam lines, in this case the "A" beam. Bending magnets (B10-13) disperse the beam for momentum resolution by a high-power slit (SL-10), and a symmetry quadrupole (Q-12) and second set of bending magnets (B14-17) recombine the beam. Various quadrupoles, not shown, are used for focusing. The energy of the beam is given by magnetic field measurements on the bending magnets. The energy spread is set by the slit, and was 1% for this experiment.

For this experiment, the primary electron beam was converted to a conventional bremsstrahlung photon beam: an aluminum disc, of thickness 0.100 inch (approximately 0.03 radiation length), was placed in the beam at TC-20. Bending magnets (B23-26) deflected the electrons down into a dump (D-11) leaving the radiated photons to continue. A variable high-power water-cooled collimator (C-10) was used to reduce the size of the beam at the target, and to make changes in the beam intensity at the target without touching the accelerator itself. This was followed by a sweeping magnet (B-29) to remove any electrons produced on the jaws. The beam then passed through a secondary tungsten collimator (followed by another sweeping magnet) and finally a lead collimator directly in front of the target, to prevent any beam "halo" from hitting the walls of the target cell. Resulting photon beam intensities at the target were of the order of 10^{12} equivalent quanta per second.

Steering of the beam was checked between data runs by remotely inserting zinc sulphide screens which were then viewed on closed-circuit television.

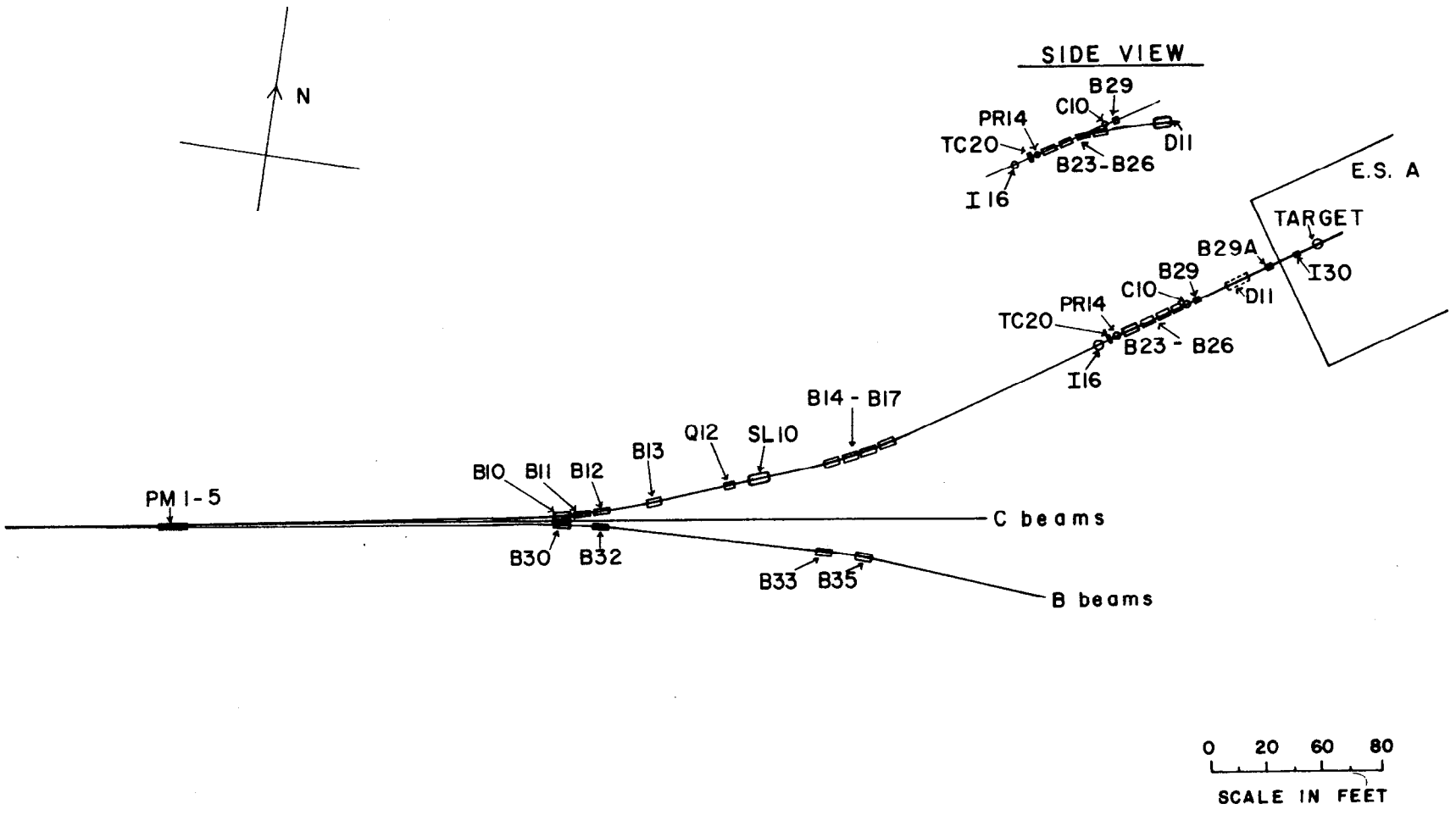

FIG. 1--Basic features of the beam switchyard.

3. Beam monitors

The experimental arrangement in end station "A" is shown in Fig. 2. After passing through the target, the photon beam stopped approximately 100 feet downstream in a nonsaturating secondary-emission quantameter (Ref. 9) labeled SEQ, which was the primary beam monitor. This device is made up of 1/2-inch-thick copper plates alternated with gold-plated aluminum foils 0.0005 inch thick, enclosed in an evacuated steel cylinder; there are 20 copper plates and 19 foils. Several hundred volts are applied to one set, typically the copper plates; then when an incident photon (or electron) produces a shower, secondary emission charge is collected and integrated. To the extent that the whole shower is contained (a few percent is lost at 20 GeV), the SEQ is a total energy device. Cooling water is circulated to the copper plates enabling the device to handle safely a beam power of several kilowatts, with no variation of response with beam intensity. It is also little affected by beam steering, since the effective 8-inch-square aperture is much larger than the incident beam spot size.

As a secondary beam monitor, the SLAC Cerenkov monitor (Ref. 10) was used for a continuous comparison with the SEQ. This device is basically a piece of beam pipe about 4.5 feet long, filled with helium at approximately atmospheric pressure and placed in the beam line upstream of the target. Beam photons materialize in the upstream window (0.005 inch thick aluminum) and Cerenkov light from the pairs is collected by a mirror and directed onto a photomultiplier tube. The output of this tube is then integrated. The ratio of SEQ to Cerenkov charge was normally stable to less than a percent over several hours. Any sudden change was then investigated, and was usually due to the sensitivity of the Cerenkov monitor to beam steering.

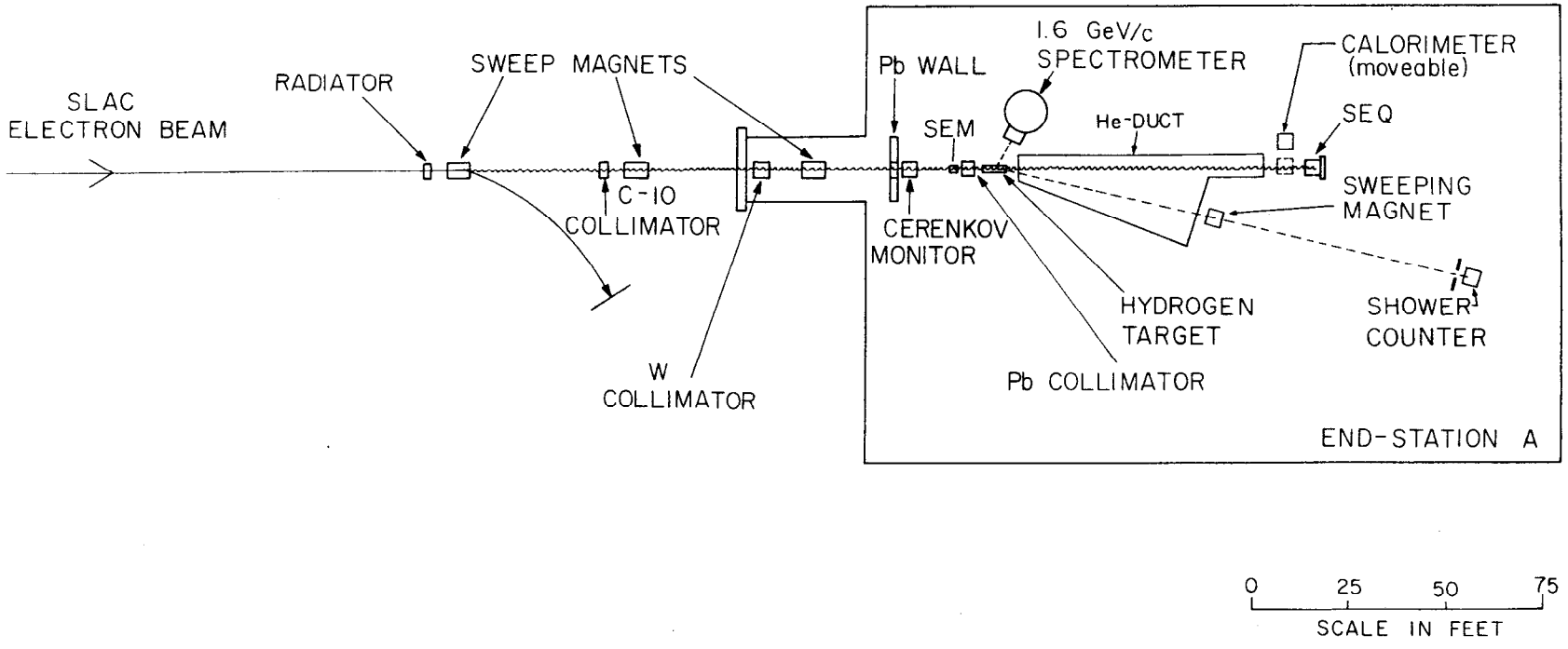

FIG. 2--Experimental arrangement.

From time to time, monitor calibration runs were done with the SLAC silver calorimeter (Ref. 10) moved into the beam. The temperature change of the calorimeter determined the total beam energy incident during the run, and thus the calibration of the Cerenkov monitor. Since the SEQ was blocked by the calorimeter in such a run, its calibration was determined from the Cerenkov constant using the SEQ-to-Cerenkov ratio measured just before and after the calorimeter run. In addition, a direct check was made every time an electron beam was brought into the end station, by comparing the SEQ to the integrated charge on a SLAC precision toroid monitor (Ref. 11) (not shown in Fig. 2) assuming 100% transmission between toroid and SEQ. These calibrations were reproducible to one percent at a given energy over the course of an experimental cycle (two to three weeks) and showed a slight loss of efficiency of the SEQ with increasing beam energy.

Finally, in case of disaster, a thin SEM (secondary-emission monitor) was installed upstream of the target. This is similar in principle to the SEQ, but consists only of seven 0.00025-inch-thick gold-plated aluminum foils, and thus stops only a very small fraction of the beam.

4. Targets

Two separate hydrogen targets were used for this experiment: one contained gaseous hydrogen and was used for measurements at low momentum-transfers, $0.1 \leq |t| \leq 0.4$; the other contained liquid hydrogen and was used for the higher t-values.

A diagram of the liquid target (Ref. 12) is shown in Fig. 3. This is a convectively-cooled device designed for intense SLAC electron beams, and was more than adequate for the photon beams in this experiment. The hydrogen cell was 15 inches long by 2 inches in diameter, with 0.008-inch-thick Mylar walls

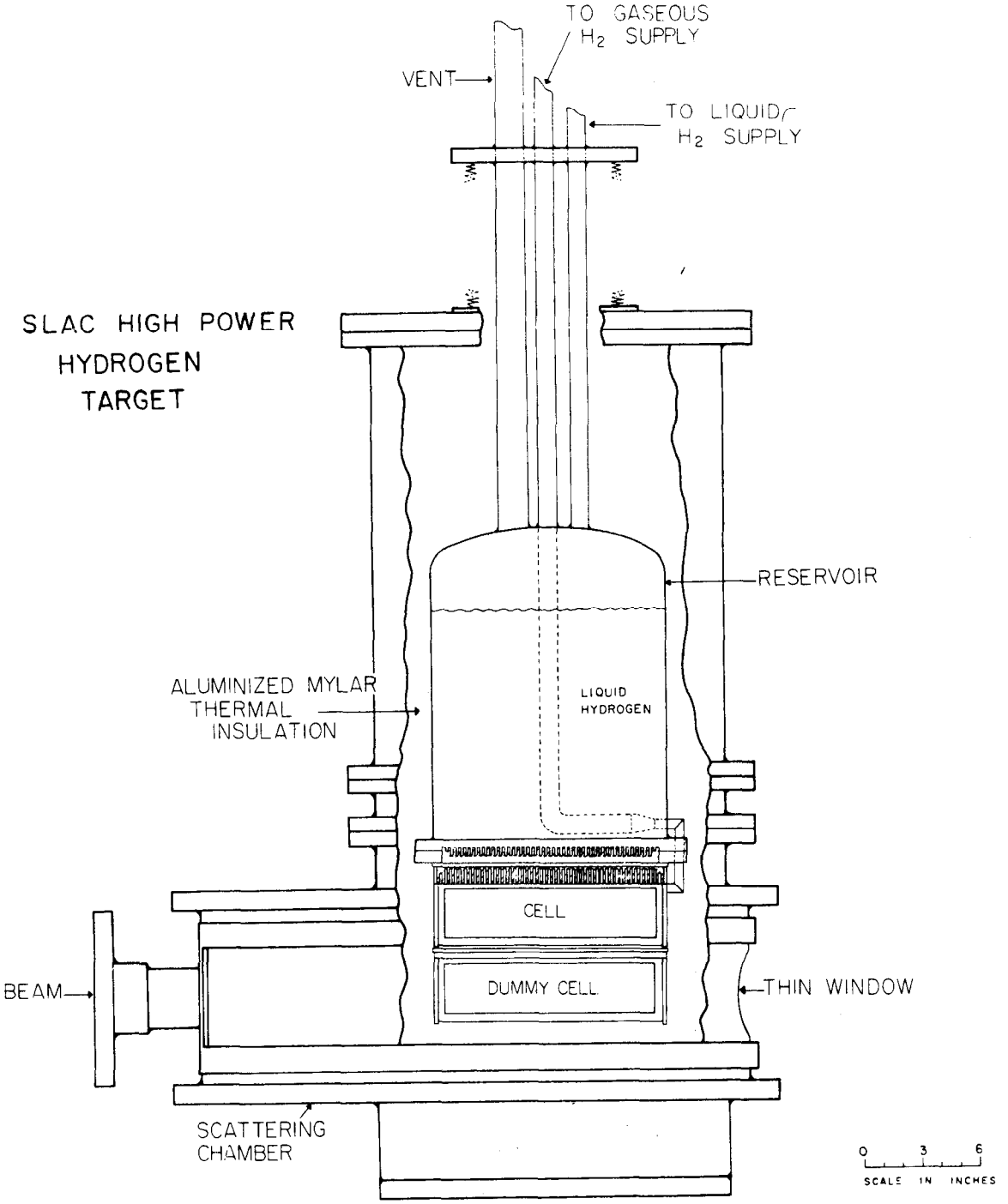

FIG. 3--Liquid hydrogen target.

and 0.005-inch-thick aluminum end windows, and was attached by a finned copper heat exchanger to the bottom of a reservoir of liquid hydrogen (boiling at a pressure of one atmosphere) as a heat sink. This cell was filled from a slightly pressurized supply of hydrogen gas, which then condensed into liquid at the reservoir temperature (20° K). With this arrangement, liquid hydrogen warmed by the photon beam would rise to the heat exchanger and be cooled, setting up convection currents and keeping the whole cell at 20° K. The main limitation on the experiment from this target was the loss of proton angle resolution at small momentum transfers due to multiple scattering in the hydrogen.

The gas target (Ref. 13) is shown schematically in Fig. 4. It was built to reduce the multiple scattering and minimize the energy loss of recoil protons in getting out of the target. The target cell was 25 inches long and 5 inches in diameter, of aluminum, with a 0.01-inch-thick Mylar side exit window. The scattering chamber was connected directly to the spectrometer vacuum, and rotated with the spectrometer on a sliding vacuum seal. To avoid too great a reduction in hydrogen density (and therefore rate) the gas was cooled to 34° Kelvin by a commercial refrigeration unit and filled to a pressure of approximately 120 pounds per square inch. The density thus achieved was 0.01 grams/cm^3, or 1/7 that of liquid hydrogen, and was determined to about 2 percent by filling the known volume of the target cell from a known standard volume of pressurized hydrogen gas and measuring accurately the decrease in pressure of the standard.

Both targets had a dummy cell, as nearly as possible identical to the full cell and mounted directly underneath. A remotely actuated air piston moved the whole cell assembly up and down, enabling the experimenter to choose full cell, dummy cell, or no cell at all, and thus check for background from cell

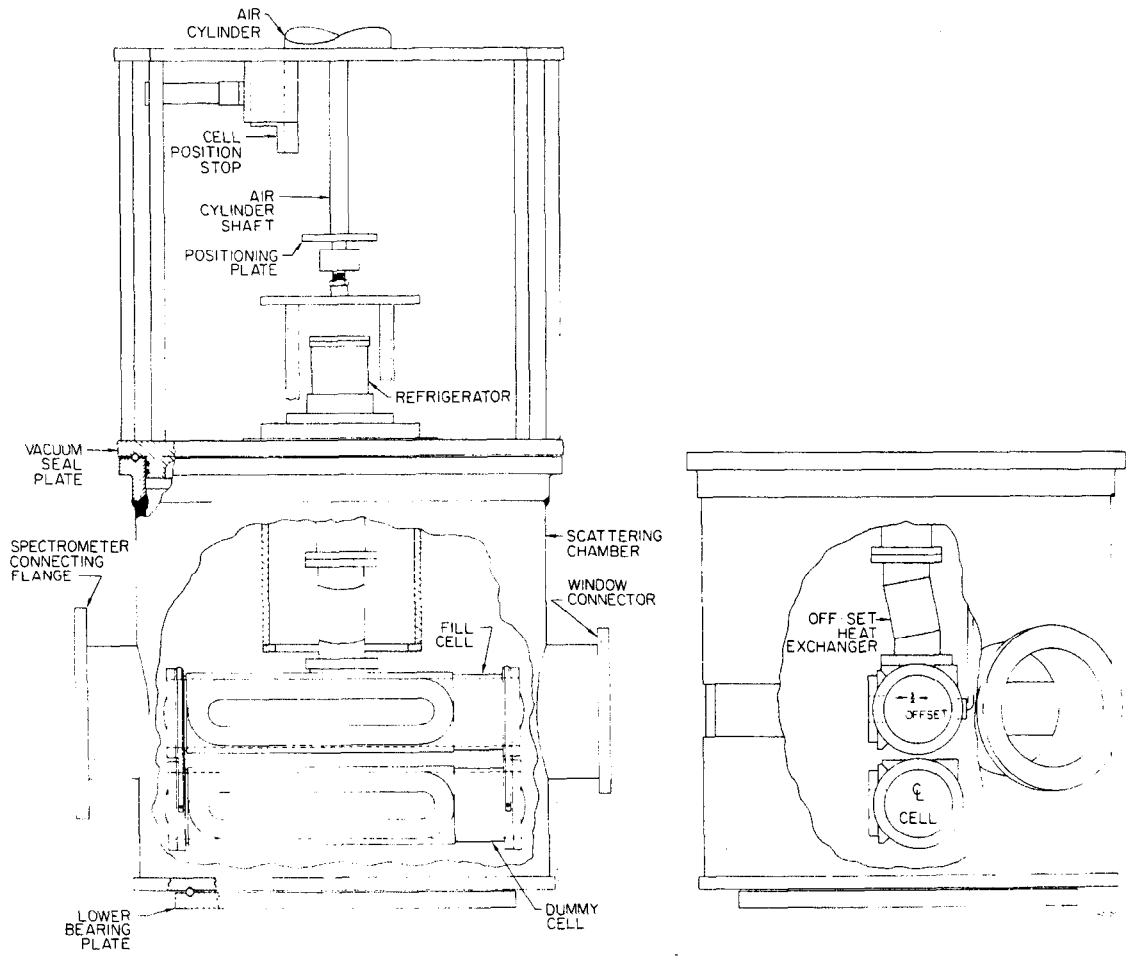

FIG. 4--Gaseous hydrogen target.

walls or other material. To reduce such backgrounds, much of the target assembly was masked from the spectrometer by lead shielding, leaving the cell to be viewed through a horizontal slit two inches high.

B. Detection System

1. Spectrometer

The SLAC 1.6 GeV/c spectrometer (Ref. 14) was, with the exception of the accelerator itself, the largest and most important single piece of apparatus involved in this experiment. A drawing is shown in Fig. 5. It consists of a single 80-ton magnet which deflects charged particles of the right momentum vertically through 90° in a 100-inch radius. A zero gradient (uniform) magnetic field provides weak focusing in the bend plane (momentum focusing), and tilted entrance and exit faces provide parallel-to-point focusing in the non-bend plane (laboratory angle). Second-order correction is produced by shaping of the magnet iron in three "beta lens" regions. By using the TRANSPORT computer program (Ref. 15) the design parameters were chosen so that both momentum and angle of the charged particles are focused in a single plane normal to the central flight path through the spectrometer.

The magnet support pivots about the target table and rides on large steel wheels along a circular rail, driven by electric motors; the position along the rail, and thus the angle of the spectrometer relative to the beam line, can be set and measured to a precision of 0.001°. Particles from the target travel through a vacuum chamber, mounted in the magnet gap, into a counter cave surrounded by 200 tons of concrete shielding, with movable lead access doors. The effective target length viewed by the spectrometer, and the range of azimuthal angles ($\Delta\phi$) accepted, are set by movable horizontal and vertical pairs of lead jaws. Magnet current is provided by a power supply outside the end

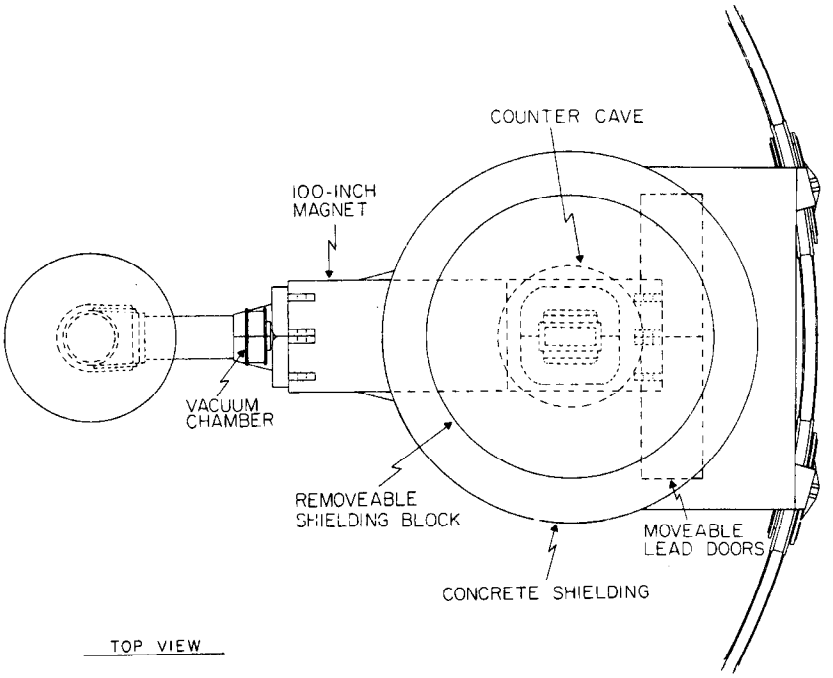

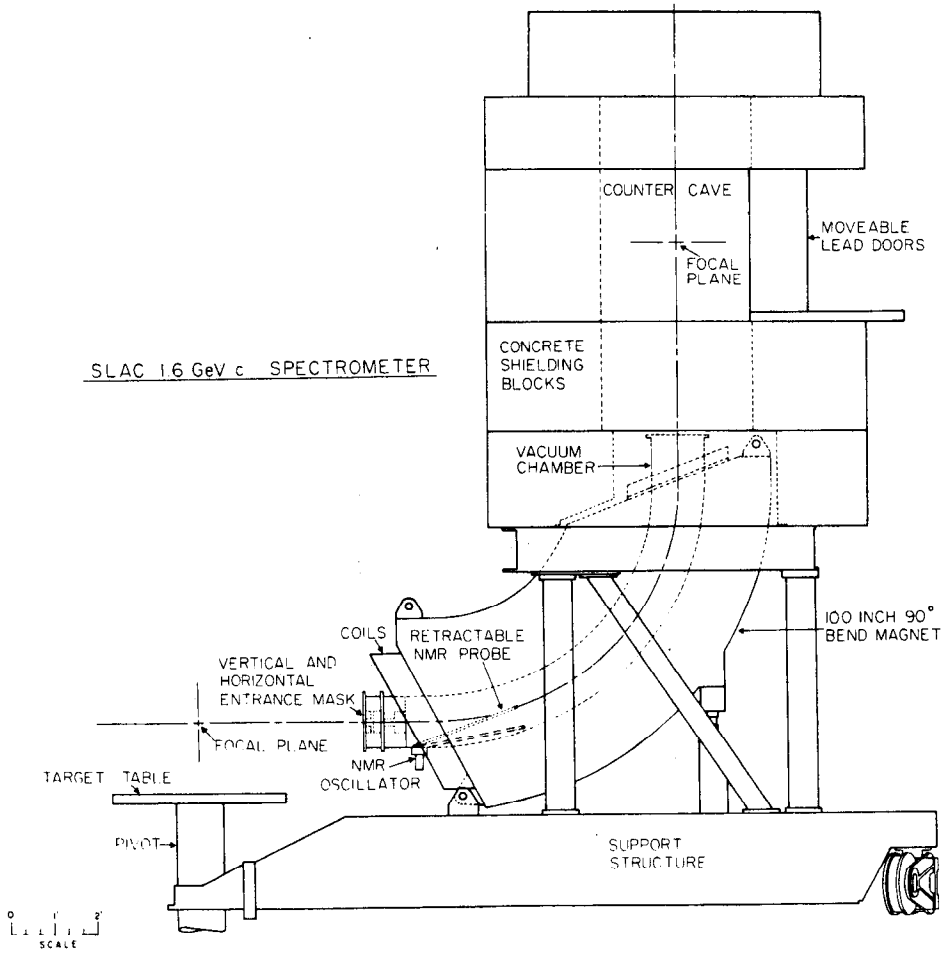

FIG. 5--SLAC 1.6 GeV/c spectrometer.

station, and the magnetic field can be measured to one part in 10^5 using a nuclear magnetic resonance (NMR) system, while a water-cooled shunt in the power supply and a transductor on the magnet leads provide faster but less precise and reproducible settings. A voltmeter gives a quick visual check on polarity and approximate field.

For this experiment, the vertical angular aperture of the spectrometer was set to its maximum value of 59.1 milliradians. The horizontal aperture was 6 inches when using the liquid target and 7 inches for the gas target; the effective target length is then equal to the horizontal aperture divided by the sine of the spectrometer angle. The acceptance in momentum and production angle is defined by the dimensions of the counters in the focal plane and the measured dispersions of the magnet. The total acceptance $\frac{\Delta p}{p} \Delta\Omega$ is independent of spectrometer angle and orientation of the counters in the focal plane. In this case $\frac{\Delta p}{p} \Delta\Omega = 6.8 \times 10^{-5}$ steradian with an uncertainty of ±3%, as determined from earlier experimental measurements of the properties of the magnet, using first a floating wire technique and later a direct electron beam from the accelerator with the spectrometer at 0^o.

2. Counters

The counters used for the liquid-target measurements are shown schematically in Fig. 6. The whole counter assembly could be rotated about the central flight path from the spectrometer. S1 - S13 were scintillation counters made of Pilot B plastic and viewed through lucite light-pipes by photomultiplier tubes (RCA 7850's, except S9 and S10 used the Amperex XP1020). S1 - S8 were hodoscope elements, each 10 inches long by 0.75 inch wide by 0.25 inch thick. S9, S10, and S11 were 0.5-inch-thick backing counters to provide a proton trigger, and so were made large enough to cover the hodoscope for all possible

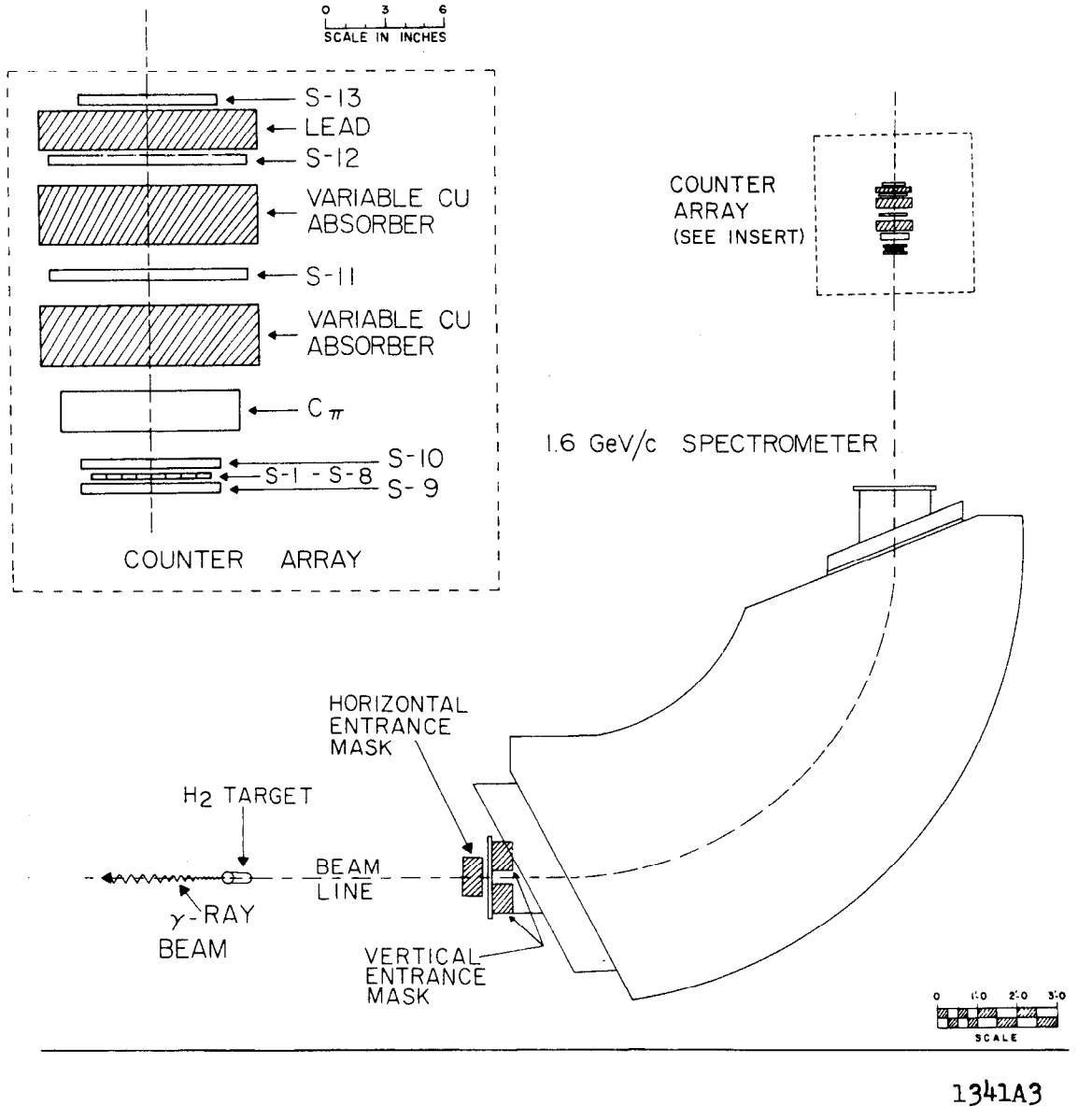

FIG. 6--Counters used with the LH_2 target.

particle flight paths from the spectrometer: S9 and S10 were 7 inches by 11 inches, while S11 was 10 inches by 14 inches. S12 and S13 were 0.5-inch-thick counters placed at the top of the telescope and put in coincidence simply to provide a rate proportional to the pion flux. S12 was 10 inches by 14 inches, and S13 was 6 inches by 10 inches.

The counter labeled C_π was a lucite threshold Cerenkov counter designed to count pions and not protons for momenta between approximately 0.2 and 1.4 GeV/c, so that it could be used as a veto against pions. It consisted of a 9 inch by 13 inch by 2-inch-thick block of lucite, viewed by four high-quantum-efficiency photomultiplier tubes (RCA 8575) the outputs of which were added linearly. It was wrapped in black paper so that light which was not totally internally reflected was not efficiently collected, thus improving the rejection of protons. This counter was found to be approximately 98% efficient for pions, while the efficiency for protons depended on the particular electronic pulse height discrimination level chosen, but was as much as 6% at 1400 MeV/c and approximately 1% or less below 1000 MeV/c.

The lower of the variable copper absorbers shown was not used, but the upper one was set to 3 inches thick to prevent protons from reaching S12 - S13 and counting in the pion monitor. The one-inch-thick plate of lead between S12 and S13 served the same purpose.

Figure 7 shows a diagram of the counters used with the gas target. The most important difference is that counter 9 was replaced by two very thin backing counters 9a and 9b, each 10 inches by 14 inches by 1/32 inch thick Pilot B scintillator viewed from each end by RCA C31000D high-resolution phototubes. This change was made to reduce the range limitation on detecting low-momentum protons. Counter 10 was enlarged to 8 inches by 12 inches and moved farther above the hodoscope to accommodate a thin absorber changer (A-0) and allow

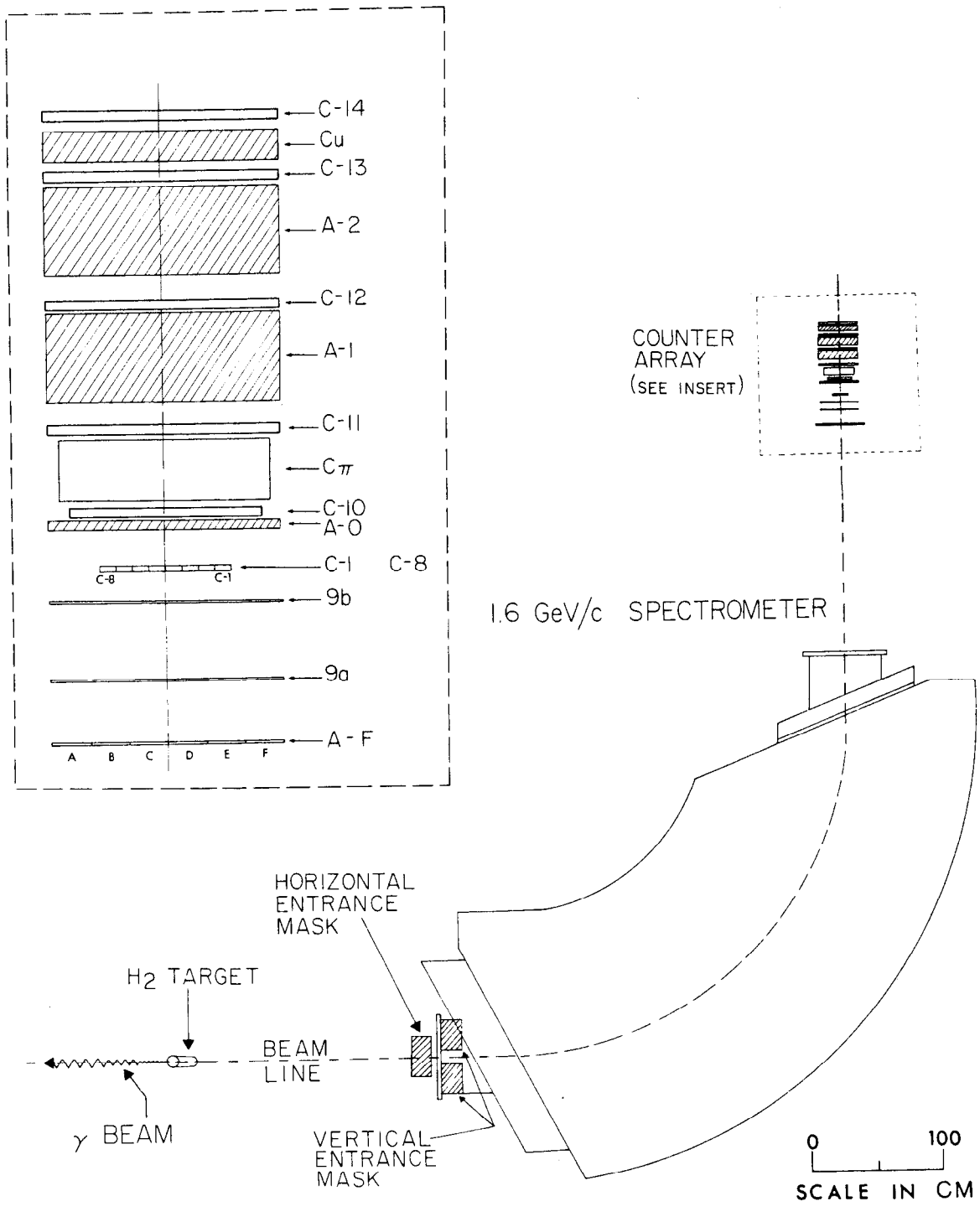

FIG. 7--Counters used with the gas target.

use as a range veto if necessary. Counters 11 and 12 were moved below the variable absorbers A-1 and A-2 respectively, to be a part of the proton telescope for momenta above 500 MeV/c (for which the thin counters did not operate well). A counter 14 was added above (and was identical to) counter 13, and these two provided the pion monitor. There was one inch of copper between them, and A-2 was again set to 3 inches of copper.

The counters labeled A - F were a non-rotatable hodoscope of six thin (1/32 inch) scintillators fixed across the spectrometer momentum direction at the end of the vacuum chamber. Each element was 2.5 inches by 14 inches, constructed like 9a and 9b. They were added (with appropriate relative delays) and put in coincidence with the proton trigger when measuring the Compton effect, to break up the spread in proton flight times through the magnet and allow better time resolution in coincidence with the shower counter detecting the scattered photon.

The shower counter itself was made of 13 pairs of 0.25-inch-thick lead and lucite plates, alternated in a "sandwich" 14 radiation lengths thick with active area 15 inches square. The lucite plates tapered smoothly together outside the active area to form a light pipe. Cerenkov light from a shower was then detected by two 5-inch-diameter Amperex 58AVP photomultiplier tubes, the outputs of which were added linearly. The counter was heavily shielded against room background by lead, paraffin, and several feet of concrete, with an opening toward the target. The opening was adjustable both horizontally and vertically using remotely movable lead jaws, and 3 radiation lengths of carbon (graphite) were placed in front to screen out low energy particles.

The whole shower counter assembly was mounted on a carriage positioned in the end station as shown in Fig. 2. The carriage could be moved along a

steel rail at a 150-foot radius from the target, and remotely controlled jacks were provided to move the assembly up and down. A sweeping magnet, on a similar carriage, was kept in line with the shower counter to deflect away charged particles from the target and vicinity. A helium-filled plastic bag was installed, as shown in the figure, to reduce spray from the beam line and conversion of Compton scattered photons.

3. Electronics and logic

Voltage-divider bases were built for the various photomultiplier tubes according to the manufacturers' suggestions, with some modifications due to local experience. High voltage was provided by power supplies (Ref. 16) capable of up to 3000 volts and 40 milliamperes, with each supply driving up to 12 tubes through a variable distribution box. Phototube pulses were transmitted to the logic system on large 50-ohm coaxial cables.

Figure 8 shows a simplified diagram of the logic used with the liquid hydrogen target; all logic modules (Ref. 17) and scalers (Ref. 18) were 100 Mc units. Pulses from the various counters were fed into discriminator circuits which produced a standard shaped output pulse when the input pulse height exceeded the chosen discrimination level. A variety of coincidence combinations could then be required by other circuits. All important rates were recorded by the fast hardware scalers.

The proton trigger was provided by the coincidence circuit labeled "PROTON", where one could choose any combination of counters 9, 10, 11, and a veto from the coincidence of 9, 10, and C_π. Most of the time the full set $9{:}10{:}11{:}\overline{C_\pi}$ was required. For $|t| \leq 0.4$ $(\mathrm{GeV/c})^2$ the C_π veto was not used, as pulse-height discrimination in the three telescope counters was quite adequate to reject pions: pions are minimum-ionizing at these momenta but the heavier

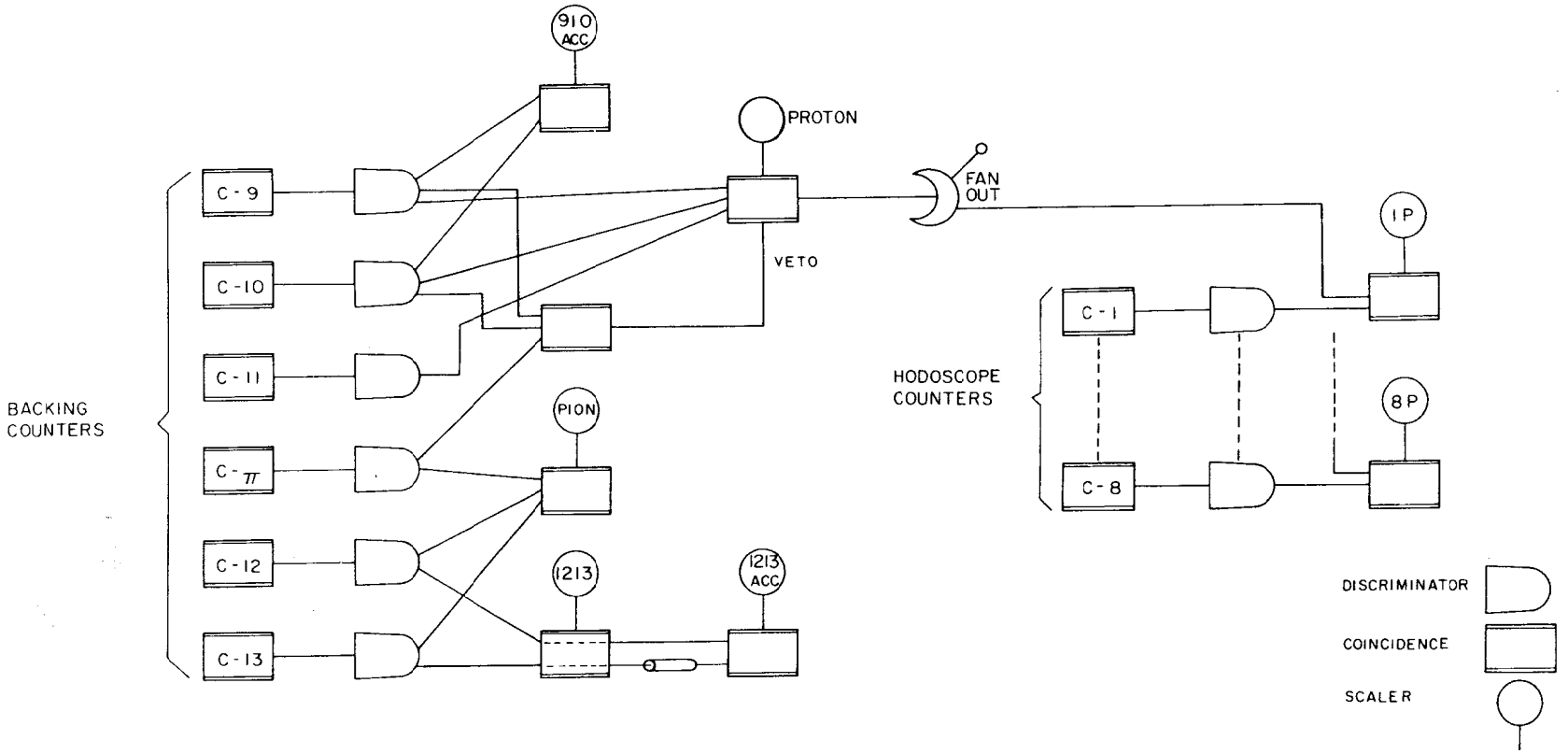

FIG. 8--Basic logic used with the LH_2 target.

protons are not, resulting in larger scintillation pulses from the protons. For $|t| \leq 0.2$ counter 11 could not be used, since the protons did not have enough range to get through C_π. In all cases, the proton trigger was fanned out and used to interrogate the hodoscope, making coincidences labeled 1P - 8P. These rates were then the raw results of the experiment.

C_π was also put in coincidence with counters 12 and 13 to provide a rate (labeled "PION") proportional to the pion flux, as a back-up check on the beam monitors. Certain accidental coincidence rates were determined by deliberately mistiming the input signals to a coincidence circuit; examples are "9:10 ACC" and "12:13 ACC" in the diagram. These rates provided a means of determining losses of counts due to dead time in the circuits.

Figure 9 shows the basic features of the logic used with the gas target, including the additions necessary for measuring proton Compton scattering. The proton logic is similar, except that due to the limited number of inputs on the main proton trigger circuit, a preliminary coincidence was made between 9a, 9b, and 10. The proton signal for $|t| \leq 0.2$ $(GeV/c)^2$ was 9a:9b:10, and was 10:11:12 for $|t| = 0.3$. For $|t| \geq 0.4$ the C_π veto was added, since rates were low and any extra background from pions would have unnecessarily degraded the statistical precision of the measurements.

The Compton trigger, labeled C, was made by a coincidence of the proton trigger with an event in the shower counter, and the accidental rate was monitored by a delayed coincidence labeled "C ACC". Both signals were fanned out to make hodoscope coincidences, shown in the diagram only for the real rate. These provided the raw Compton results. The added "momentum counters" A - F were also in coincidence at "C" and "C ACC" for $|t| \leq 0.3$, but this is not shown in the figure.

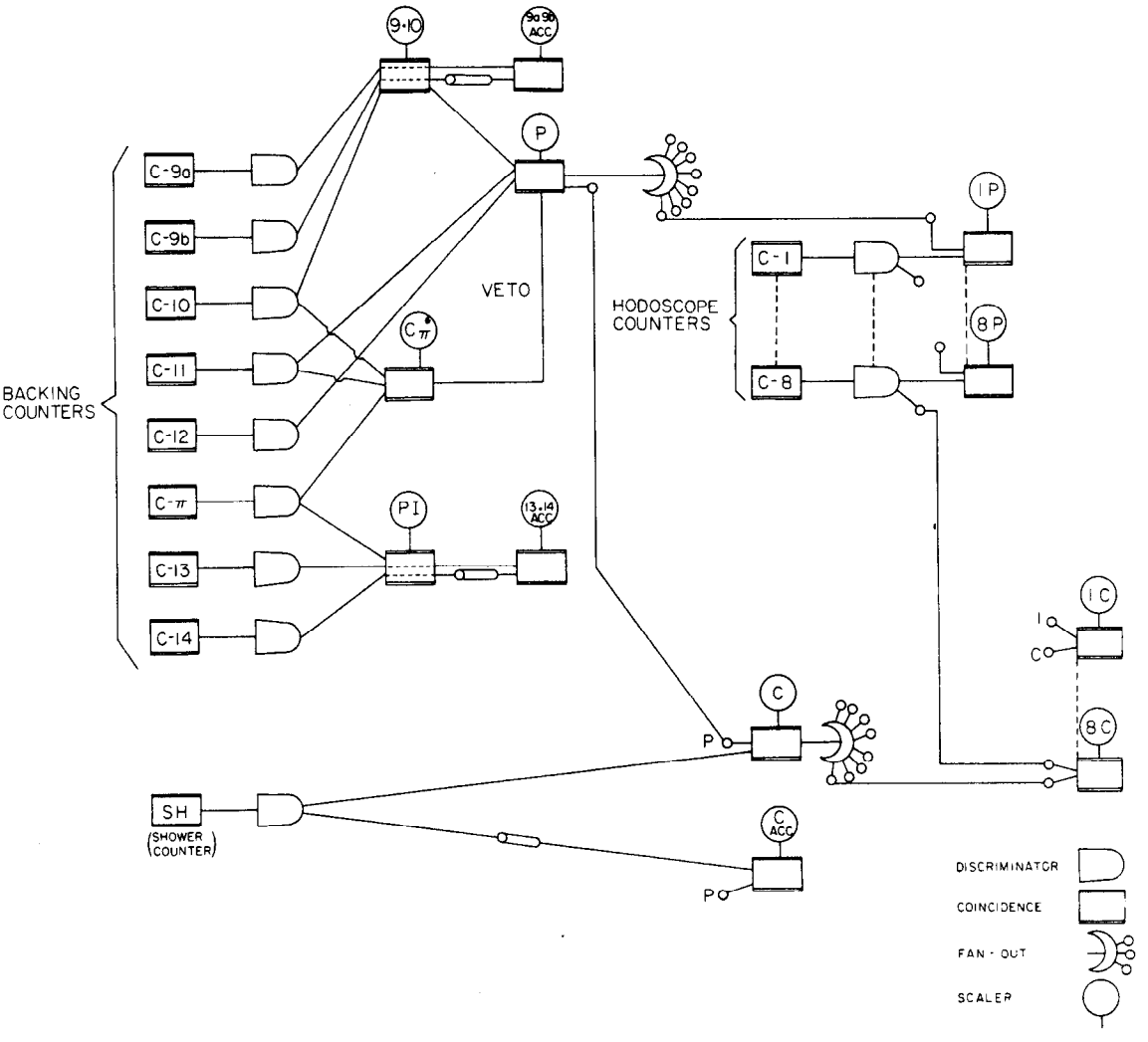

FIG. 9--Basic logic used with the gas target.

C. Counting House

The so-called "counting-house A" is situated outside end station A, directly over and well above the beam line on the upstream end. It is the terminus for signal cables and control wiring of all sorts. In addition to racks of electronics (as described in the last section) and integrators for the various beam monitors, it contains remote controls and read-out devices for the spectrometer current and field, spectrometer angle and aperture, rotation angle of the counter system, target cell position, and other experimental details. Closed-circuit television monitors provide views of zinc sulphide screens (for beam steering checks) and various devices and gauges in the accelerator and experimental area.

A dominant feature of the counting house is the SDS 9300 computer (Ref. 19), with 1.75 microsecond cycle time and 32 K-word memory, designed for scientific computation and real-time control. It has three tape drives, disc, card reader, card punch, teletype, line printer, oscilloscope, and plotter. For this experiment it was used as a very efficient secretary, to read and record (on the line printer and magnetic tape) all pertinent information about a data run: parameters of the beam, target, spectrometer and other devices, and values of all the scalers and beam monitors. It was programmed to recognize a number of improper experimental situations (screens left in the beam, etc.) and deliver an appropriate warning via the teletype or a tape-recorded audio message. By normalizing scaler counts to the primary beam monitor and displaying the results on the oscilloscope, line printer, or plotter, it enabled the experimenter to spot troubles with a run before much time was lost. In the event the computer failed, it was still possible to do all the above by hand.

III. METHOD

The general reaction to be studied, $\gamma+p \rightarrow X^o+p$, results in a neutral product X^o which decays rapidly (except in the elastic process, proton Compton scattering) and is thus difficult to detect. However it is possible to determine the effective "missing mass" corresponding to the neutral product from the kinematics of the reaction, if enough is known about the other particles: writing the process as $1 + 2 \rightarrow 3 + 4$ we have

$$M_3^2 = P_3^2 = (P_1 + P_2 - P_4)^2 \qquad \text{(III.1)}$$

from four-momentum conservation, where P_i is the four-momentum of particle i. In this case one gets

$$M_x^2 = 2k(p \cos \theta - T) - 2MT \qquad \text{(III.2)}$$

where k is the energy of the incident photon and p, θ, T, and M are the momentum, production angle, kinetic energy, and mass of the recoil proton. Since M is known, and $T = (p^2+M^2)^{1/2} - M$, it is sufficient to measure p and θ in a spectrometer, given the beam energy. Of course, intense monoenergetic photon beams are not easy to come by, but a bremsstrahlung beam of known endpoint energy is sufficient, as will be discussed.

Figure 10 shows a plot of Eq. (III.2) for a photon energy of 11.5 GeV and values of M_x corresponding to π^o, η, ρ^o, and ϕ mesons. As described in section II.B.1, the focal properties of the spectrometer used in this experiment are such that p and θ are orthogonal and focus in the same plane normal to the central flight path; thus, except for scale, the focal plane simply sees a small portion of Fig. 10 (up to 10% in p by 2^o in θ). In such a small region, and for momenta covered in this experiment ($\approx$ 300-1400 MeV/c), the lines of constant M_x are essentially straight and parallel, so that the hodoscope may simply be

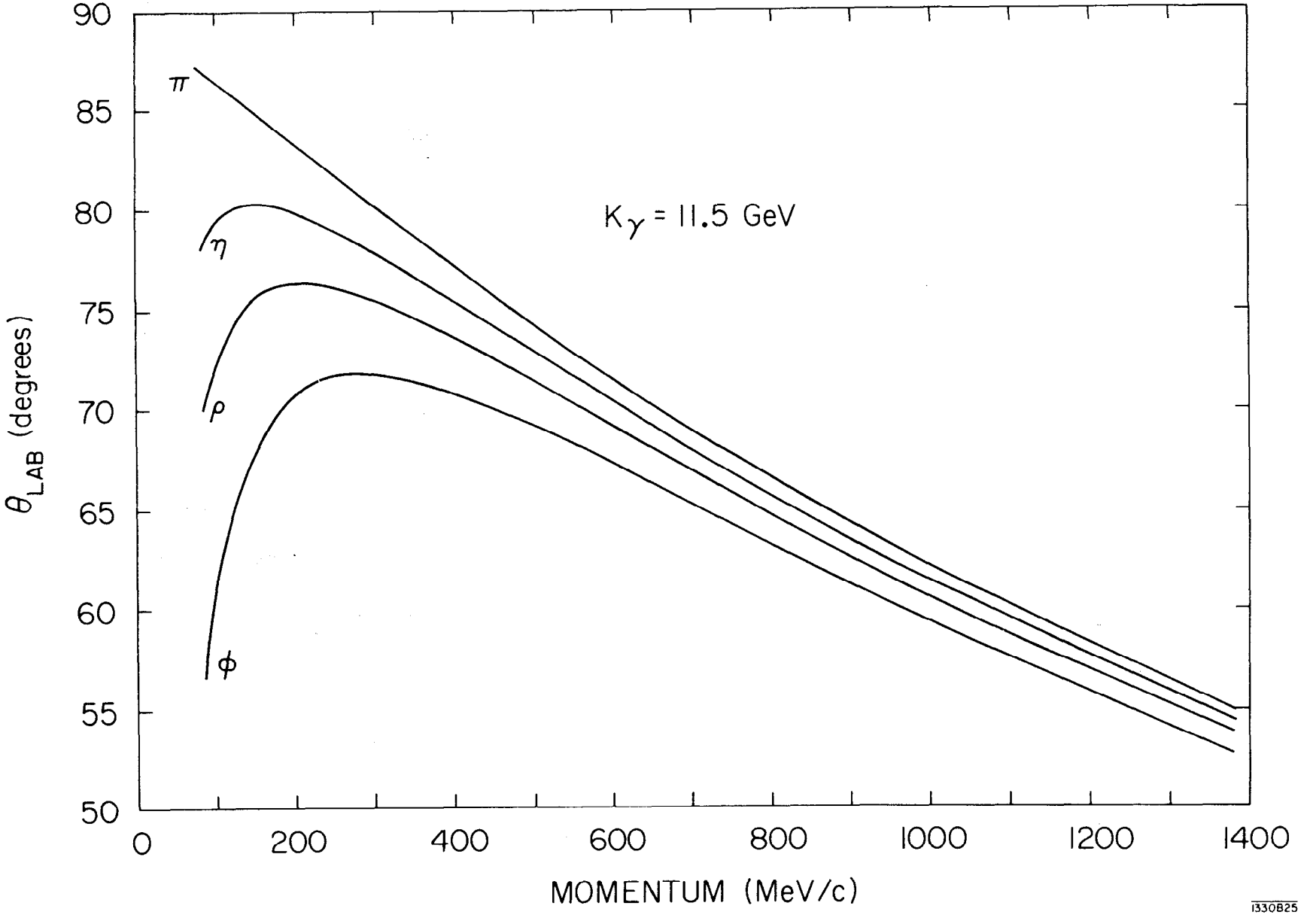

FIG. 10--11.5 GeV kinematics for $\gamma + p \rightarrow X^o + p$.

rotated to such an angle that the elements fall along such lines. The proper orientation is easily calculated for each case, given the p and θ dispersions of the magnet. Decoding of the kinematics is thus accomplished automatically, without complex crossed hodoscopes and event-by-event computer analysis. That is, for fixed spectrometer field and beam energy, the proton yield across the hodoscope would simply be a function of missing mass, showing bumps corresponding to existing particles.

A (p, θ) plot of Eq. (III.2) could also be made for a single value of M_X and several values of the photon energy. It would look essentially like Fig. 10, with photon energy increasing with θ for fixed p. Viewed this way, the properly rotated hodoscope elements each correspond to different k for a given missing mass. Now consider a bremsstrahlung beam, containing photon energies from zero up to a maximum E_0 (the "endpoint" energy) with a spectrum approximating a step function:

$$k\, n(k) \begin{cases} \approx 1 \text{ for } k < E_0 \\ = 0 \text{ for } k > E_0 \end{cases} .$$

The yield of protons in the hodoscope from photoproduction of a given particle with such a beam will be a similar function: zero for angles greater than that corresponding to E_0, a more or less sharp rise at threshold proportional to the particular cross section, and a more or less slowly varying yield for further decreasing θ, depending on the behavior of the cross section with energy. Calculation of this yield is described in the Appendix.

The basic data-taking pattern in this experiment consisted of fixing the spectrometer momentum (thus the value of $t = -2MT$) and the primary electron beam energy (thus the endpoint photon energy), rotating the hodoscope to the

appropriate orientation, and measuring the proton rate as a function of production angle. Such a "sweep" was made up of a number of runs taken at different values of the spectrometer angle, separated by multiples of a "bin" or width of one hodoscope element in θ. Ideally, the accumulated result was then a composite of the views just described: the yield was a sum of "steps" occurring at different threshold angles, with higher masses entering at smaller angles. The various cross sections could then be determined from the corresponding "step heights", as described in the Appendix. However, there were certain complications due to backgrounds and lack of resolution as discussed below. A sample yield curve is shown and described later in this section.

From the kinematics, it is clear that for a given primary energy and t-value there is a limiting angle, corresponding to $M_x = 0$ and $k = E_0$, such that a single γp event cannot produce a recoil proton at a greater angle. Beyond this kinematic limit there should be no counts, yet "ghost protons" were always observed in this region. A few of these, of course, were pion counts which escaped the electronic biases, but time-of-flight studies showed that most were protons. Although using a target mask (see section II.A.4) reduced the ghost rate by a factor of two, full-dummy target comparisons showed that the majority came from the hydrogen. The conclusion is that they came from various double processes in the target. In any case, this background was always smooth and slowly-varying, so that it could not affect the apparent size of a step directly. Instead, it required that extra time be spent to measure its magnitude and behavior, and it degraded the statistics on the rest of the yield.

A similar problem was caused by nonresonant events in the kinematically allowed region: processes such as photoproduction of $\pi^+\pi^-$, 3π, $\pi\rho$ and so forth. Since the products do not have unique missing masses they do not result in step yields, but rather a smooth rise from threshold.

The major resolution problem in this experiment was the loss of angle resolution due to multiple scattering of the recoil protons, in the target hydrogen and other material, before reaching the spectrometer. The resulting smearing of steps was a serious problem at low momentum-transfers, particularly in the case of the η, as its yield occurs on a steep background due to nonresonant processes and the low-mass tail of the ρ^o. The π^o step at high energies also suffered: here the mass scale is compressed and the multipion and ρ production yields crowd in close. Finally, the combined effects of hodoscope counter width and multiple scattering did not leave enough resolution, at any energy and t-value, to separate the step yields due to π^o photoproduction and proton Compton scattering. Thus a measurement of the Compton effect was necessary before the π^o results could be made final.

As already mentioned, the Compton measurement was done with a shower counter in coincidence with the 1.6 GeV/c spectrometer. For this case Eq. (III.2) can be rewritten

$$|t| = 2kk_\gamma(1 - \cos\theta_\gamma) \qquad \text{(III.2')}$$

where k_γ and θ_γ are the energy and laboratory angle of the scattered photon. Since $k_\gamma = k - T = k - |t|/2M_p$, with the t-value fixed by the spectrometer momentum setting, the range of θ_γ accepted by the shower counter defines a range of incident photon energies k. The coincidence yield across the hodoscope is then not a step but a peak, such as the photoproduction processes would also produce from a "monochromatic" beam.

Separation of Compton events from π^o events was due to geometry: the Compton scattered photons corresponding to protons in the spectrometer are required by kinematics (coplanarity) to be produced into a band defined by the vertical spectrometer aperture with a cutoff at small angles from the endpoint

energy of the beam. The photoproduced π^o's are produced toward essentially the same region but quickly decay into photon pairs 99% of the time. One of the two photons from a π^o decay will always be within a cone (relative to the π^o direction) of radius m_π/p_π, where m_π and p_π are the mass and momentum of the π^o, so that it is possible for a π^o event to produce a coincidence; but since for these energies and t-values the solid angle of the decay cone turns out to be large compared to that of a shower counter matched to the spectrometer aperture and a reasonable energy bite (say, $\Delta k/k = 10\%$), the π^o events in practice are rejected by more than an order of magnitude. Furthermore, the remaining π^o contamination may be measured by moving the shower counter up or down out of the region illuminated by Compton events. The efficiency of detecting π^o decay photons decreases (typically by 15%), but the difference can be calculated and a correction applied.

Since elastic electron scattering has essentially the same kinematics as Compton scattering, with ample rate and small backgrounds, it was a useful tool for checking alignment of the shower counter, testing its response and efficiency, checking linearity of the variable apertures, setting the timing between shower counter and spectrometer, and so forth. The Compton data were taken using the same pattern as for photoproduction, but required a smaller range of angles covered. The beam intensity was adjusted to reduce accidental coincidences to a tolerable level, and measurements were then taken with the shower counter in and out of the Compton region. The π^o efficiency ratio between the two cases was calculated by a computer program. Note that with the logic as described in section II.B.3 it was possible (actually automatic) to observe the Compton (plus π^o) coincidence yield at the same time as the π^o (plus Compton) step in the spectrometer alone. Serious simultaneous measurements were actually made in several cases.

Examples of experimental yields, as described in this section, are shown in the next two illustrations (more sample data are included in the next section). Figure 11 shows photoproduction data for a primary beam energy of 11.5 GeV, and $t = -0.7$ $(GeV/c)^2$; the abscissa is missing-mass-squared, which for the values of p and θ in this experiment is very nearly linear with θ (see Eq. (III.2)). View (A) is just the normalized accumulated spectrometer counts arranged in hodoscope bins. The solid lines represent an illustrative least-squares fit assuming smooth backgrounds as described earlier; π^o, ρ^o, and ϕ yields including multiple scattering, with the π^o and ϕ contributions arbitrarily taken to be constant past threshold; and negligible contributions from Compton scattering and η photoproduction. The π^o yield is of course partly Compton. In (B) these points have been subtracted, bin by bin, from a similar sweep at 13.0 GeV endpoint energy. Since the reduced bremsstrahlung spectrum changes only slowly with energy, the difference is essentially due to the band of photon energies between 11.5 and 13.0 GeV, approximating a "monochromatic" beam. In (C) a similar display has been produced by "differentiating" the yield curve in (A), specifically by subtracting the counts in bin i-1 from those in bin i+1 and plotting the difference in bin i. Note that the η is actually visible, but only as a "shoulder" on the ρ^o peak, as the mass resolution at this high energy is not sufficient to make a clean separation.

Figure 12 shows a sample coincidence measurement at $t = -0.5$ $(GeV/c)^2$ with a primary beam energy of 12 GeV (the average photon energy was approximately 11.5 GeV, since the shower counter accepted a range of energies below the maximum). The yield in arbitrary units is plotted in the usual hodoscope bins (thus laboratory angle increases linearly to the left), and a missing mass scale is provided on the abscissa. (A) shows results for otherwise identical

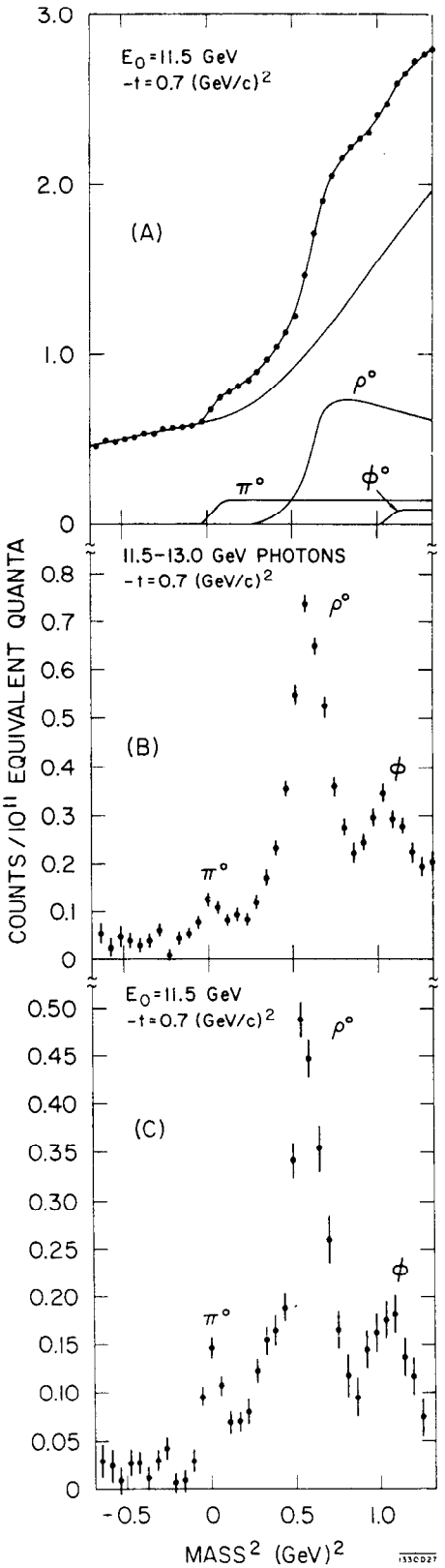

FIG. 11--Sample recoil proton yield curve.

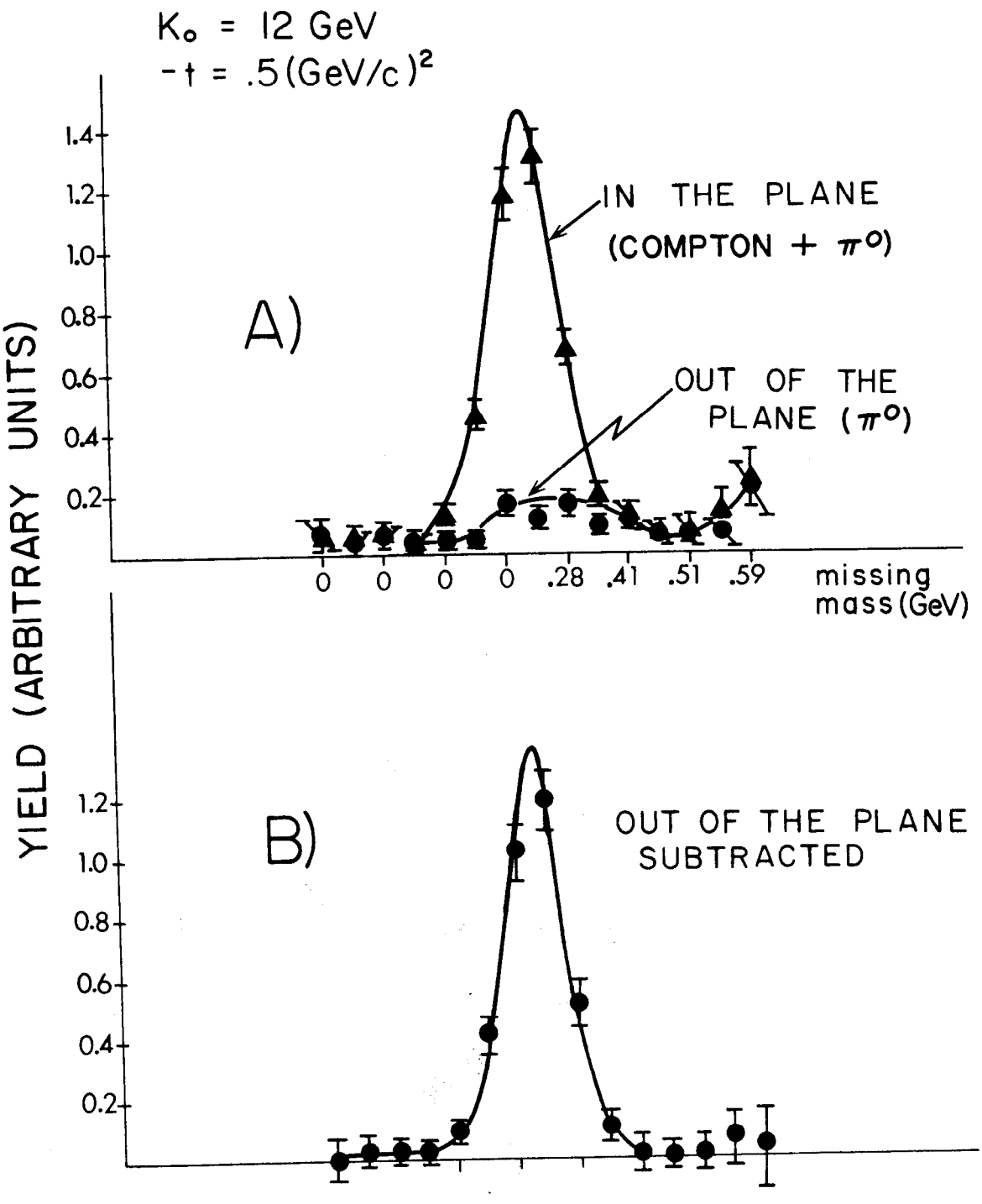

FIG. 12--Sample coincidence yield.

angle sweeps, one with the shower counter positioned to accept Compton events, the other with it moved vertically to sample the π^0 contamination. In (B) the two have been subtracted: the accidental counts cancel nicely, and the result contains only a small residue of π^0 events.

In addition to the basic data taken as described above, certain studies were made during the experiment to determine what corrections to these data were required, and how much. Rate effects, such as dead-time losses in the electronics, were measured in cases of high counting rate (several events per 1.6 microsecond beam pulse). The net effect was seen directly by taking otherwise identical runs with beam intensities differing by a factor of 3 or so, typically by varying the collimator C-10 and leaving the accelerator spectrum and steering untouched. The beam rates actually used were adjusted to keep the net loss under 5%. Absorption losses of protons in the counter system were determined by installing plastic plates in one of the variable absorber changers, and observing the difference in normalized rate in the telescope with more or less plastic moved in place. The loss in a given amount of plastic was thus measured as a function of proton momentum. When the C_π veto was used, there was an additional possible loss of proton events due to a small efficiency of the Cerenkov counter for protons. This was measured by defining a clean proton trigger without the veto (such as with a time-of-flight system, or using the shower coincidence with electron scattering), then switching the veto in and out, observing the change in normalized trigger rate.

IV. DATA ANALYSIS

A. Data Reduction

The raw π^0 and η photoproduction data to be analyzed were recorded in the form of approximately 110 separate "sweeps", some containing usable yields from both processes. These sweeps were taken as described in the last section for various combinations of beam endpoint energy and spectrometer momentum, and each consisted of a number of separate runs (perhaps 20 or 30) at different spectrometer angles. After each run, lasting of the order of 10 minutes, the computer recorded on magnetic tape all the numbers pertaining to that run: machine energy and spectrometer momentum (same for all runs in a sweep), spectrometer angle and apertures, charges on the various beam monitors, counts on approximately 40 hardware scalers, and so forth. This mass of information had to be filtered down in various stages to produce results in the form of cross sections.

The first step, following a two- or three-week accelerator cycle, was to retrieve the important numbers from the magnetic tape and get them punched on cards in a convenient format. This typically required two 80-column cards per run. This was followed by a period of editing, using as a guide the log books kept during the experiment. Each run was studied as to its purpose and "quality": good data runs were separated from various check runs (rate checks, dummy target runs, monitor calibrations, etc.) and from any runs recorded in spite of improper experimental conditions (spectrometer angle or momentum wrong, wrong hodoscope orientation, bad beam steering, incorrect logic, etc.). Some of the bad runs were saved if the effect of the particular error happened to be negligible or could be corrected.

The various rate effect comparisons were collected together and analyzed to provide a means of estimating net dead-time losses in each data run. In each case the fractional change in normalized counting rate between high and low rate runs (summed over the hodoscope) was compared with the concurrent change in the various accidental coincidence rates, usually divided by appropriate real rates. A formula could then be derived to fit all cases, which gave the dead-time loss in terms of one or more important accidental ratios. In general, it turned out that within a sweep the beam intensity was sufficiently constant that the dead-time correction did not need to be applied run by run; rather, a step height from the sweep could later be increased by the average value of the formula for the runs taken in that particular region of angles.

A careful analysis was also made of the various monitor calibration runs using the silver calorimeter as an absolute standard as explained in section II.A.3. In each case the proper calorimeter constant was used, having been checked before each accelerator running cycle by applying a known amount of heat from a built-in electric heater and observing the temperature change. The resulting SEQ calibrations were averaged at each beam energy for each running period, and the averages were used to calculate the number of equivalent quanta incident in each run.

The next step was a preliminary "first-pass" accumulation of the various overlapping runs in each sweep into a single set of yield values versus laboratory angle in hodoscope bins. That is, where a given bin was covered in more than one run (a different hodoscope element in each case), the total counts in that bin were divided by the total incident equivalent quanta, as summed over those runs. The result is a simple average if the runs in question all had the same amount of incident beam, as was often true. A considerable degree of

overlap had been found to be desirable, as this tended to average out efficiency differences among the hodoscope counters and any monitor instabilities. More often than not, in fact, part of a sweep was taken with complete overlap; that is, each bin was eventually covered by each of the eight hodoscope counters, with adjacent runs separated in spectrometer angle by a single bin width. This produced a high degree of redundancy in the data and provided a source of diagnostic information about the sweep.

For example, it was easy to determine relative hodoscope efficiencies from a region of 8-counter overlap: in a given bin, the ratio of the rate in one counter to the accumulation (average) of all eight is just the relative "efficiency" of that counter. Averaged over a number of bins, such ratios achieved reasonable statistical precision, and could be used to correct individual hodoscope counts in a second pass, thus removing some nonstatistical fluctuations in the part of the yield curve where there was not complete overlap. Normally these ratios were within one percent of 1.00, so that the correction was not really important; but all sweeps taken with the gas target for $|t| \leq 0.2$ were quite abnormal. In these cases the low target density caused the real rate to be lower than usual compared to the room background, and the proton telescope was unusually short (using only 9a:9b:10, see section II.B.3), enabling it to count a comparatively large fraction of the room background that got through the shielding walls. This junk rate did not, of course, count uniformly across the hodoscope, because the possible angles were more restricted for the edge counters. Thus in a region where the real rate (coming up the spectrometer) was fairly flat, there appeared in each run an evident "hump" across the hodoscope, with the center counters about 10% higher than the edge counters. The 8-counter overlap technique averaged this out and permitted the necessary correction to be

determined. It was found, in agreement with the above explanation, that for each counter relative to the average, the ratio was not constant with angle but rather the absolute difference, so that as the real rate changed the junk rate did not. Thus no counter inefficiencies were responsible, and the correction was not to divide each counter by its average ratio but to add to it the average difference. The smoothing effect on the sweeps was quite considerable.

Further information was derived from the accumulations by comparing the yield in a given run, summed over the hodoscope, to the accumulation summed over those eight bins covered. To the extent that for the sweep as a whole this ratio varied from 1.00 more than expected from statistics, possible monitor instabilities were indicated. A plot of this ratio versus run number (related to time) in a sweep occasionally showed apparent slow drifts or sudden changes, but only of the order of 1% or less, in agreement with the long-term SEQ stability as determined by the calorimeter comparisons. A check on these plots was provided by the pion rate over each sweep, monitored as described in section II.B. These smooth pion yield curves were fitted to polynomials, and individual runs were compared to the curve. Where the results showed the same pattern versus run number, an appropriate smooth correction was applied run by run.

With all these corrections applied, a final quality check could be made on each sweep by calculating the root-mean-square deviations of the different hodoscope contributions in each bin from the accumulation in that bin, and comparing the result to the statistical errors. This "chi-square" for the sweep normally gave a reduced value close to 1 when proper corrections had been made.

The final step in data reduction was then to produce a set of properly corrected accumulated sweeps, containing correct monitor calibrations. For each bin covered in each sweep, the yield was calculated in counts per 10^{11} or 10^{12} equivalent quanta, and the result was punched on a card containing bin number, yield, statistical error, beam energy, nominal t-value, and the value of the laboratory angle in the center of that bin. The results were also printed by the computer used to carry out all these calculations, and the printout included a missing-mass calculated for each bin using the beam endpoint energy, the angle of that bin, and the correct production momentum. The data were then ready for the extraction of cross sections.

B. Fitting

As previously stated, the basic step in determining a cross section was in essence very simple: to measure the rise in yield due to the onset of production of the particle in question. In certain cases, where statistics and resolution were good and backgrounds smooth and slowly varying, this was in fact almost as easy as subtracting two numbers, namely the yield above and below the "step". In most cases the angular resolution was not so good, or backgrounds were changing rapidly, or both. It was then necessary to fit the yield curves in some way. This experiment took place in stages over a period of more than two years, with each portion of accelerator running time followed by a period of analysis, so that a considerable familiarity was built up with various situations before the final analysis was done. Three fitting techniques were found useful, and will be discussed.

The first technique might be called the "eyeball" method, and consisted of taking a plot of yield versus lab angle and using a French curve to fit the regions above and below the threshold of interest. These regions were extrapolated

over and under the step, respectively, and the vertical separation was then the step height. In any given situation where the statistics were good, this was a fast and reasonably reliable way of getting results. However, it was difficult to be entirely consistent between fits, and some available information was not easily incorporated, such as the experimental angle resolution. A second method with similar problems involved "folding" the yield curve about the threshold in question: that is, if the threshold fell in bin i, the yield in bin i-1 was subtracted from that in i+1, that in i-2 from that in i+2, and so on. The resulting values, plotted against symmetric angular distance from threshold, would fall on a smooth curve approaching the step height if the resolution were perfect. A French curve could then be used to extrapolate this single curve to threshold, or a least-squares fit to a polynomial could be made. In the latter case, however, there was no way to ensure that the fit would be a monotonically rising curve, so the results were often physically unreal.

The method used for the final analysis was made possible by the availability of a convenient time-sharing computer system with remote-terminal access. With this system it was possible to request a linear least-squares fit of a particular yield curve to appropriate functions, and get an immediate answer. If, upon study, the fit was not found to be satisfactory, the input parameters specifying the functions could be varied and other fits tried. In the end, all final fits were required to represent a consistent set of parameters. Thus the computer provided a flexible yet reproducible and basically objective "French curve".

Sample π^0 yield curves and fits are shown in Fig. 13. The fits are shown as the dashed lines, including the contributions from ghost proton background, π^0 yield, and a smoothly rising yield from nonresonant processes (starting at

the 2π mass) plus, in some cases, the low mass tail of the ρ^o. Multiple scattering has been included. Where statistical error bars do not appear on the points, they are smaller than the dots shown. The sample cases were chosen so that Fig. 13a through f provide a coarse pass over the range of t-values in the experiment, at an intermediate energy of approximately 12 GeV, while g and h show low and high energy extremes near the low $|t|$-value end, and i and j similarly at a high value of $|t|$. It may be seen that the points at low energy are quite clean, but as the energy increases the π^o cross section decreases more rapidly than others, and the mass resolution gets poorer. For a given target the angle resolution gets poorer with decreasing $|t|$ as the multiple scattering increases (note that the angle width of a bin does not change much with t). The points for $|t| \leq 0.4$ were taken with a gas target, yet at $t=-0.1$ the resolution is marginal.

The region over which each fit was made was chosen so that the π^o, as nearly as possible, was the dominant feature. All available ghost background points were included, but above the π^o the fit was cut off where additional points ceased to add any significance. In no case was the fit carried out past the mass of the ρ^o, so that an extra complicated function was not needed to fit its yield. Such a fit would also have resulted in less significance for the fit to the π^o yield (usually much smaller).

The fitting functions were then specified as follows. A quadratic polynomial in angle was provided for the ghost proton background. A π^o step yield of unit height was calculated by the computer given the threshold angle and the assumed energy dependence of the cross section, and including the angle resolution of the hodoscope counters. A given amount of Gaussian multiple scattering was then folded in. For the nonresonant background and low-mass ρ^o tail there was

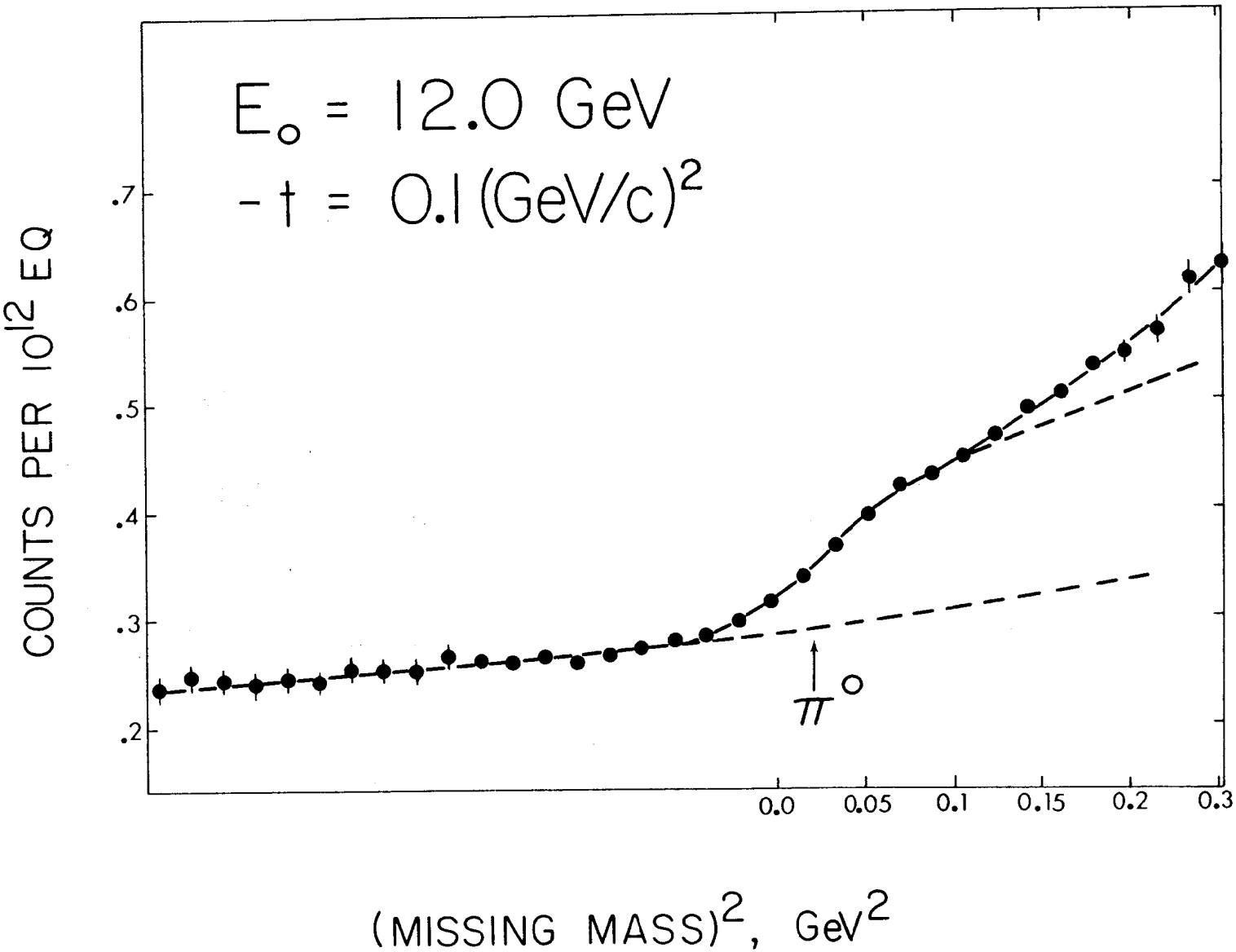

FIG. 13a--Sample π^o fits.

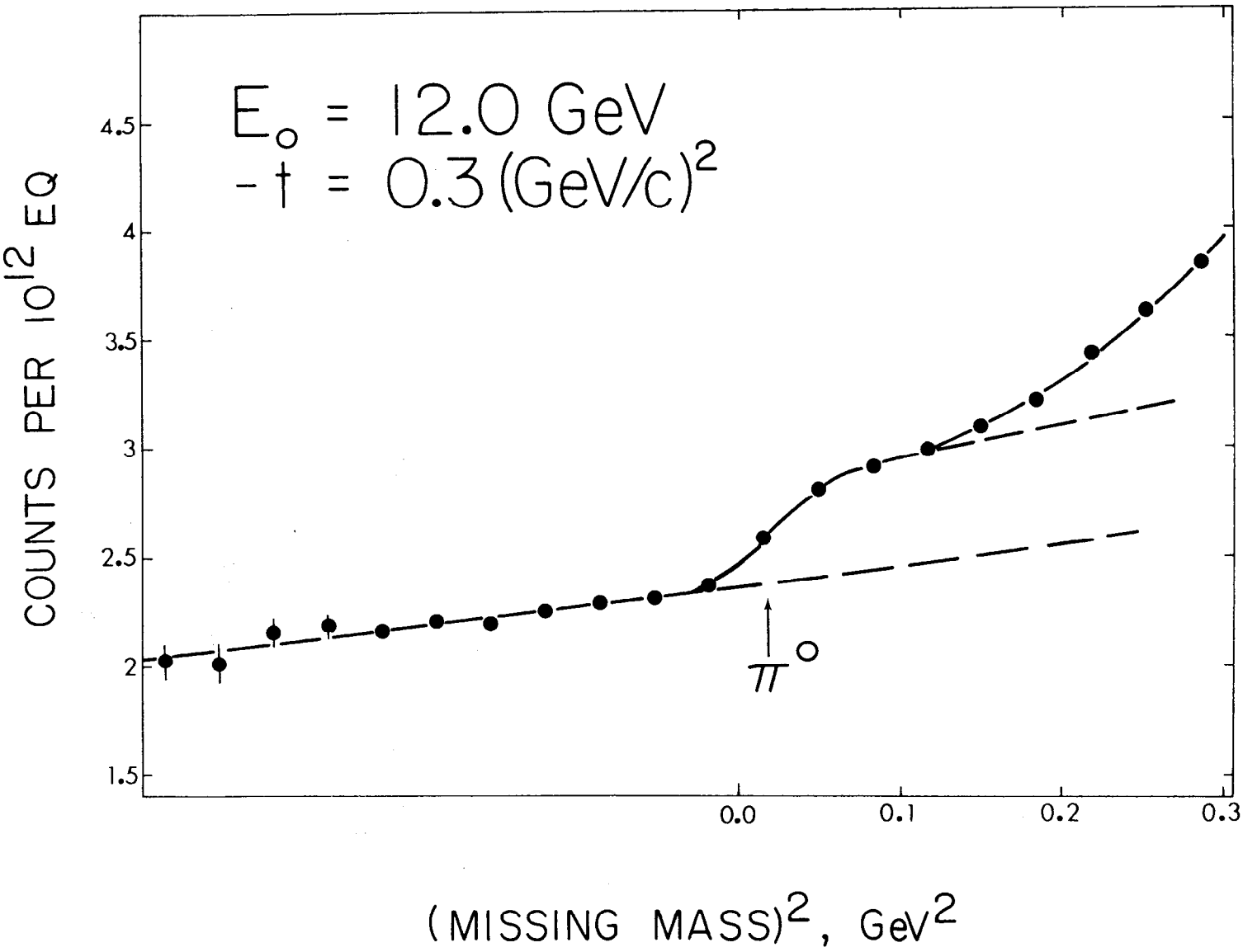

FIG. 13b--Sample π^o fits.

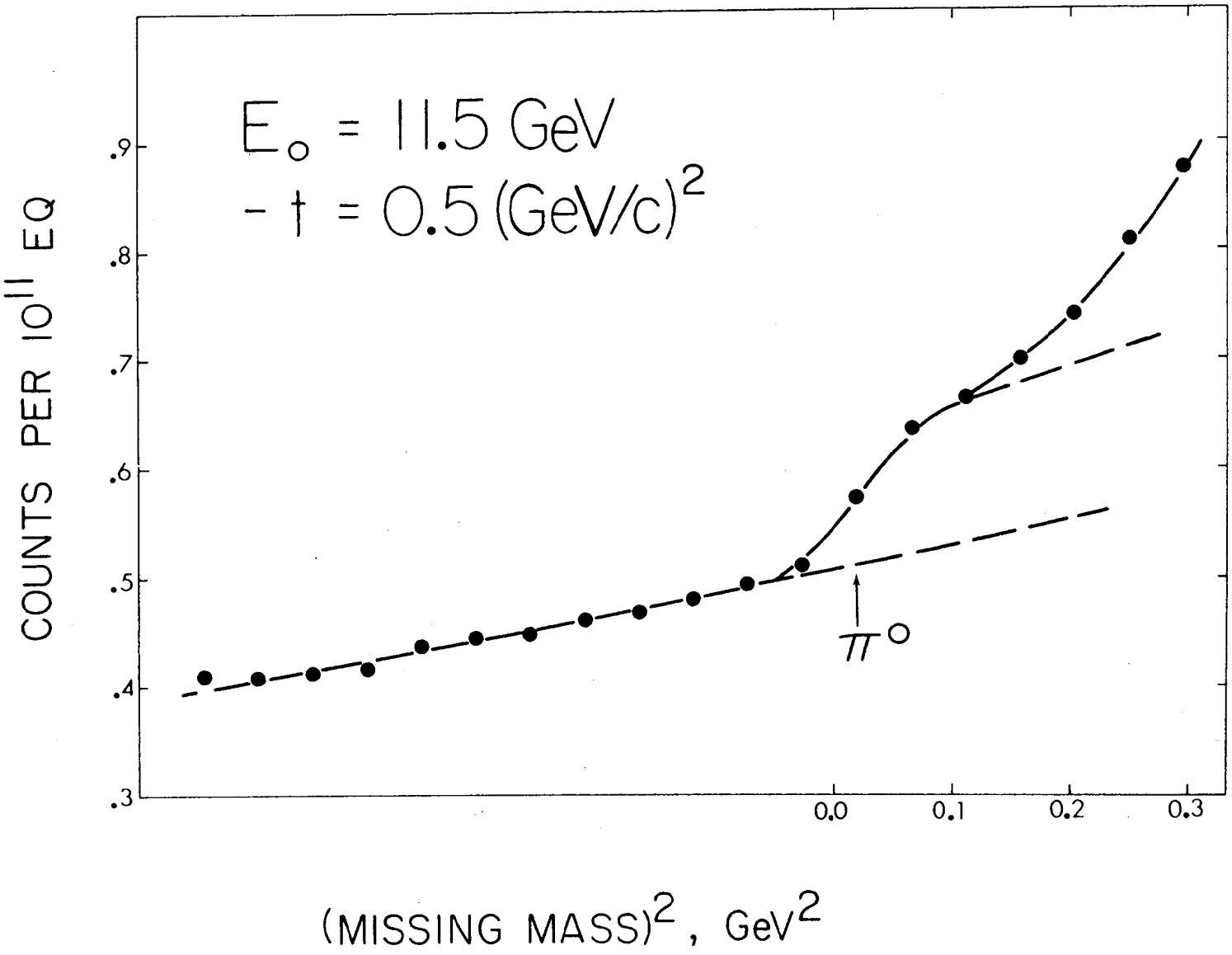

FIG. 13c--Sample π^o fits.

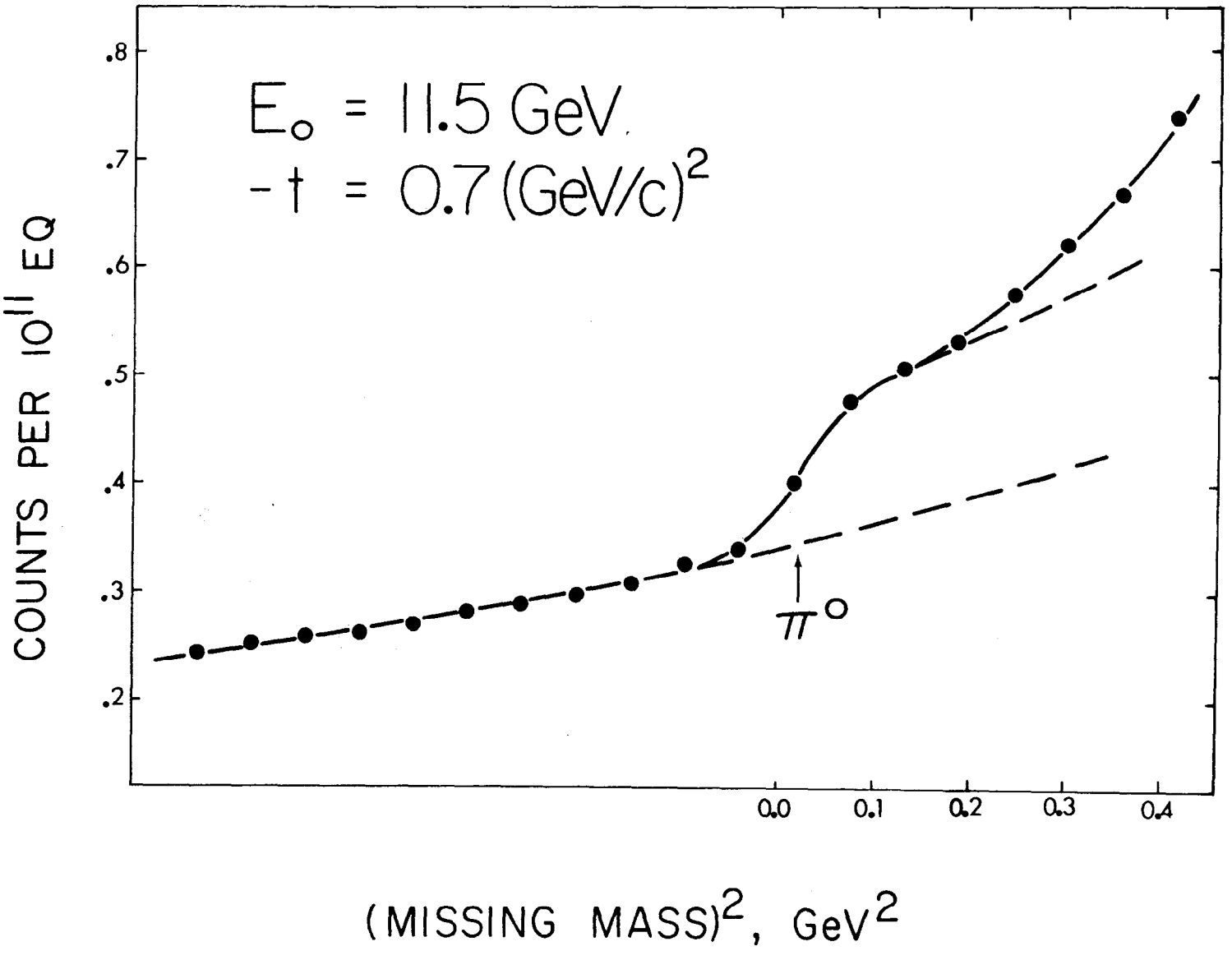

FIG. 13d--Sample π^o fits.

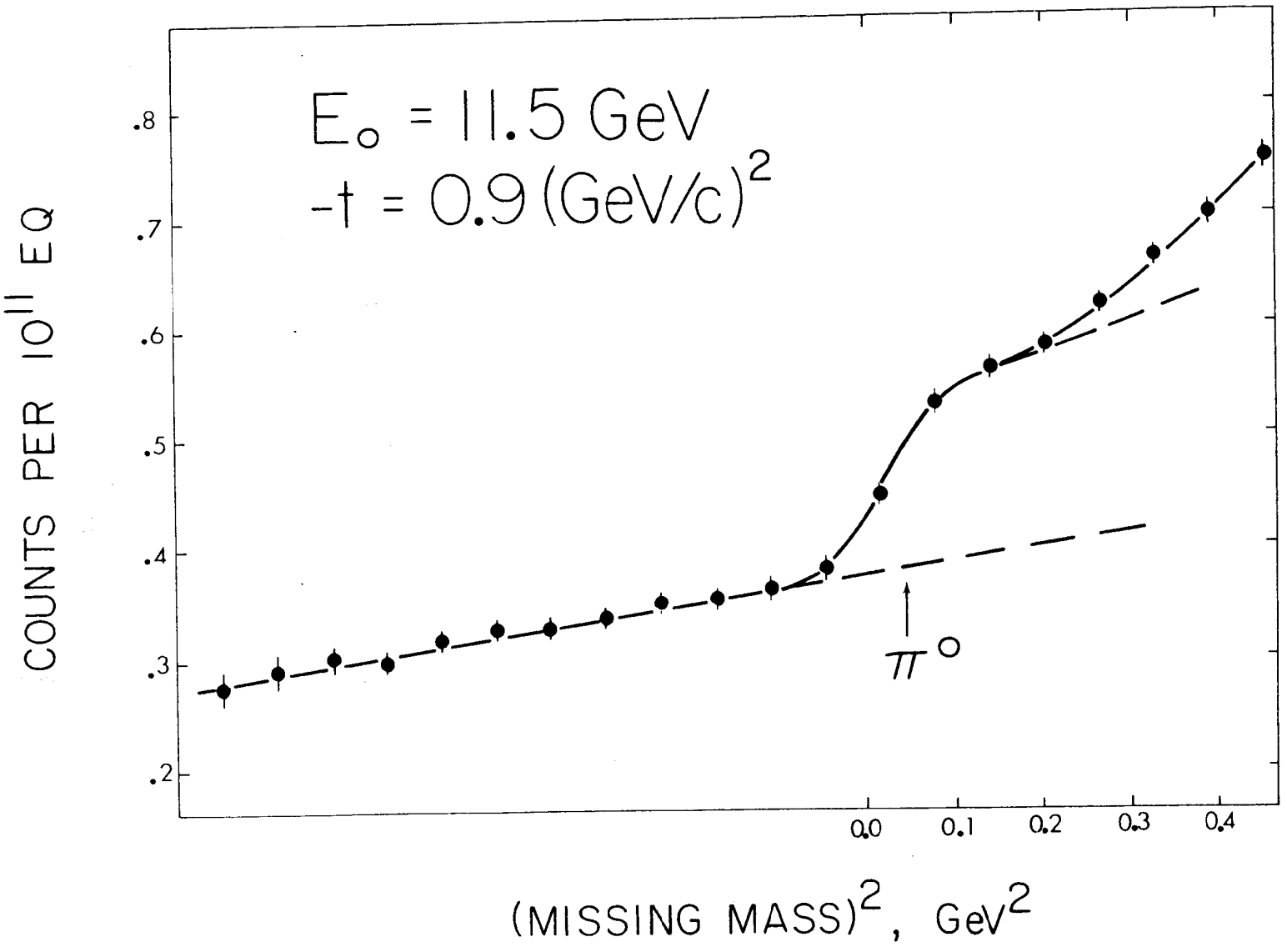

FIG. 13e--Sample π^o fits.

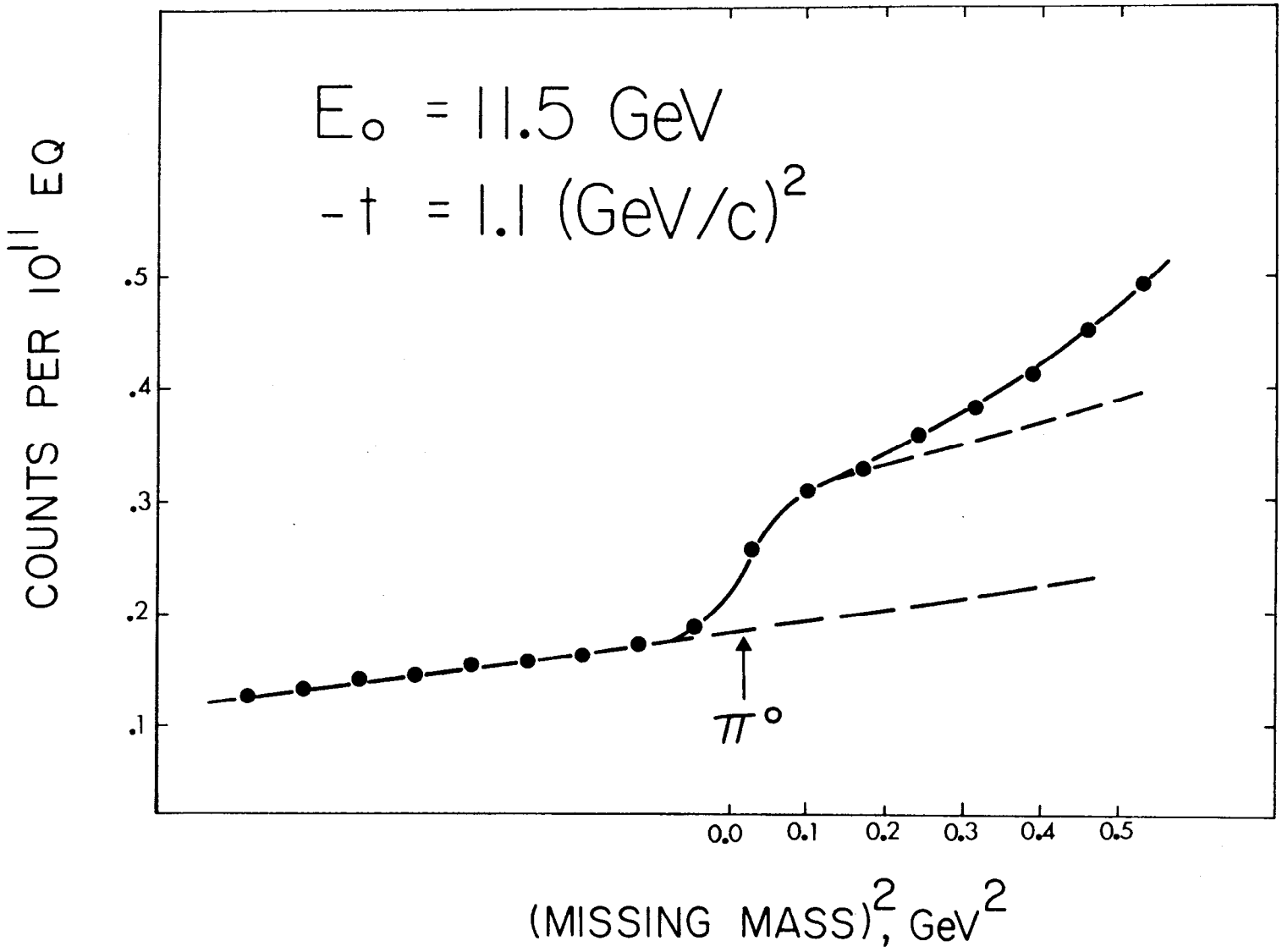

FIG. 13f--Sample π^o fits.

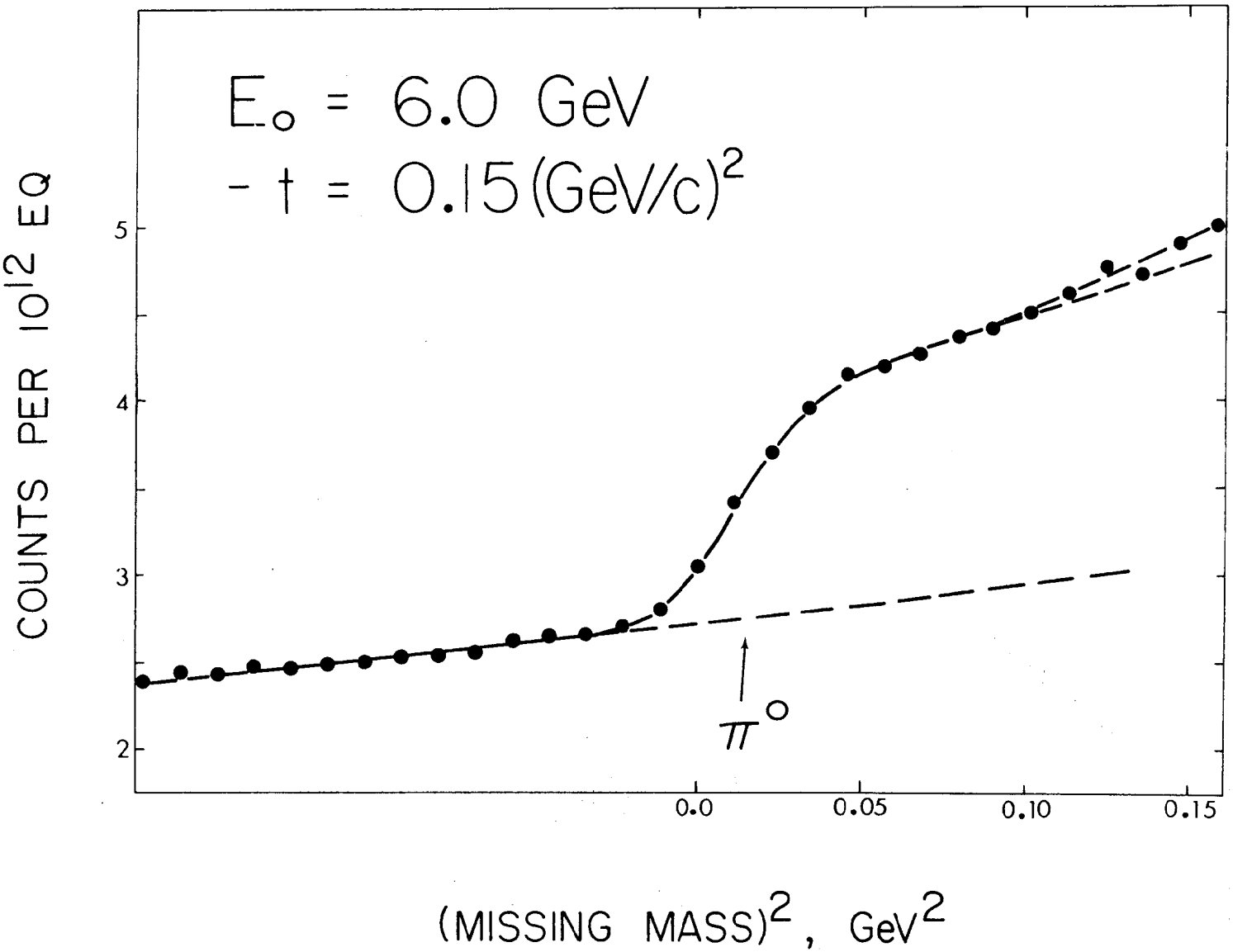

FIG. 13g--Sample π^o fits.

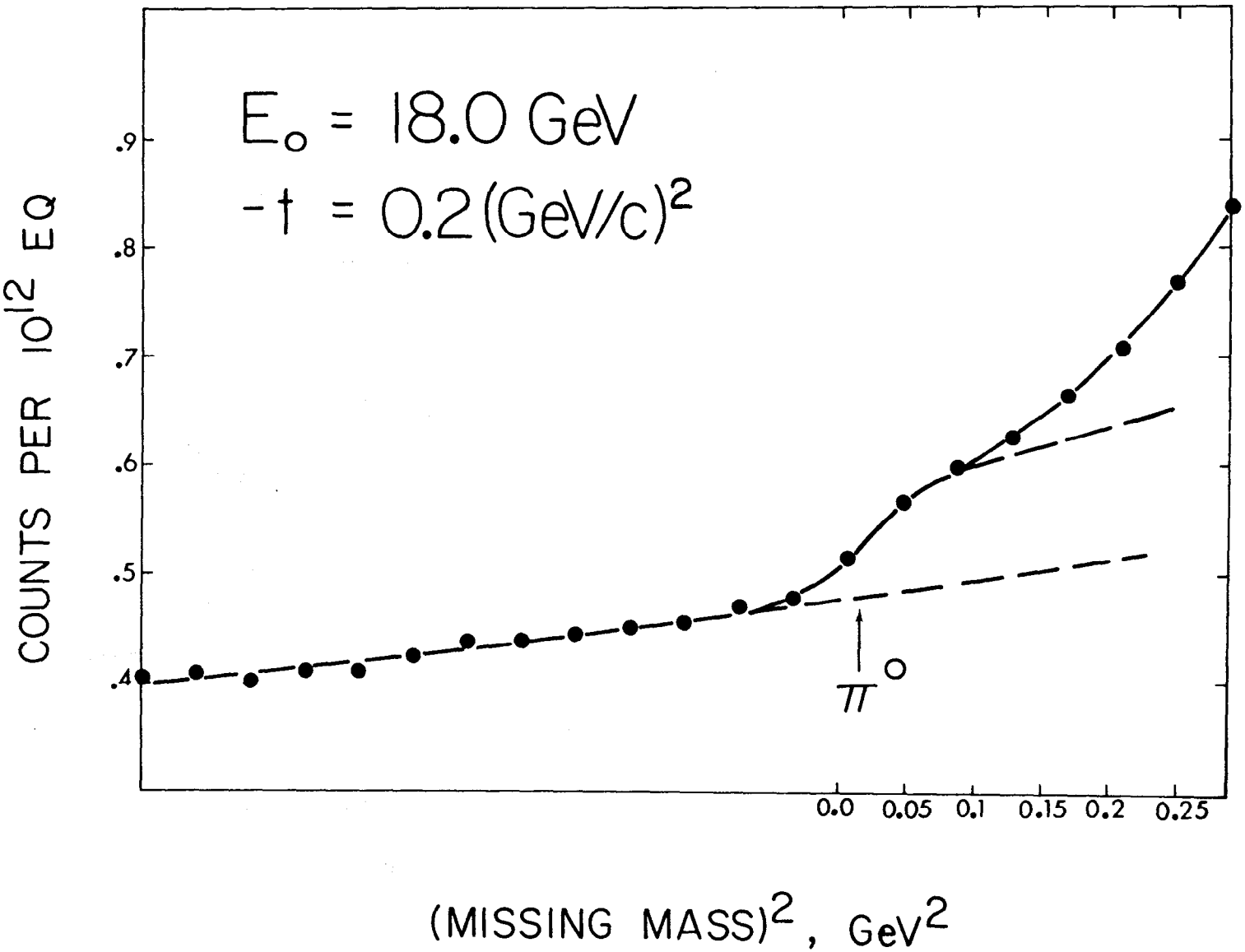

FIG. 13h--Sample π^o fits.

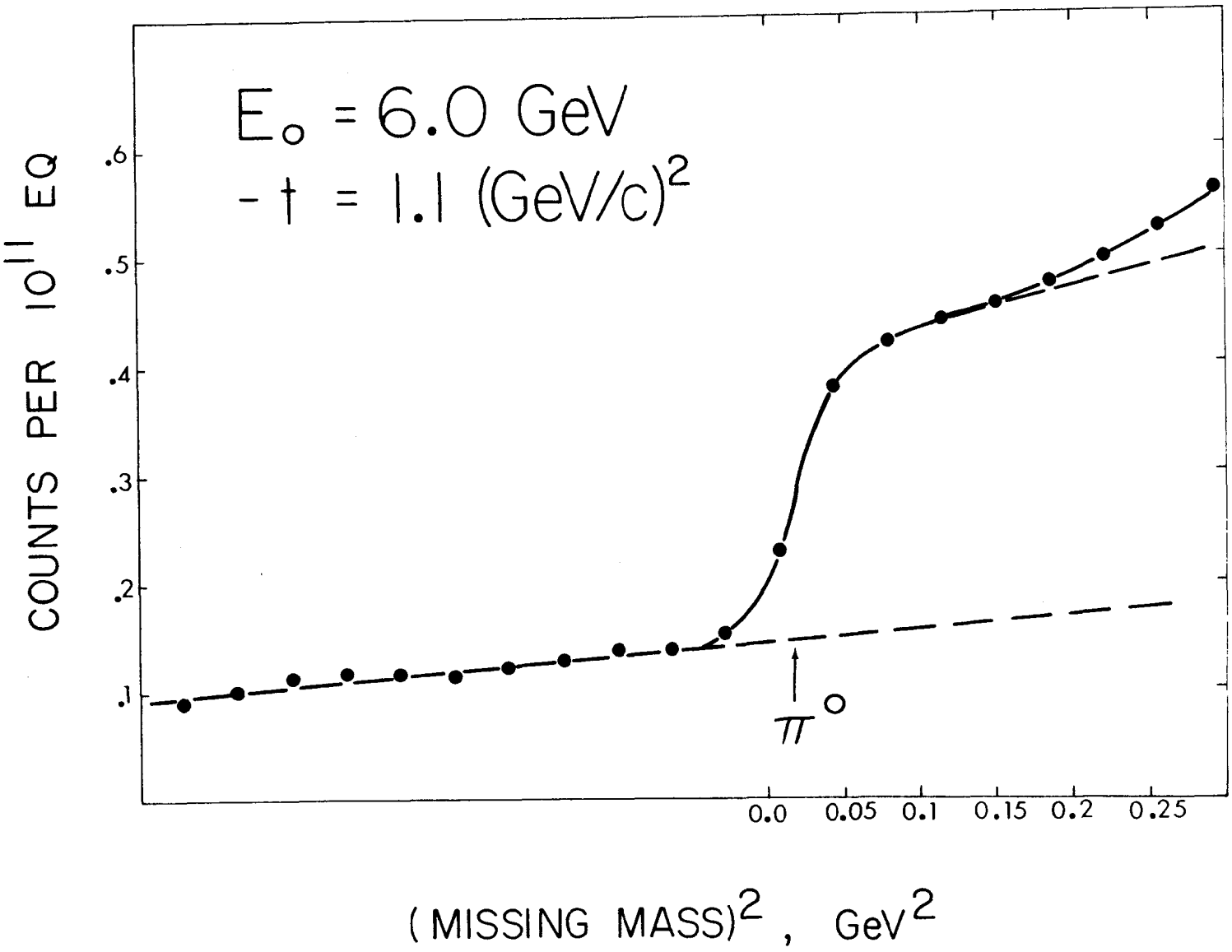

FIG. 13i--Sample π^o fits.

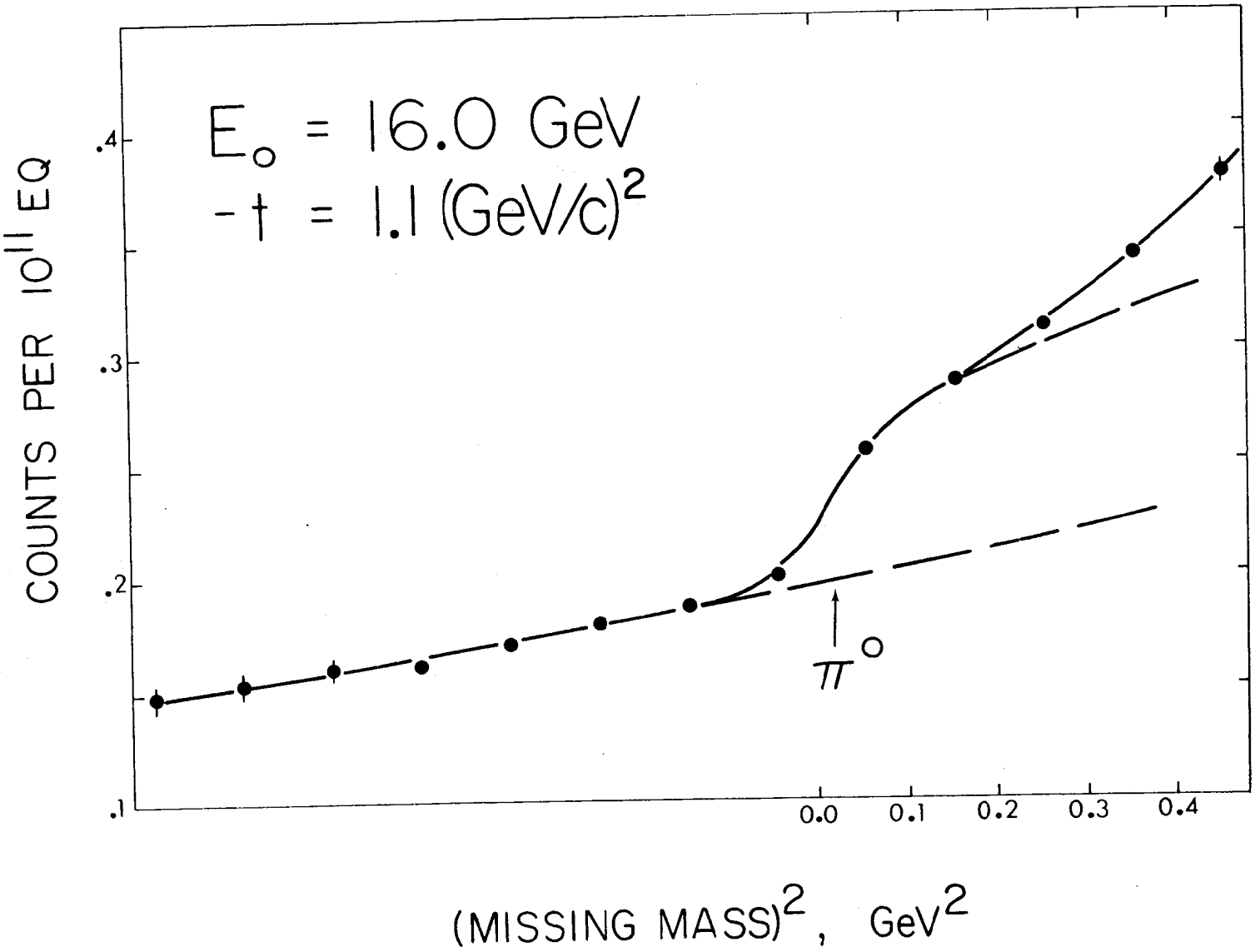

FIG. 13j--Sample π^o fits.

provided a quadratic polynomial with no constant term, starting at the given 2π threshold and with multiple scattering folded in. The least-squares coefficients of the various functions were then calculated by matrix inversion. These functions were more than adequate as long as the fit was cut off below the ρ^o mass, or below the η in the cases where it was significant. In fact, the linear term in the 2π polynomial was never needed, and more often than not the ghost proton background was for all practical purposes a straight line over the region covered and could be fitted as such.

The Compton cross sections had been calculated separately, from the coincidence measurements, as described previously in section III. Where the results were small enough compared to the π^o, the π^o + Compton step yields were fitted as though they were all π^o, and the derived cross sections were later reduced by the appropriate amount. For $|t| \leq 0.6$, however, the Compton effect was a major contribution at the higher energies. In each of these cases a Compton step yield was calculated, as described above for the π^o but of a magnitude derived from the measured cross section, and this was subtracted from the full yield curve before final fitting as described above. Only in this way was it easy to put in the energy dependences properly: since the Compton cross section is approximately constant with energy while the π^o falls sharply, a mixture of the two yields is a complicated function.

Figure 14 shows sample η yield curves and fits, chosen to represent every value of t at which measurements are reported, at energies around 6 GeV. As may be seen, η photoproduction was more difficult to measure than π^o production, since the η yield is usually much smaller and falls on a steeper background. Fortunately the background is made up of several overlapping contributions and so tends to be smooth in the region of the η mass, hence the η step usually

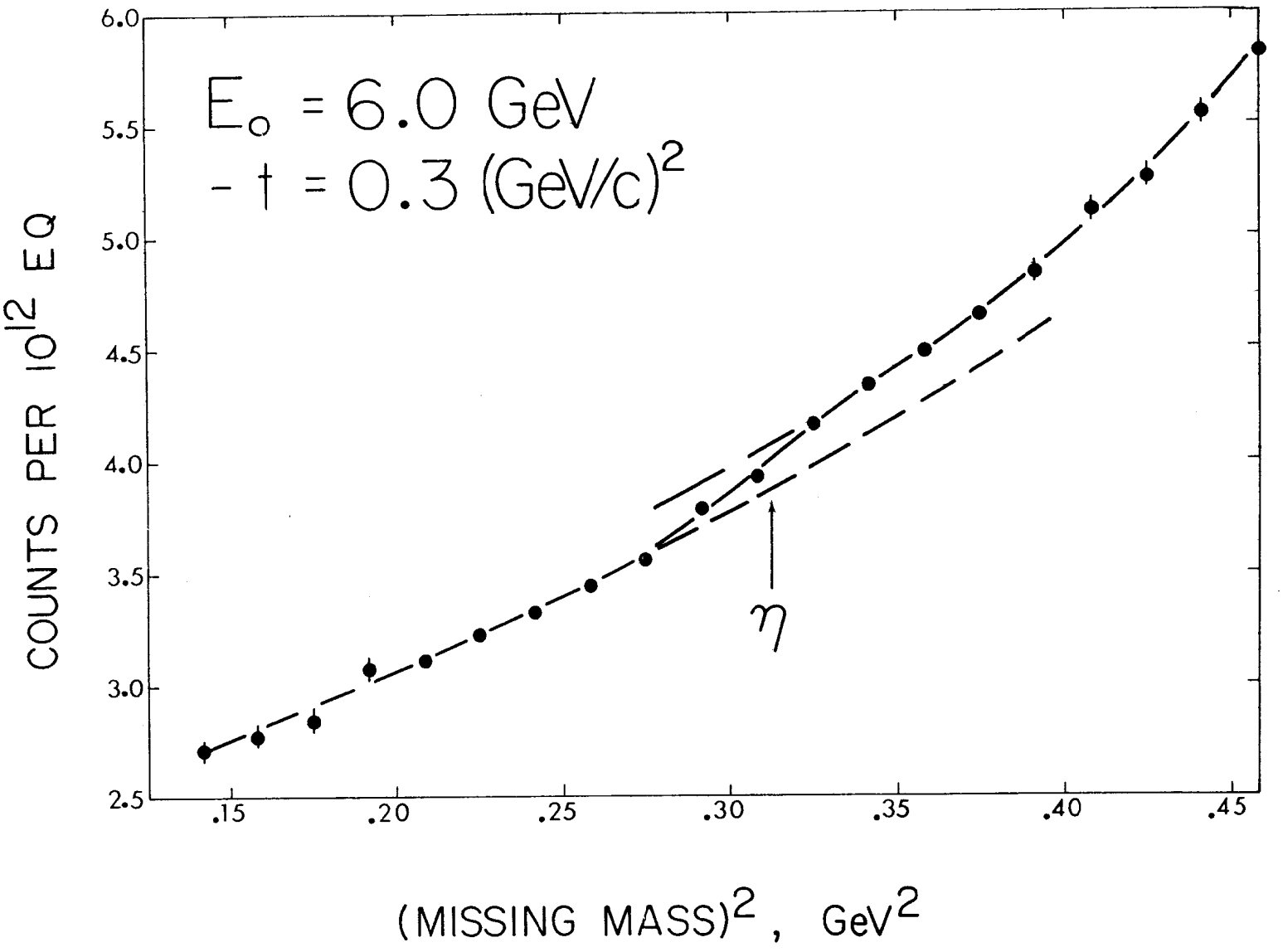

FIG. 14a--Sample η fits.

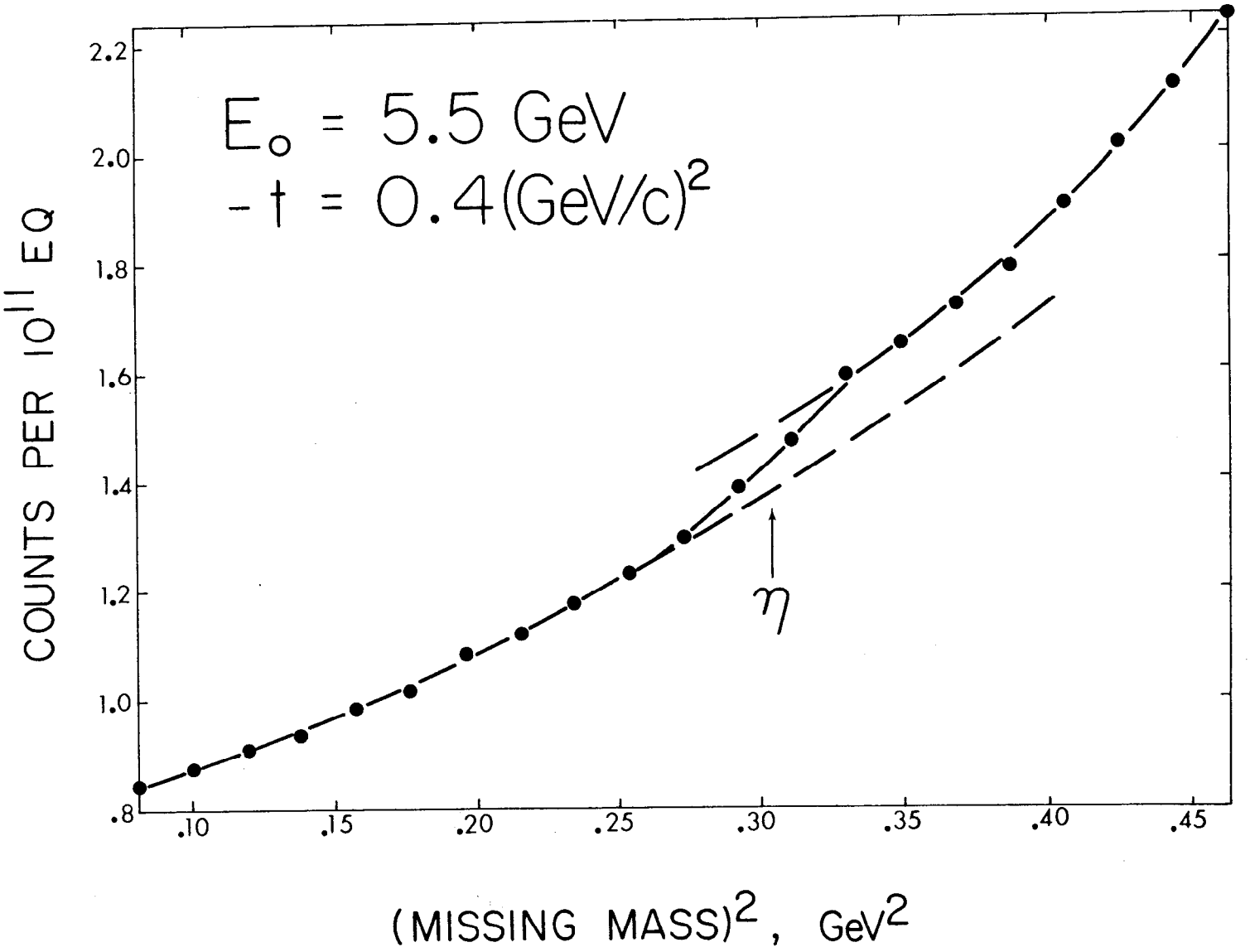

FIG. 14b--Sample η fits.

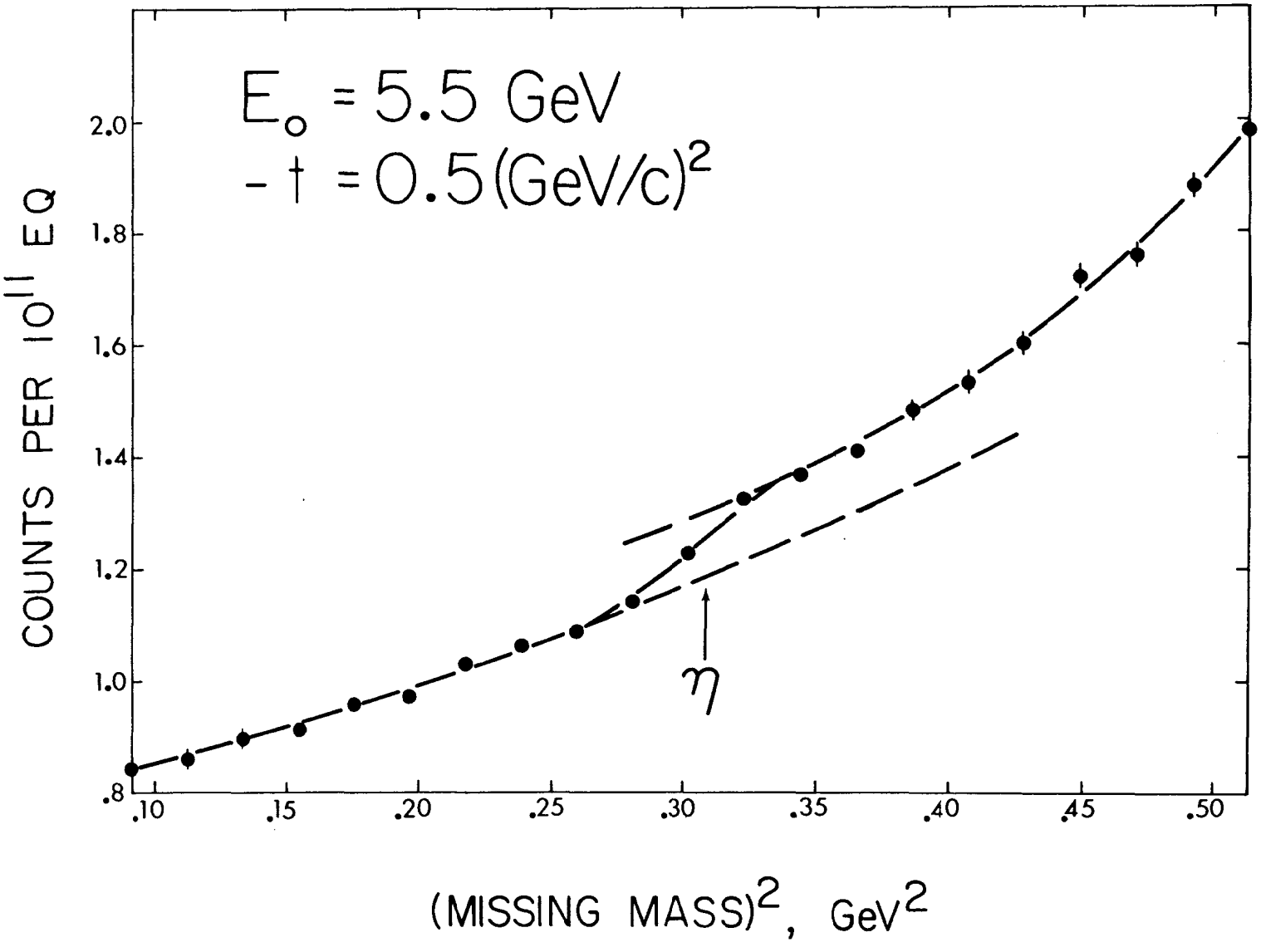

FIG. 14c--Sample η fits.

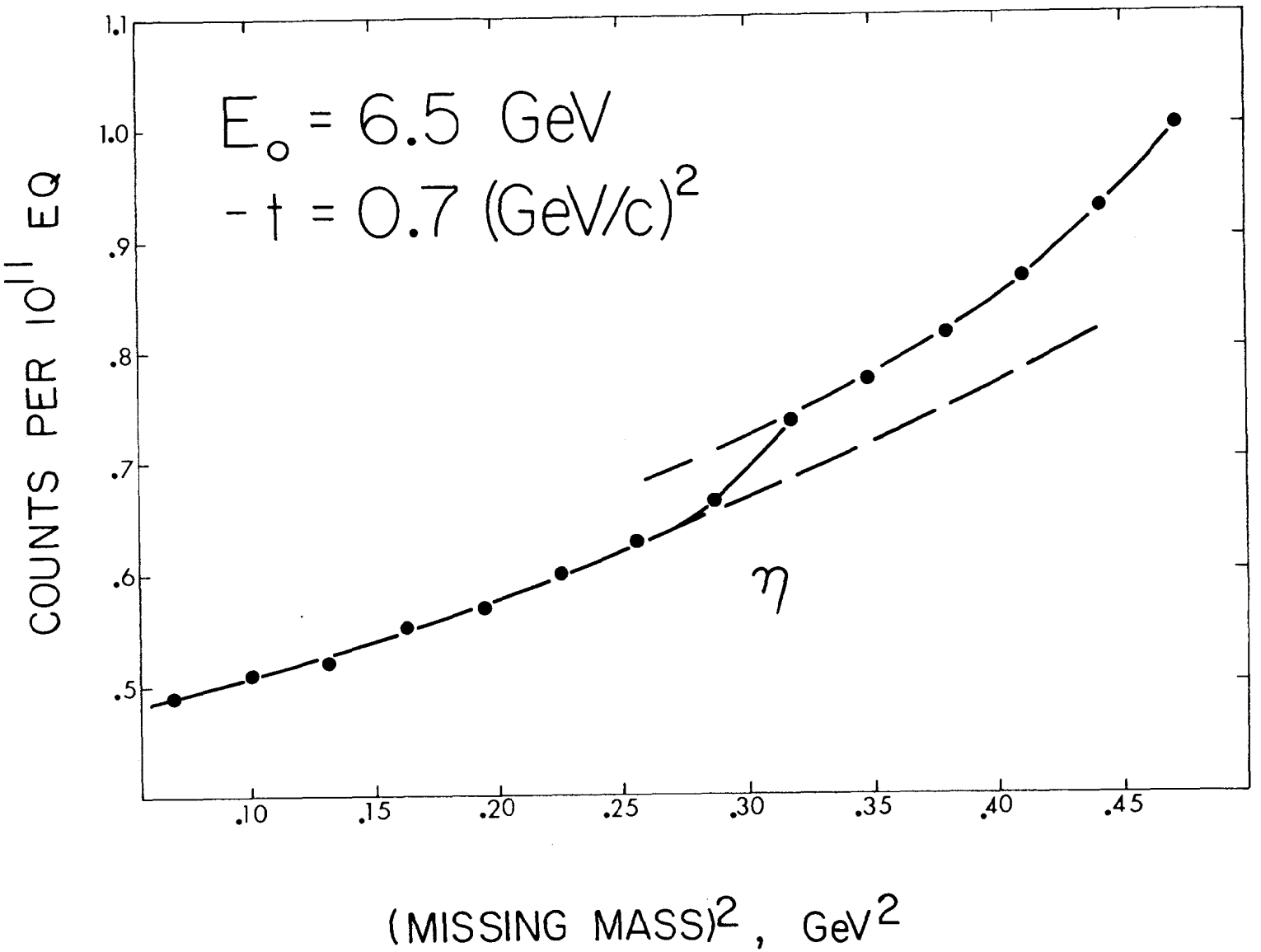

FIG. 14d--Sample η fits.

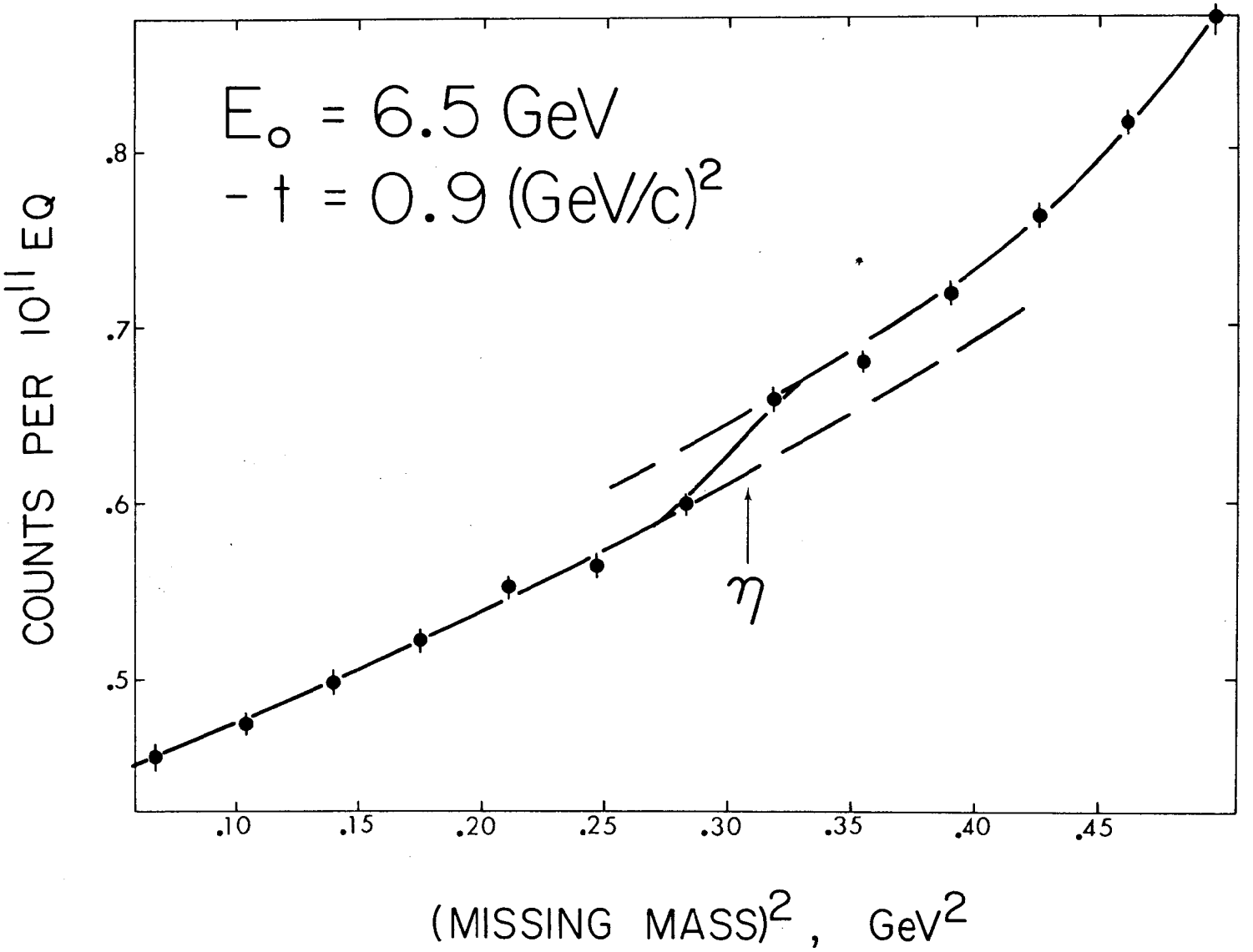

FIG. 14e--Sample η fits.

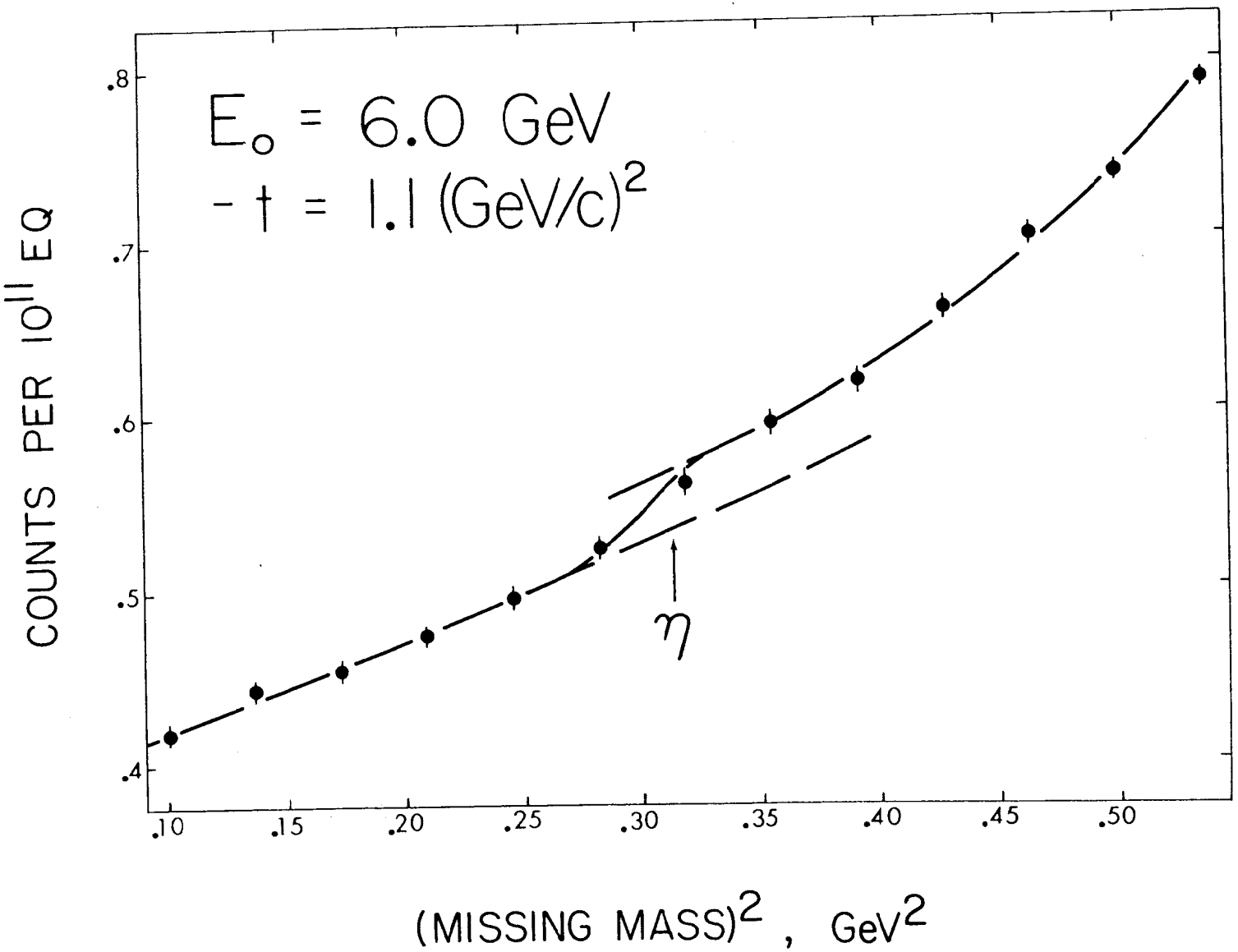

FIG. 14f--Sample η fits.

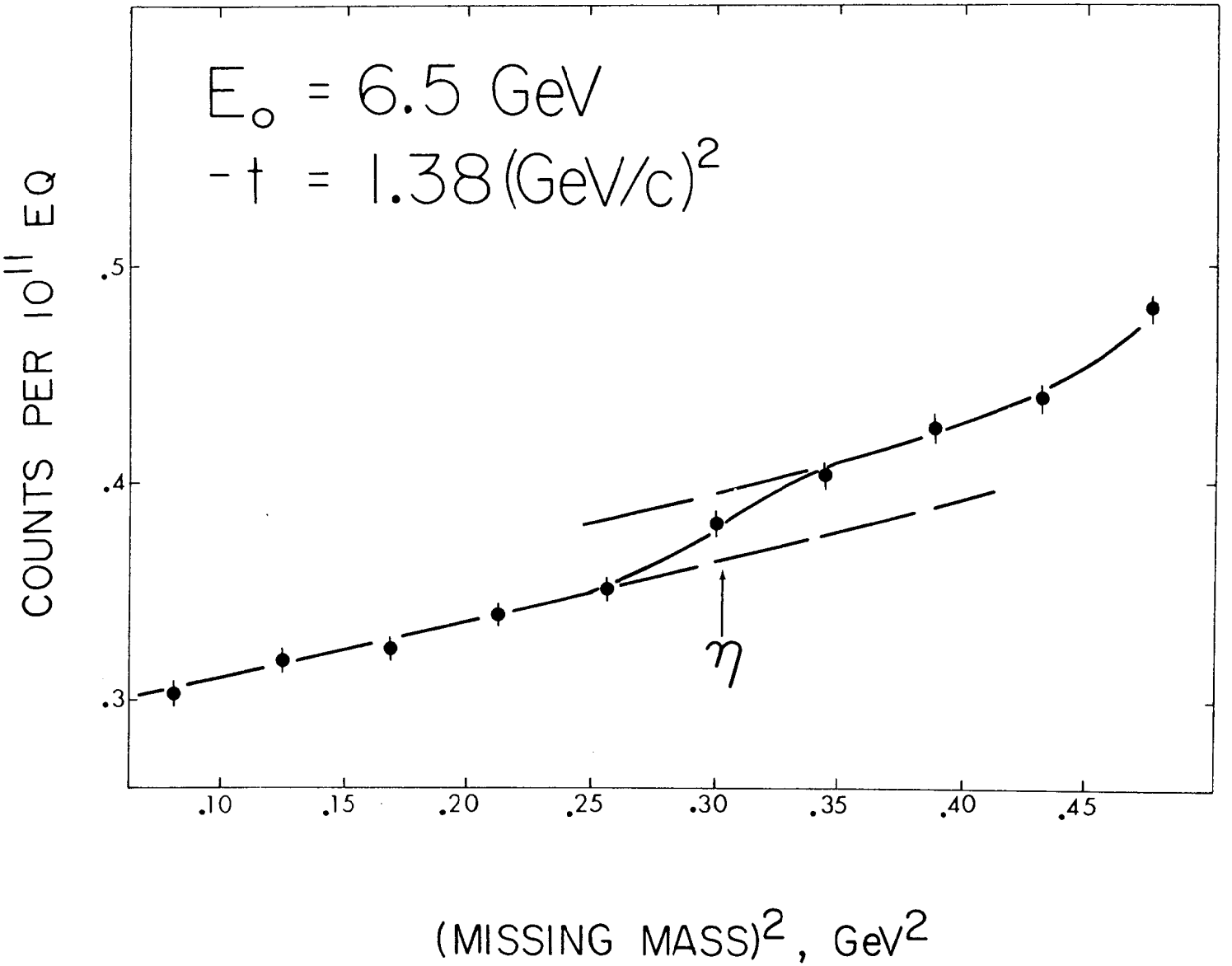

FIG. 14g--Sample η fits.

appears (if at all) as a break in an otherwise smooth curve. As it turned out, this could be fit with the same functions as the π^0, with the η mass replacing the π^0 mass in the kinematics: a quadratic for the background (all three terms needed), plus a step η yield with multiple scattering, plus an additional quadratic term starting somewhere above the η mass. This last term was needed as the ρ^0 yield began to contribute heavily, creating more curvature. The different parts of the fit are not shown separately in the figure, but the results above and below the η mass have been extrapolated past the step (the lower curve is actually the background polynomial) to emphasize the "break in a smooth curve". This is in fact how one would make a fit by eye using a French curve; the computer has simply minimized the chi-square in doing so.

For all π^0 and η fits, the computer also calculated statistical errors on the least-squares coefficients. In general, these errors could not be used directly, as the calculation assumed absolute accuracy for the fitting functions used. It was then necessary to determine what the uncertainty in a step height would be, due to reasonable uncertainty as to the precise position and resolution of the step, for example. The final quoted error on each point thus include statistics plus the author's judgment of the accuracy of the input parameters and the quality of the fit.

C. Corrections

The step heights extracted as described in the last section were converted to cross sections by the calculation in the Appendix. The resulting cross section values still were subject to correction for certain effects, some of which have already been discussed, such as dead-time losses, absorption of protons in the counters, and proton events vetoed by the Cerenkov counter. The handling of the Compton correction has also been mentioned.

In addition to the losses listed above, there were counter inefficiencies to be considered. The absolute efficiency of the hodoscope was determined by comparing the summed hodoscope coincidences to the trigger rate in a region where the proton rate was flat. The ratio should have been the same as the area of the whole hodoscope divided by the area of the smallest trigger counter. Assuming the elements to be exactly 0.75 inches by 10.0 inches, as assumed in the cross section calculation, there was thus found to be an average effective inefficiency of 2.5%. Also, counter 12 was found to cause approximately a 4% decrease in hodoscope rate when it was switched into the trigger coincidence (with a clean proton signal already defined). A further correction was necessary due to losses in the photon beam from pair production in materials upstream of the target, such as beam pipe windows, the SEM and Cerenkov monitors, air, and half the hydrogen in the target itself. Such pairs will record in the SEQ, but will not contribute to the measured yield (although electron scattering is kinematically similar to π^0 photoproduction, the energy spectrum of the electrons in this case does not have a sharp rise at the endpoint, so they cannot produce a step).

Finally, there is a correction to the momentum acceptance assumed in converting to cross sections. In traversing a given amount of material, a proton of higher initial momentum loses less momentum than a lower-momentum proton, and the difference thus becomes greater. Hence a given spread in recoil proton momentum accepted by the spectrometer corresponds to a smaller spread at the center of the target, where the protons originate. This effect can be quite considerable for low momenta. A simple computer routine was written to calculate this effect, and to determine what spectrometer momentum should be set to correspond to a desired t-value at the center of the target.

This made use of the fact that the range R (in a given material) of a particle of mass M and momentum p can be written

$$R/M = K(p/M)^{\delta}$$

where K and δ are very slowly varying functions of (p/M). Then starting with a desired center-of-target momentum, ranges were calculated for momenta 2% above and below this, the increment of range corresponding to the material to be traversed was subtracted from each, and the final momenta were calculated by inverting the formula. The desired ratio of $\Delta p/p$ in and out of the target was independent of the initial $\Delta p/p$ chosen.

The various corrections and normalization uncertainties are summarized in Table I. A blank entry indicates the correction does not apply; a dash indicates it was found to be negligible. Typically the net correction was between 10 and 20%, and the combined normalization uncertainty is approximately 5%.

TABLE I

Corrections and Normalization Uncertainties (%)

$\|t\|$, $(GeV/c)^2$	Absorption Losses		C_π	C-12 Losses	Hodoscope	Δp/p Acceptance Correction		Photon Conversion Losses		Solid	Beam	Dead-
	Gas Target	Liquid Target	Veto Losses	(Gas Target)	Inefficiency	Gas Target	Liquid Target	Gas Target	Liquid Target	Angle Calib.	Monitor Calib.	time Losses
0.1	3 ±1				2.5 ± 1	8.5		1.6		± 3	± 2	≤ 5 ± 2
0.15	2.5±1				2.5 ± 1	4		1.6		± 3	± 2	≤ 5 ± 2
0.2	2 ±1	3 ± 1			2.5 ± 1	2	7.5	1.6	3.1	± 3	± 2	≤ 5 ± 2
0.3	8 ±2	8 ± 2		4 ± 2	2.5 ± 1	1	3.5	1.6	3.1	± 3	± 2	≤ 5 ± 2
0.4	6 ±2	6 ± 2	---	4 ± 2	2.5 ± 1	1	2	1.6	3.1	± 3	± 2	≤ 5 ± 2
0.5		4 ± 1	---		2.5 ± 1		1.5		3.1	± 3	± 2	≤ 5 ± 2
0.6		3 ± 1	---		2.5 ± 1		1		3.1	± 3	± 2	≤ 5 ± 2
0.7		2 ± 1	1 ±1		2.5 ± 1		1		3.1	± 3	± 2	≤ 5 ± 2
0.8		2 ± 1	1 ±1		2.5 ± 1		---		3.1	± 3	± 2	≤ 5 ± 2
0.9		1 ± 1	1.5±1		2.5 ± 1		---		3.1	± 3	± 2	≤ 5 ± 2
1.1		1 ± 1	3 ±1		2.5 ± 1		---		3.1	± 3	± 2	≤ 5 ± 2
1.4		1 ± 1	6 ±2		2.5 ± 1		---		3.1	± 3	± 2	≤ 5 ± 2

V. RESULTS AND DISCUSSION

A. π^o Results

The final π^o photoproduction cross sections are shown in Fig. 15, with $d\sigma/dt$ in $\mu b/(GeV/c)^2$ plotted against the beam energy E_0 in GeV on a log-log scale for each value of t. Where more than one measurement was made at a particular energy and t-value, the results have been averaged. The energy dependence is variously discussed in the literature in terms of s, s-u, or $s-M_p^2$, where s,t, and u are the Mandelstam variables, defined in terms of the four momenta for a process $1 + 2 \rightarrow 3 + 4$ as

$$s = (P_1 + P_2)^2$$

$$t = (P_1 - P_3)^2 = (P_2 - P_4)^2$$

$$u = (P_1 - P_4)^2 \quad .$$

In this case $s = 2M_pE_0 + M_p^2$, $s-u = 4M_pE_0 - \left(|t| + M_\pi^2\right)$, and $s-M_p^2 = 2M_pE_0$, so that each of these combinations is closely or exactly proportional to E_0. Thus the Regge theory prediction that $d\sigma/dt \sim s^{2\alpha(t)-2}$ at high energies is borne out by the results, since for each value of t the plots in Fig. 15 may be least-squares fitted to a straight line with a good value for the chi-square, as shown by the solid lines in the figure. The slope of each line has been set equal to $2\alpha-2$, and the value of α is given in each case.

In Fig. 16 the effective $\alpha(t)$, determined as just described, has been plotted versus t. The solid line represents a least-squares fit to a straight line, given by $\alpha(t) = 0.18 + 0.26t$. The reduced chi-square of the fit is equal to 2.0, but there is a large contribution to this from the single point at $t=-0.3$. The dashed line represents the $\alpha(t)$ expected for pure ω-exchange.

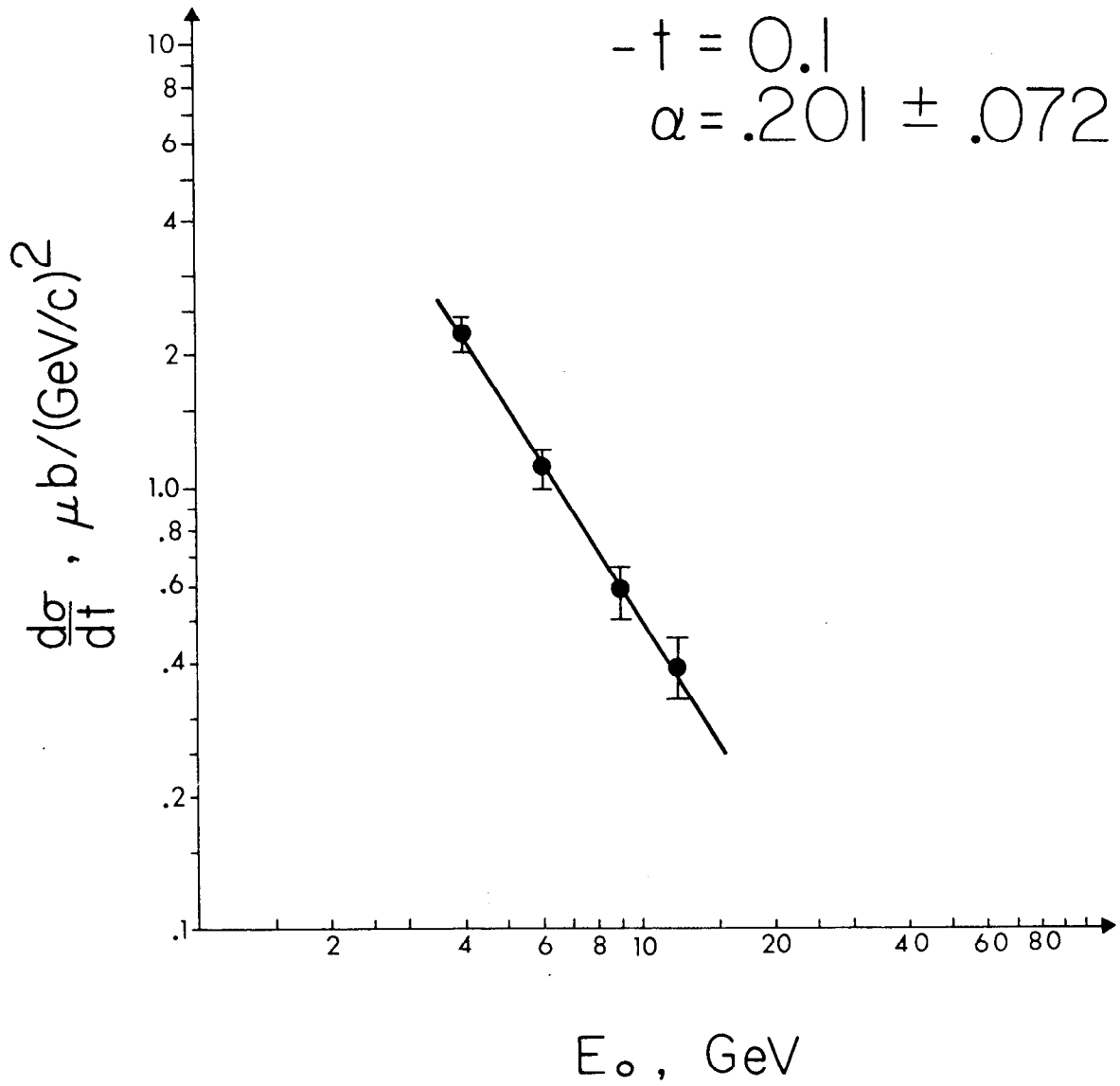

FIG. 15a--Cross sections for $\gamma + p \rightarrow \pi^o + p$.

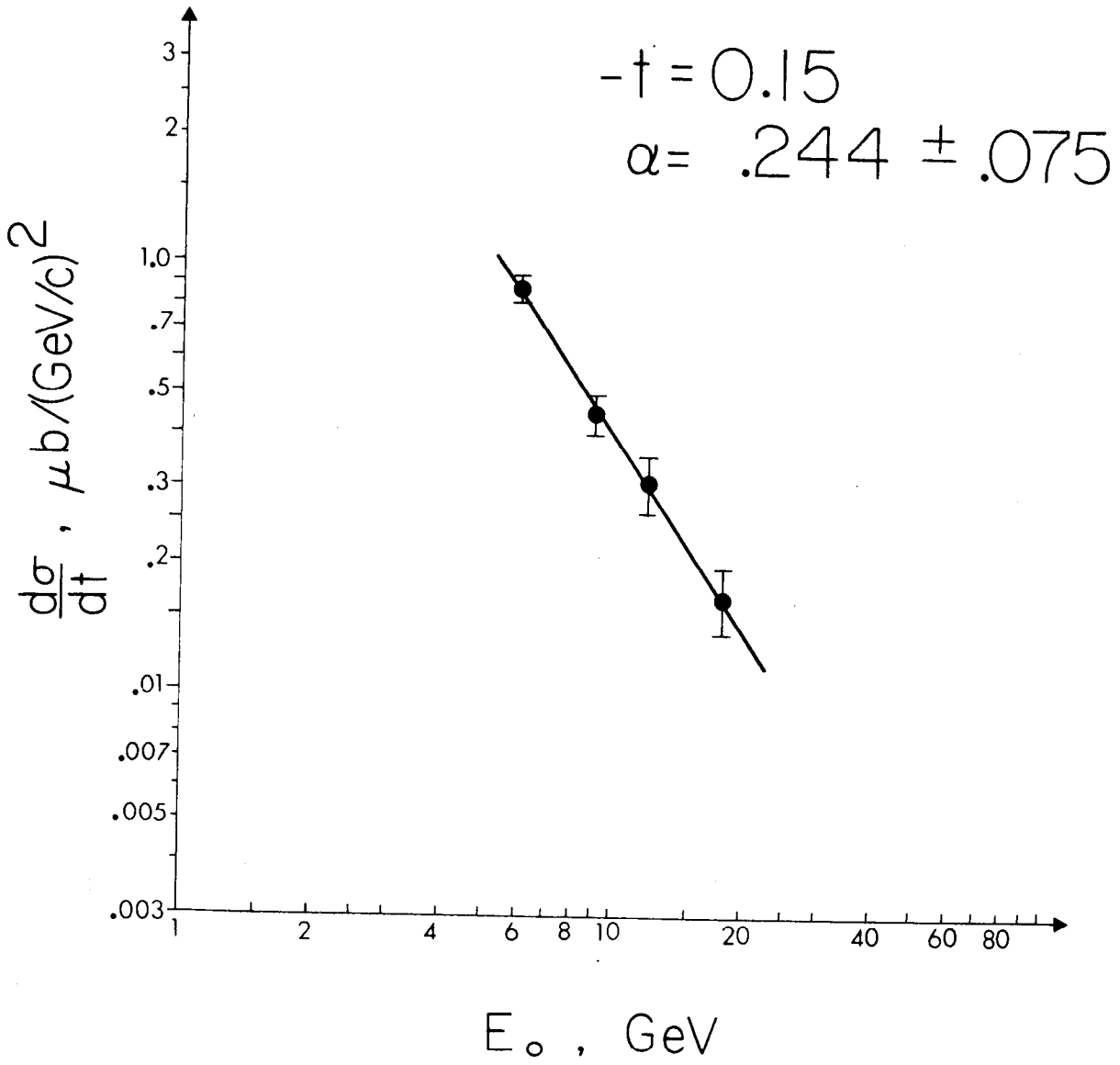

FIG. 15b--Cross sections for $\gamma + p \rightarrow \pi^o + p$.

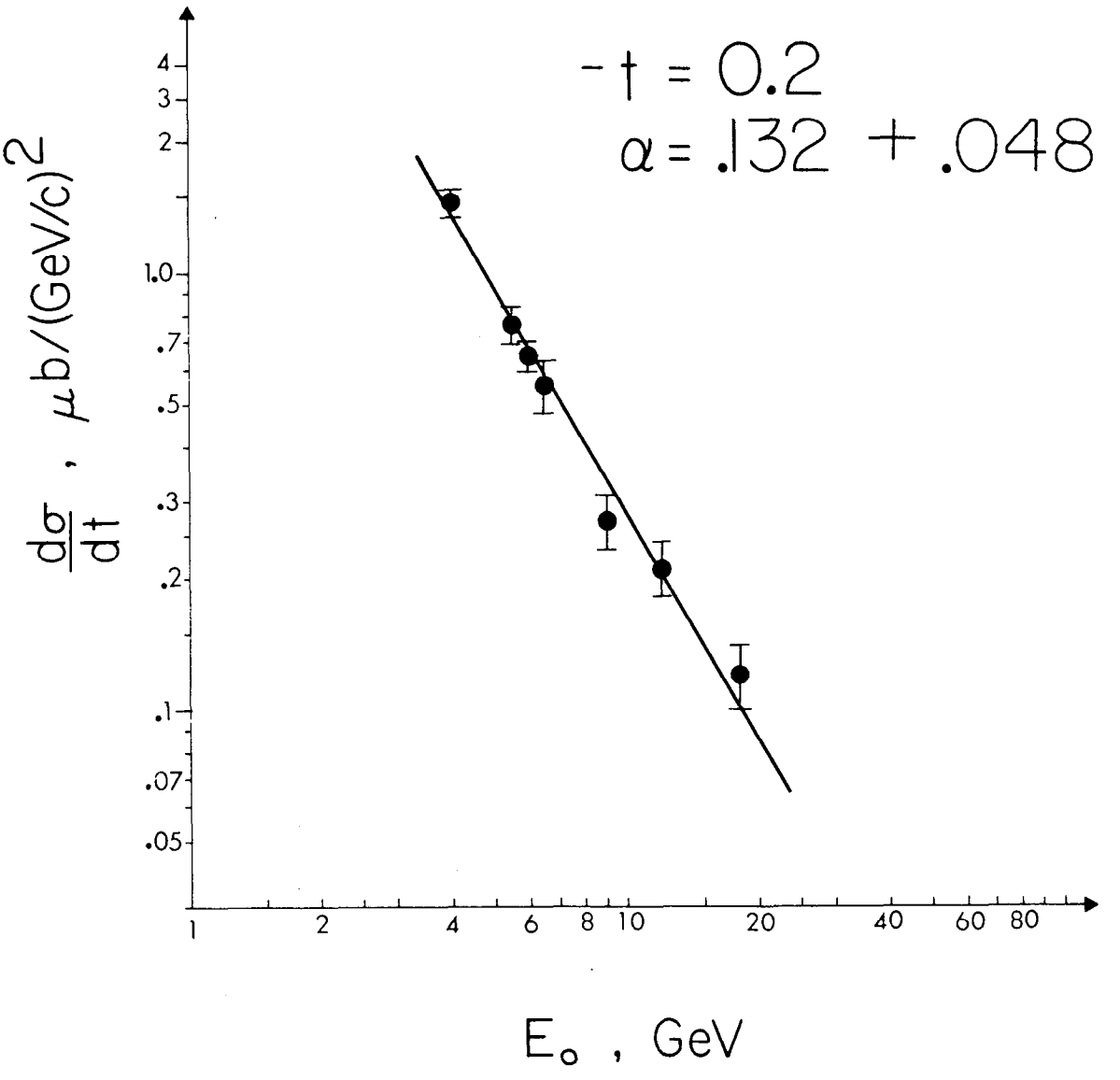

FIG. 15c--Cross sections for $\gamma + p \rightarrow \pi^o + p$.

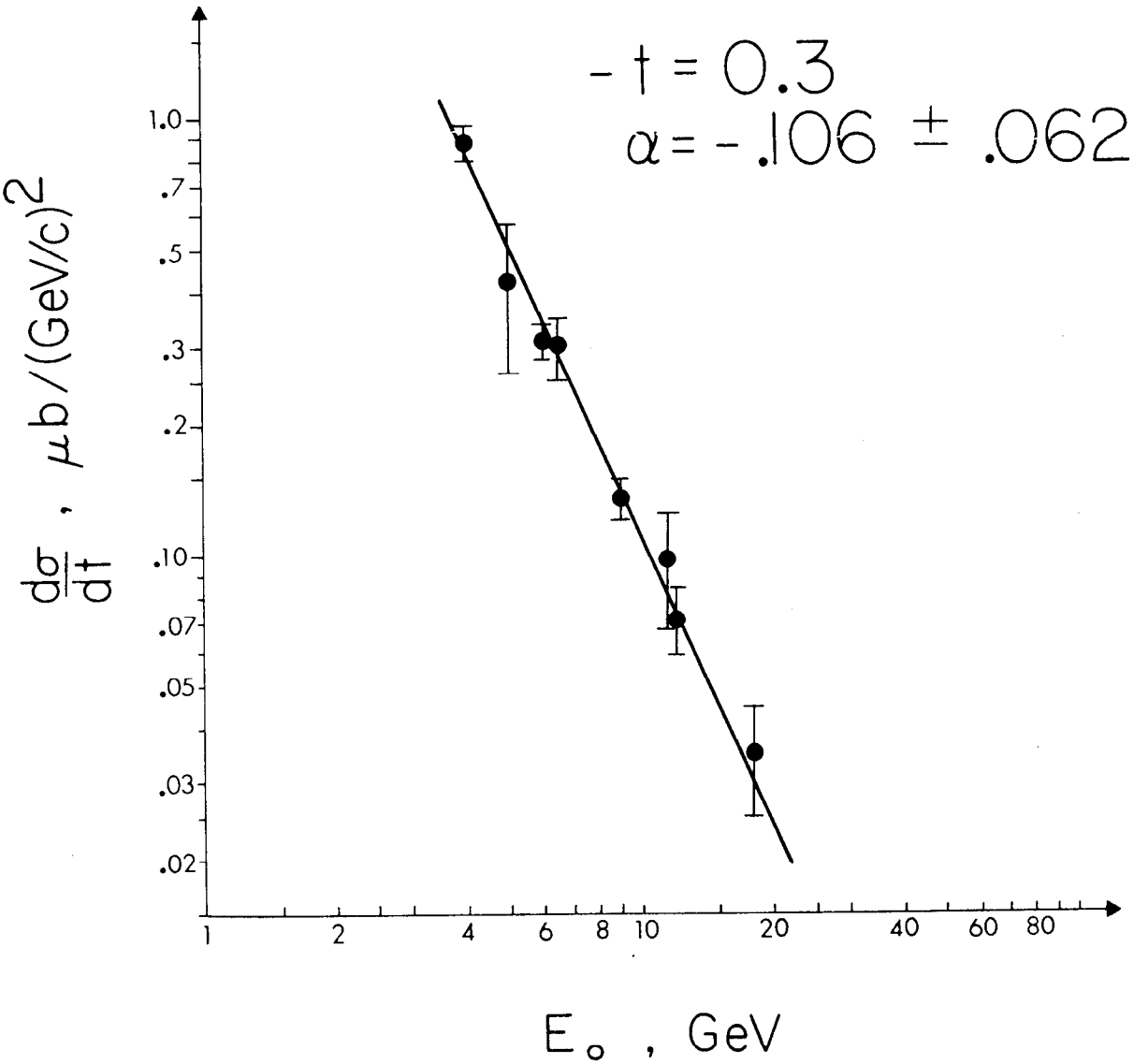

FIG. 15d--Cross sections for $\gamma + p \rightarrow \pi^{o} + p$.

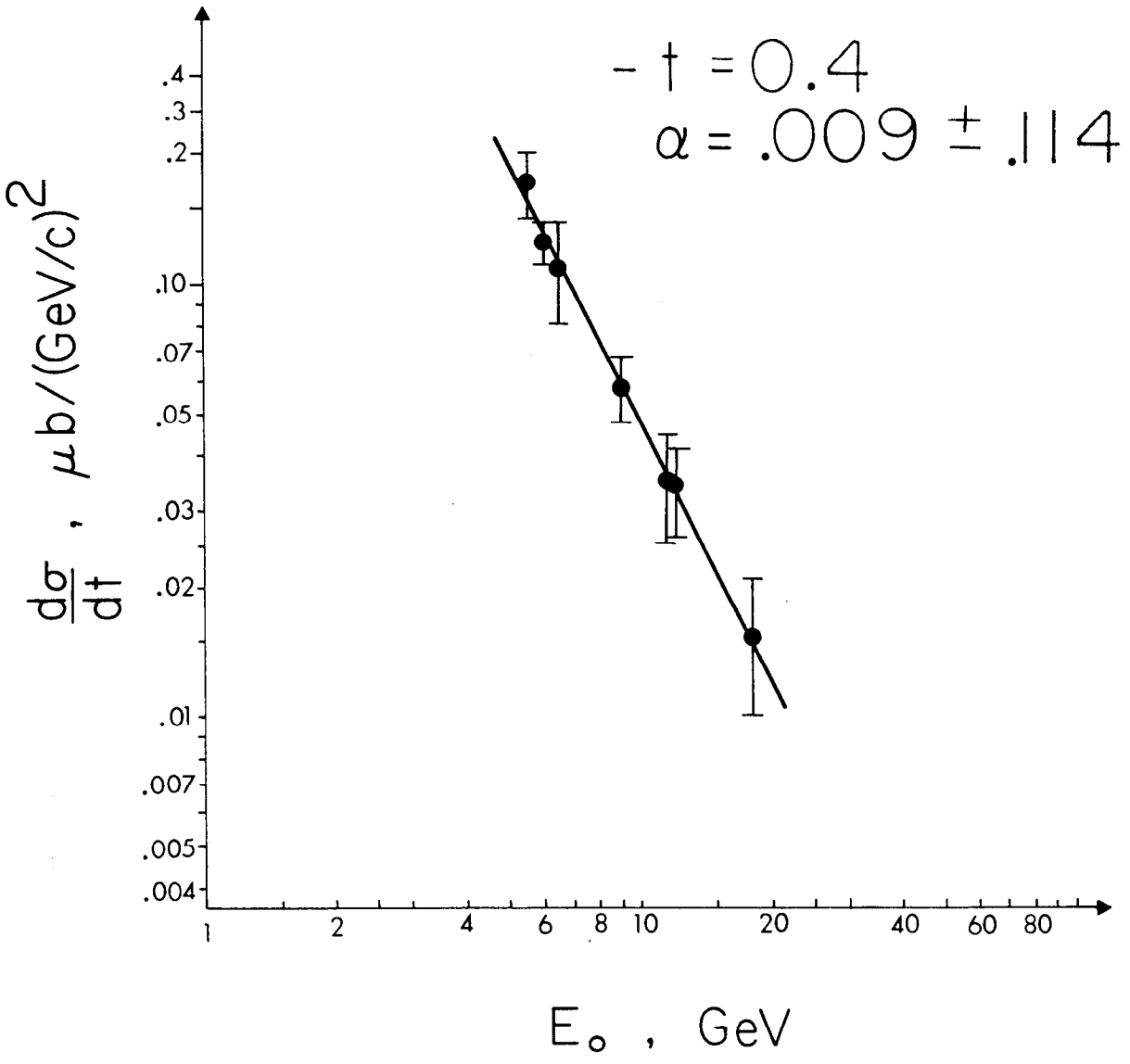

FIG. 15e--Cross sections for $\gamma + p \rightarrow \pi^o + p$.

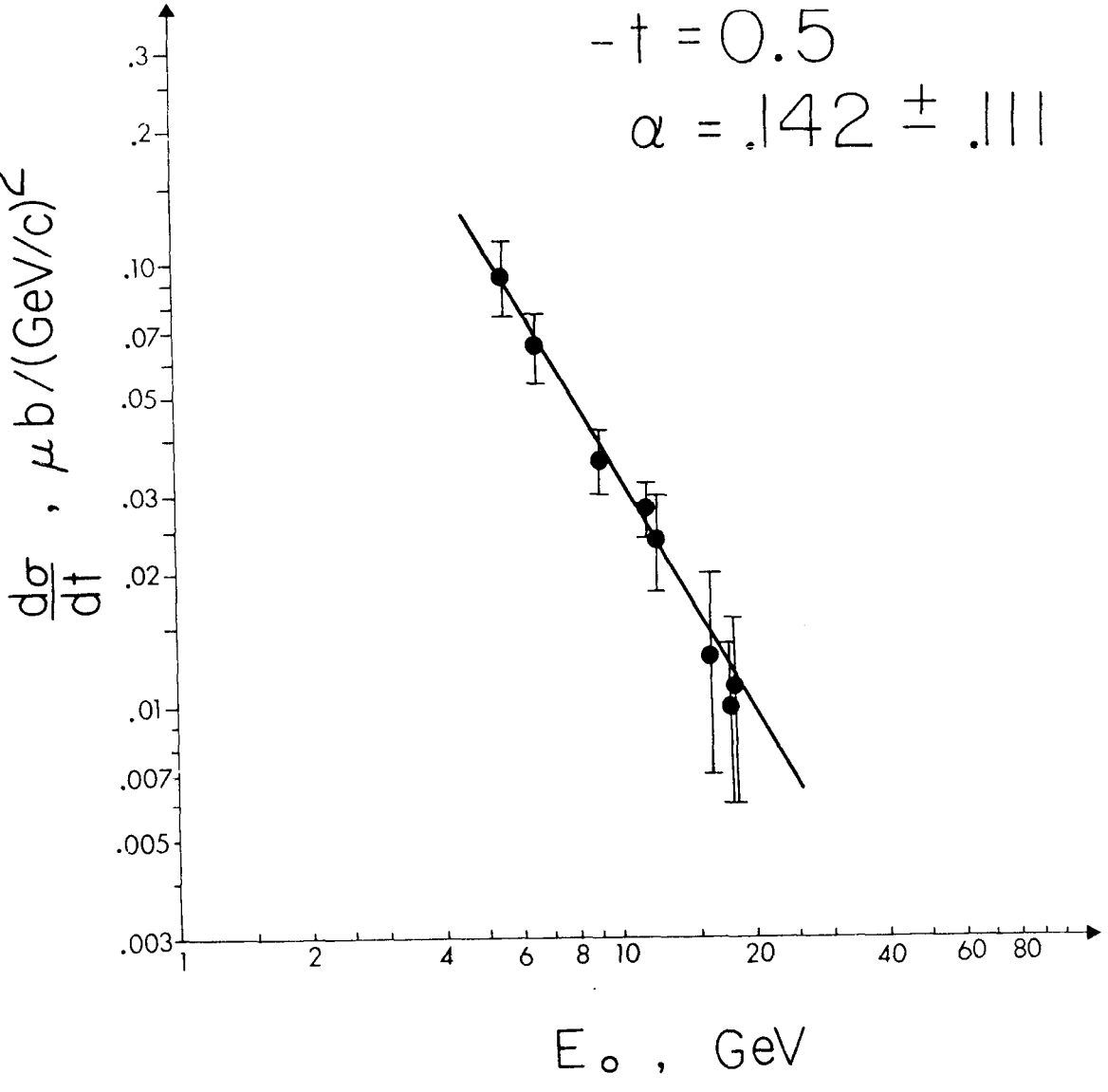

FIG. 15f--Cross sections for $\gamma + p \rightarrow \pi^o + p$.

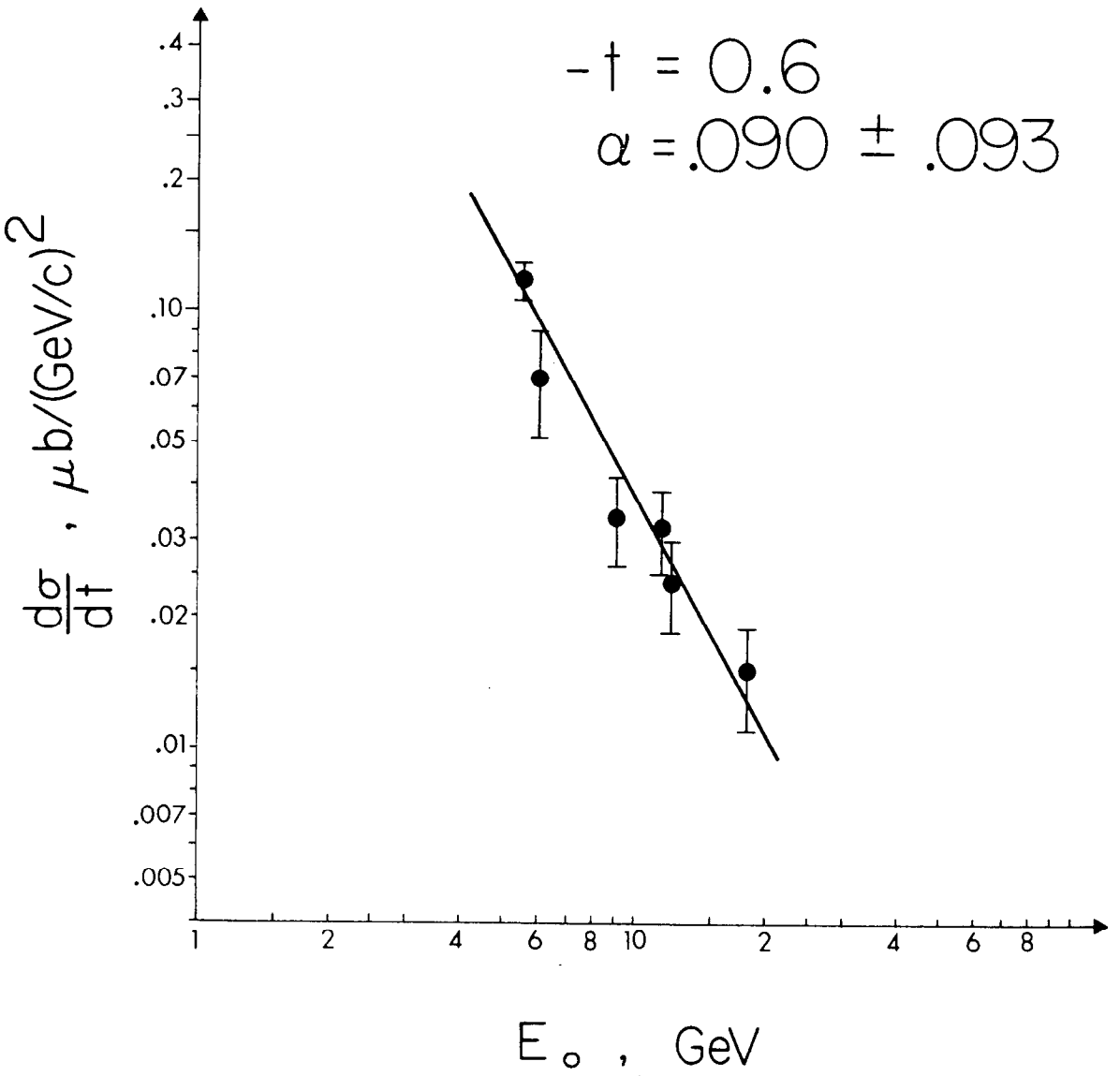

FIG. 15g--Cross sections for $\gamma + p \rightarrow \pi^o + p$.

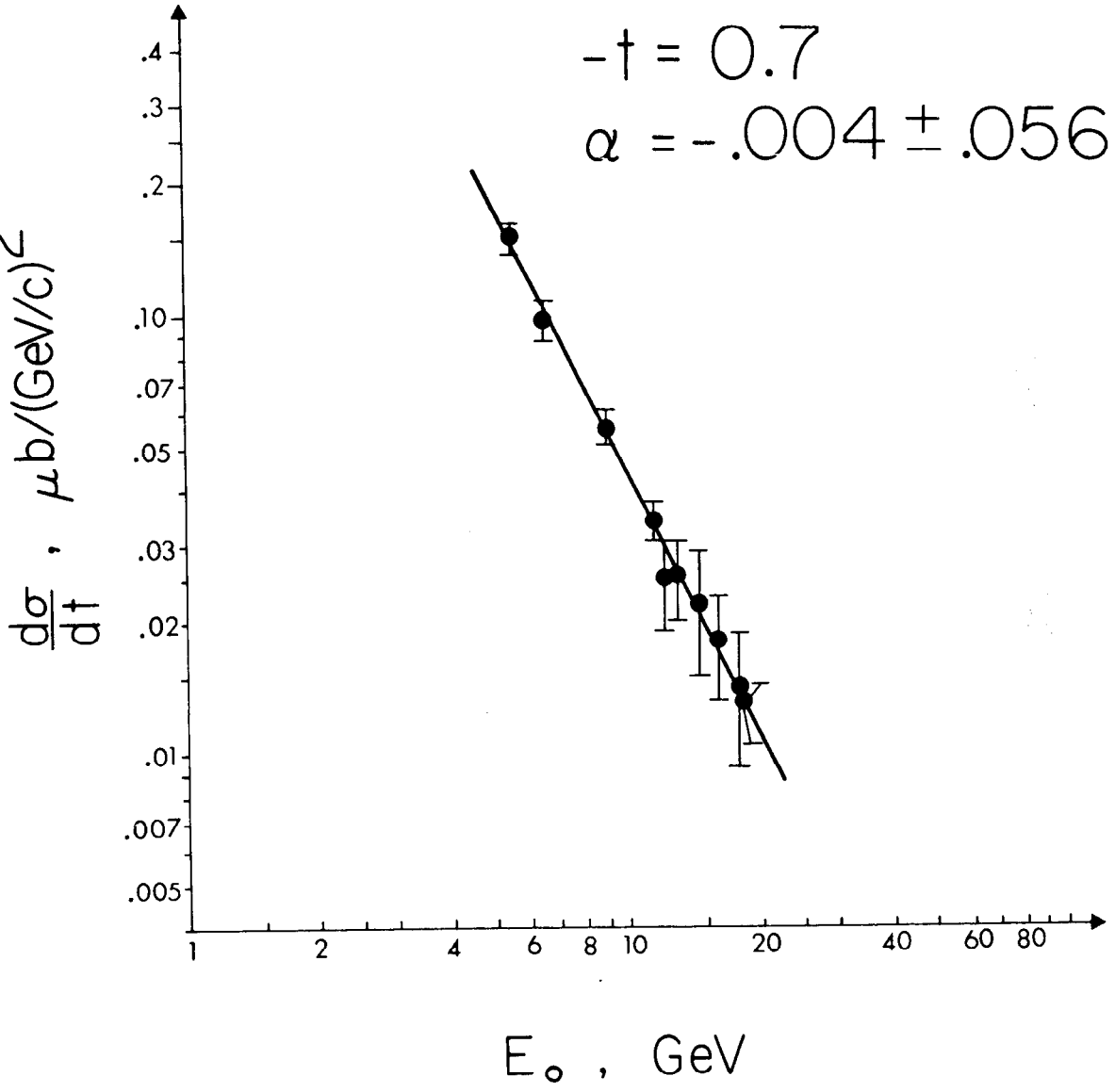

FIG. 15h--Cross sections for $\gamma + p \rightarrow \pi^o + p$.

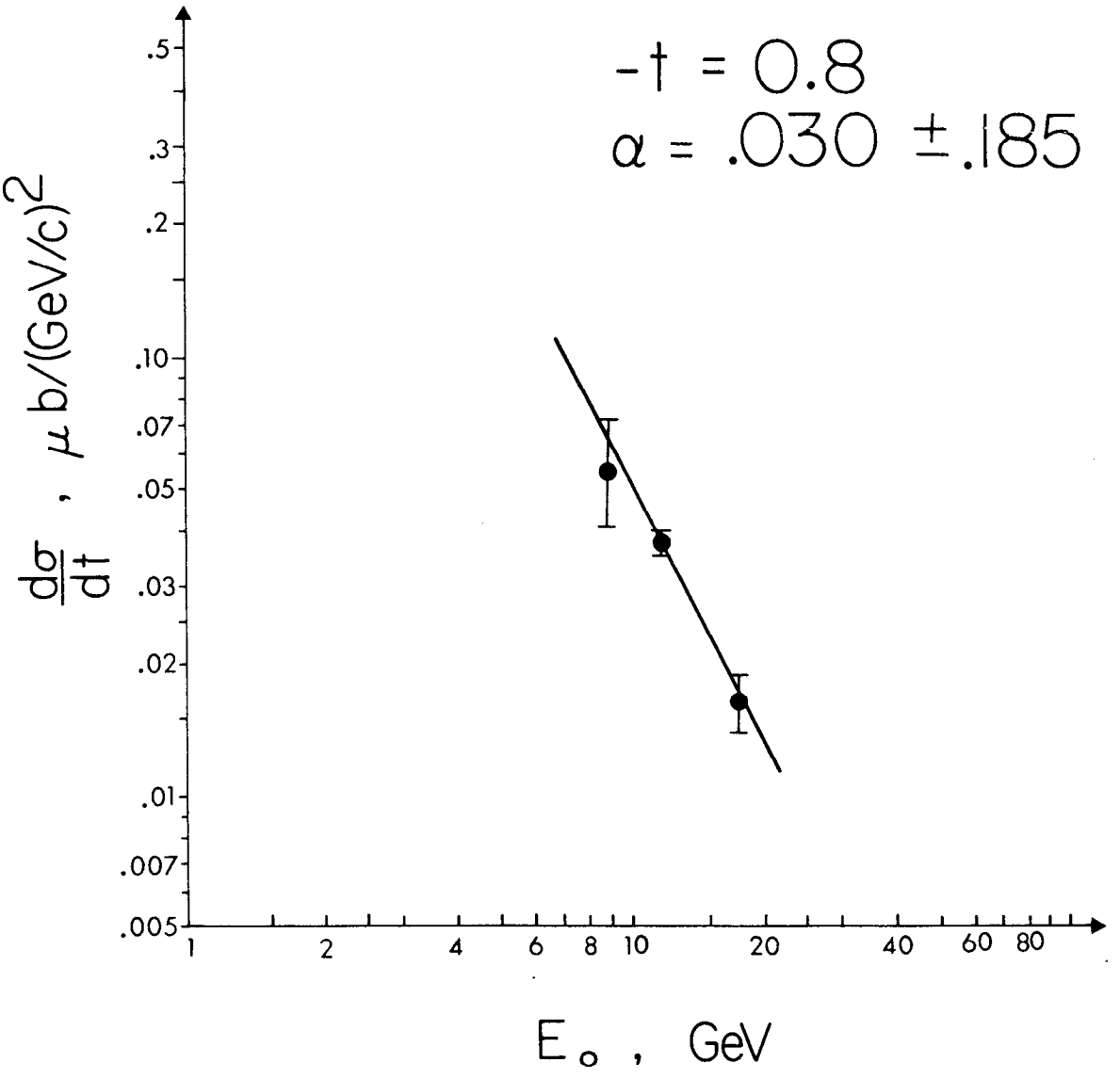

FIG. 15i--Cross sections for $\gamma + p \rightarrow \pi^o + p$.

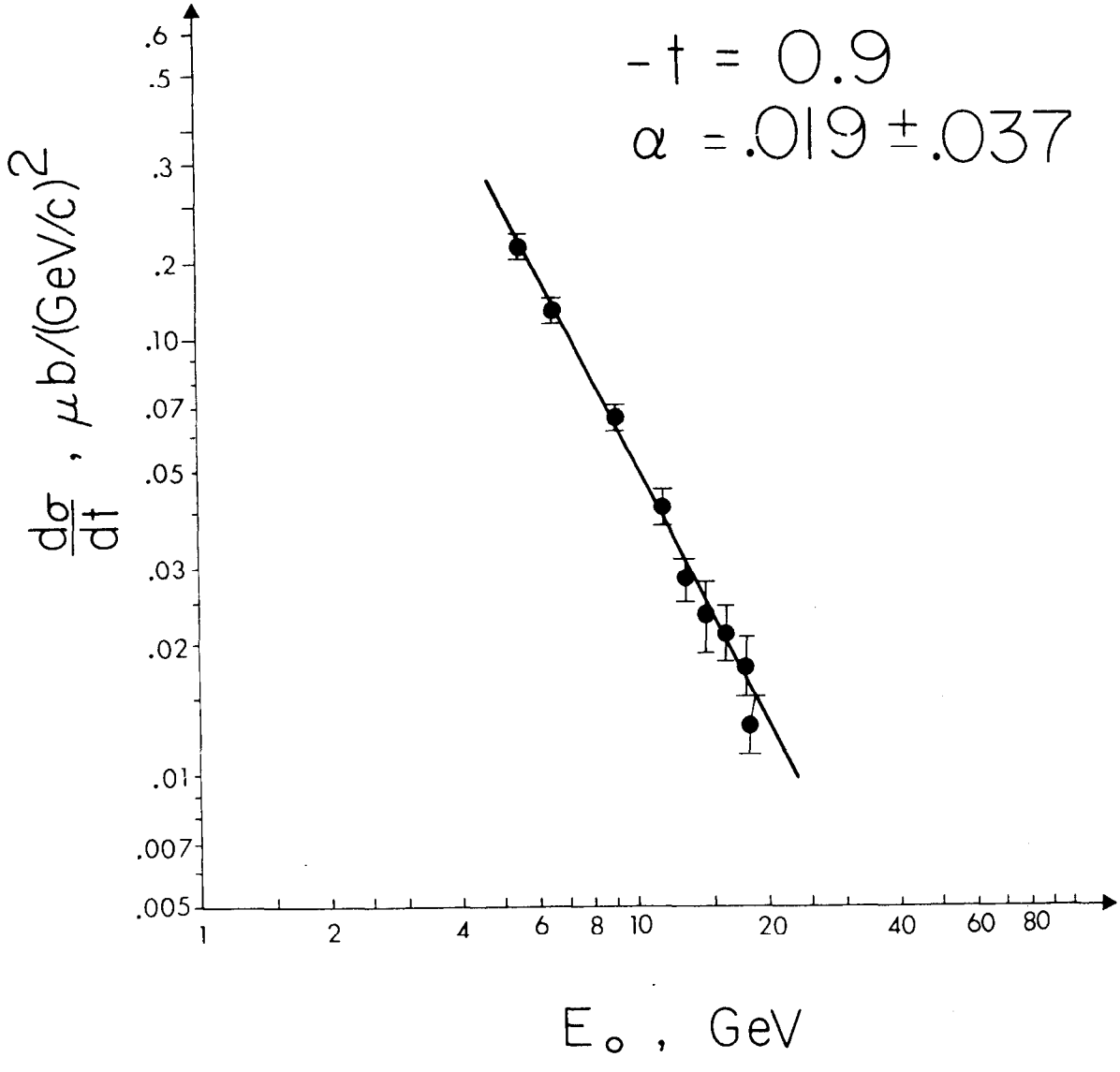

FIG. 15j--Cross sections for $\gamma + p \rightarrow \pi^o + p$.

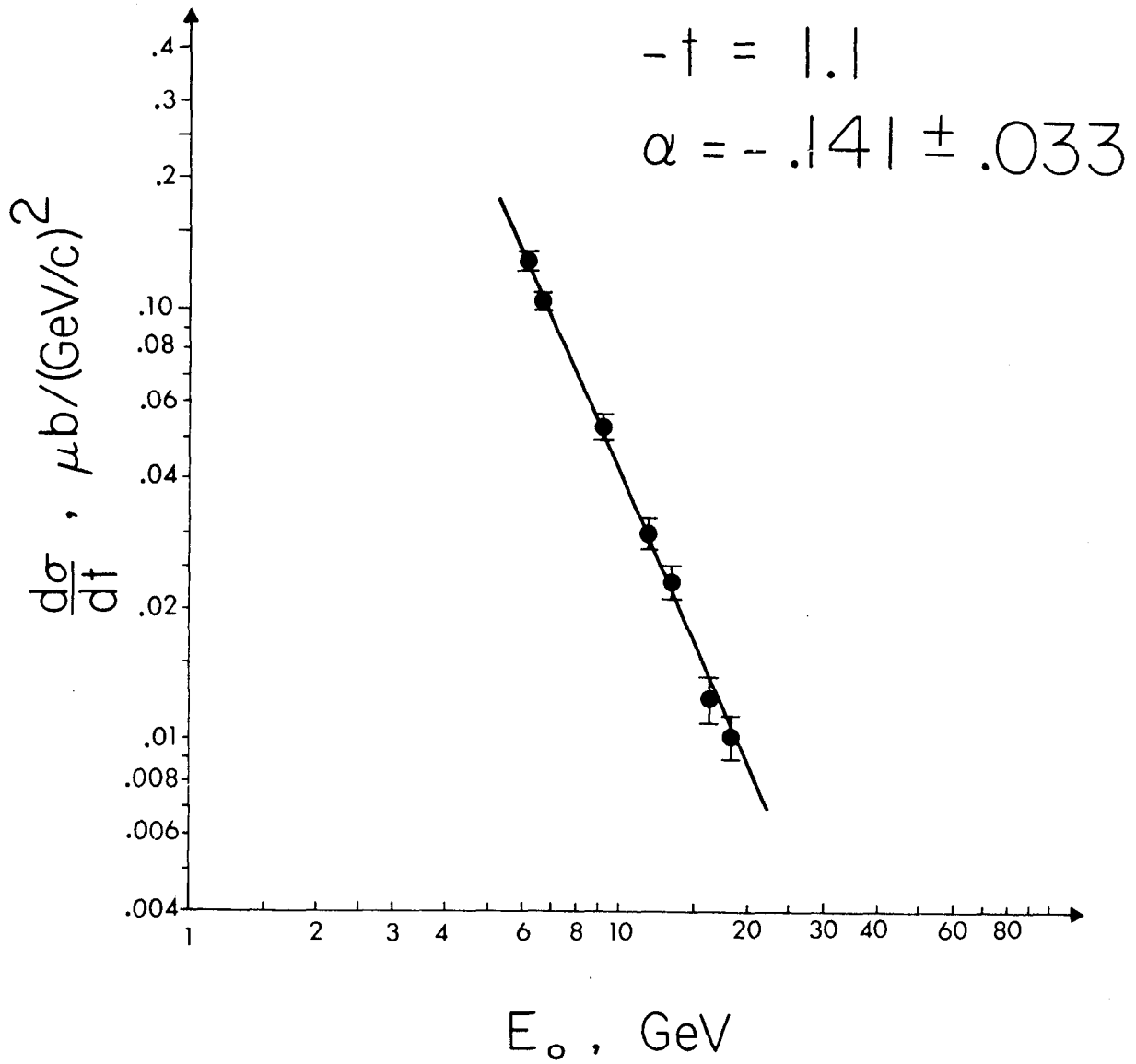

FIG. 15k--Cross sections for $\gamma + p \rightarrow \pi^o + p$.

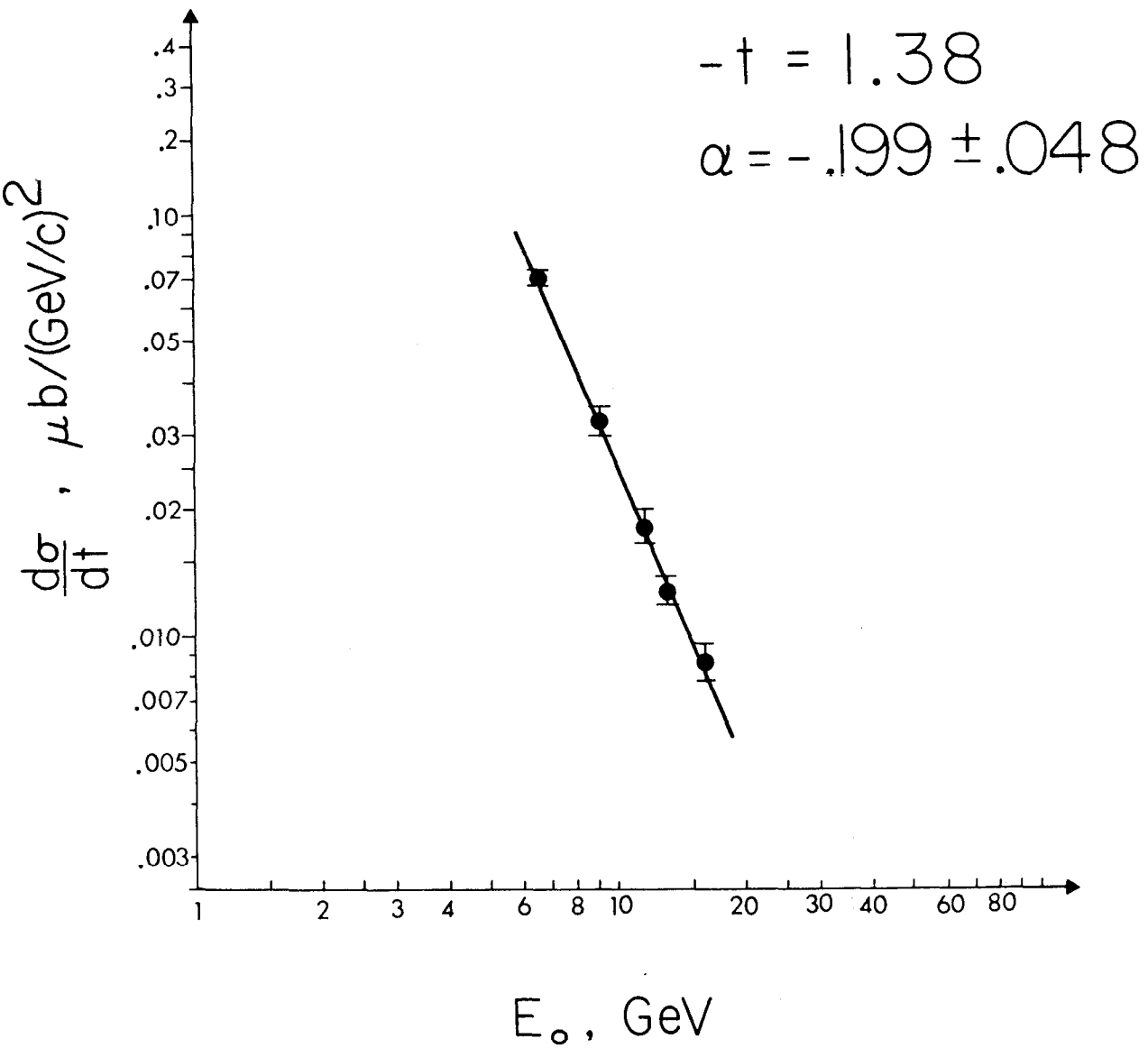

FIG. 151--Cross sections for $\gamma + p \rightarrow \pi^{o} + p$.

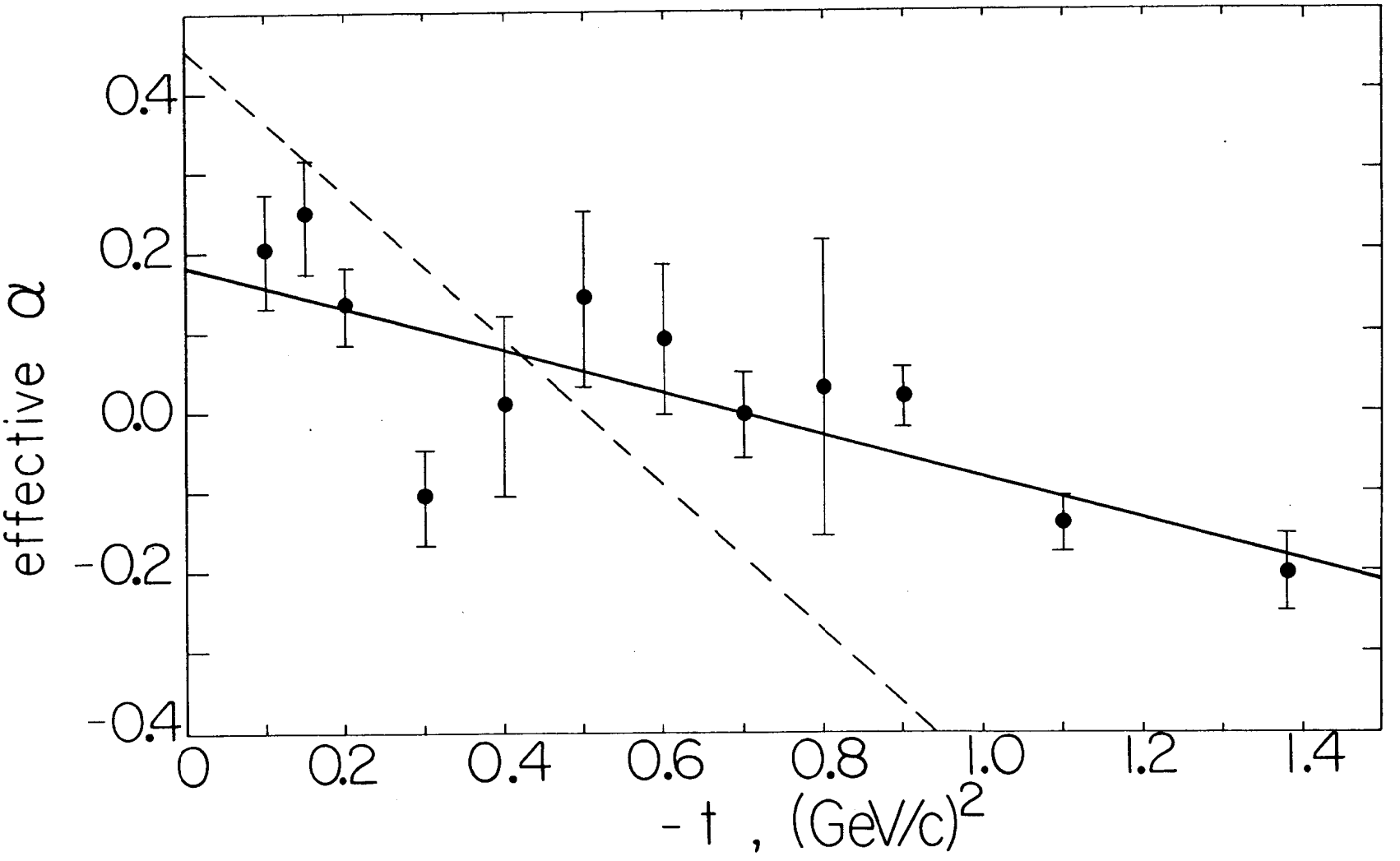

FIG. 16--Effective $\alpha(t)$ for $\gamma + p \rightarrow \pi^o + p$.

Although the cross sections shown in Fig. 15 were measured at many different energies, complete angular distributions at fixed values of E_0 may be obtained by taking values from the straight-line fits, which represent the data very well. The results have thus been summarized for energies of 6, 9, 12, and 15 GeV and the full range of t (18 GeV would have required extrapolation at some values of t), and these angular distributions are shown in Fig. 17. The dashed lines through the various sets of points are only to guide the eye. The numerical values of the points are presented in Table II. With increasing t the cross section decreases sharply past $|t| = 0.1$ $(GeV/c)^2$, reaches a local minimum around $|t| = 0.5$, then a local maximum around $|t| = 0.85$, and finally shows a comparatively gentle decrease out to $|t| = 1.4$. This behavior of the angular distributions does not appear to change much with energy, which is equivalent to pointing out that $\alpha(t)$ does not vary rapidly, as seen previously.

Figure 18 shows a comparison of these angular distributions with results from DESY, where the latter have been taken from the most recent available summary (Ref. 20). The cross sections $d\sigma/dt$ have been multiplied by $\left(s-M_p^2\right)^2 \sim E_0^2$; thus to the extent that α stays close to zero, all the distributions should fall approximately on top of one another. The agreement is quite satisfactory, considering that α is observed to be different from zero at low $|t|$ and that the two experiments for the most part cover different energy ranges. The DESY experiment detected the decay photons from the π^o.

Figure 19 shows a comparison of $\left(s-M_p^2\right)^2$ $d\sigma/dt$ with results (as yet unpublished) from a group at the California Institute of Technology (Ref. 21). The experiment was performed at SLAC using the 8 GeV/c spectrometer and a yield curve method similar to that used in this experiment, but no Compton scattering measurements were made. Here the liberty has been taken (with

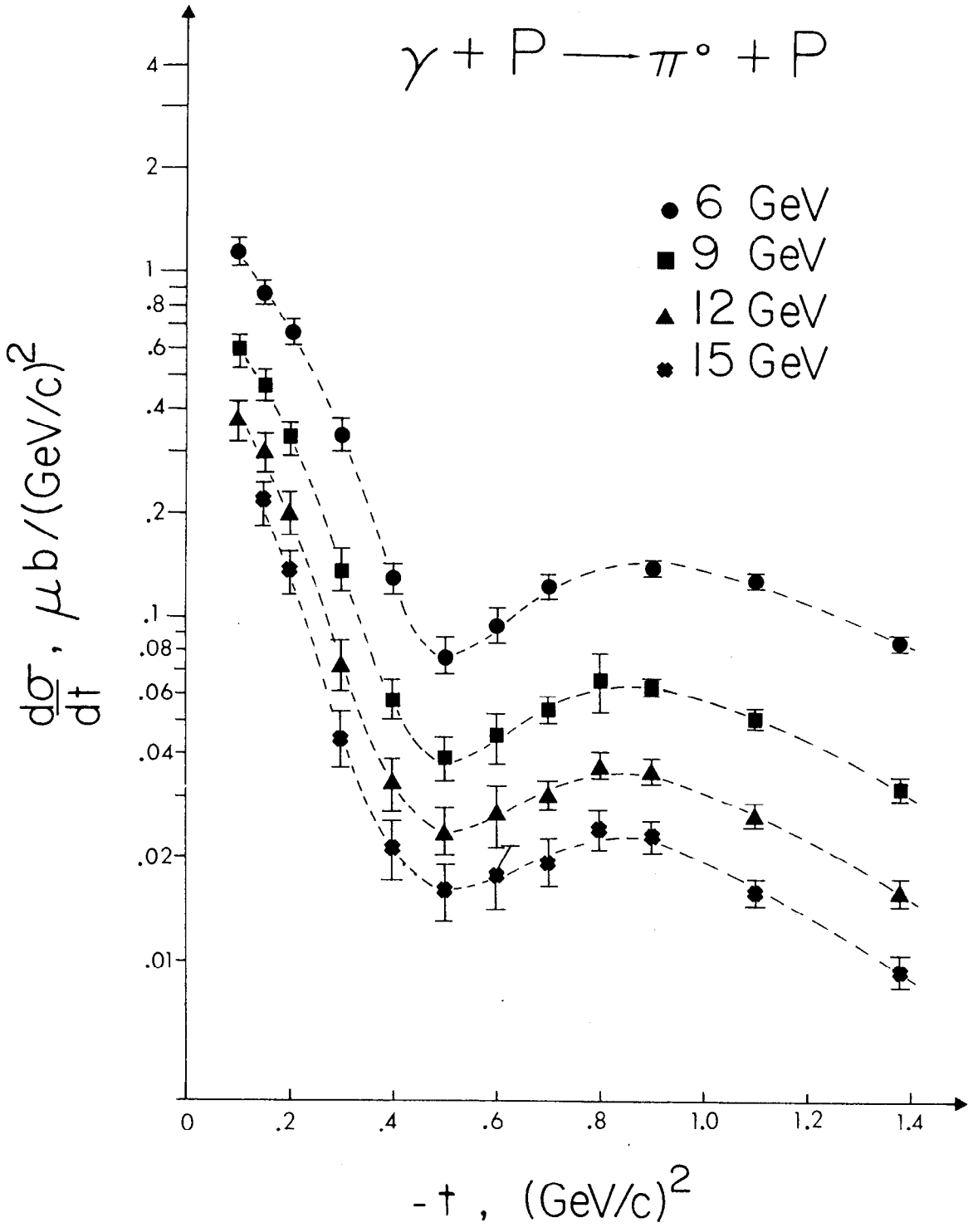

FIG. 17--π^0 angular distributions.

TABLE II

$\gamma + p \rightarrow \pi^o + p$ $\quad d\sigma/dt$, $\quad \mu b/(GeV/c)^2$

$\|t\|$, $(GeV/c)^2$	E_0 = 6 GeV	E_0 = 9 GeV	E_0 = 12 GeV	E_0 = 15 GeV
.1	1.13 ± .11	.59 ± .07	.37 ± .05	
.15	.86 ± .06	.47 ± .05	.30 ± .04	.22 ± .03
.2	.67 ± .05	.33 ± .04	.20 ± .03	.137 ± .020
.3	.34 ± .04	.138 ± .020	.073 ± .013	.045 ± .009
.4	.130 ± .014	.058 ± .008	.033 ± .006	.021 ± .005
.5	.078 ± .010	.039 ± .006	.024 ± .004	.016 ± .003
.6	.095 ± .012	.045 ± .008	.027 ± .006	.018 ± .004
.7	.122 ± .010	.054 ± .005	.030 ± .003	.019 ± .003
.8		.066 ± .013	.038 ± .003	.024 ± .003
.9	.140 ± .007	.063 ± .004	.036 ± .003	.0231 ± .0025
1.1	.129 ± .005	.051 ± .003	.027 ± .002	.0160 ± .0013
1.38	.0849 ± .0045	.0321 ± .0024	.0161 ± .0013	.0094 ± .0009

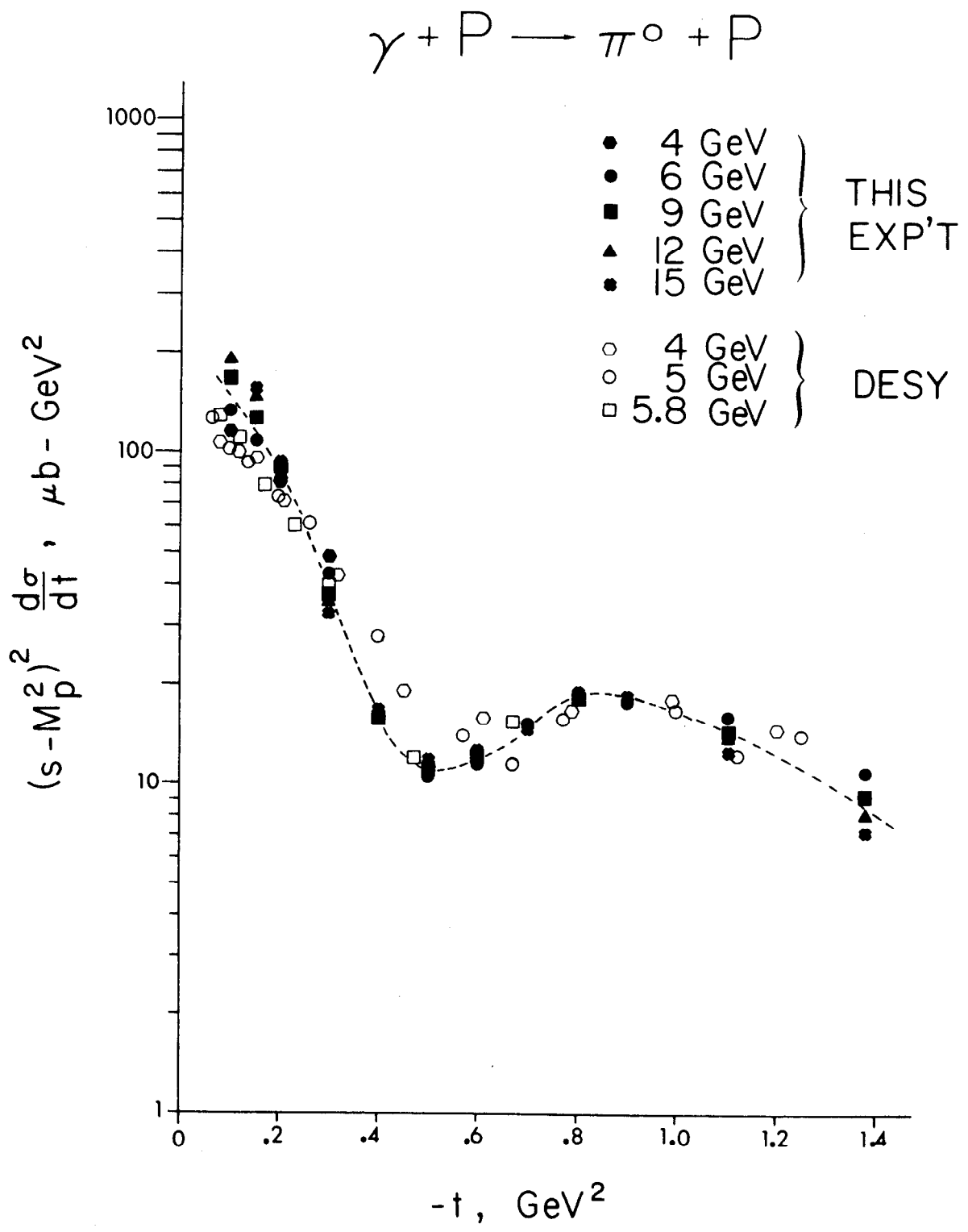

FIG. 18--Comparison with π^0 results from DESY.

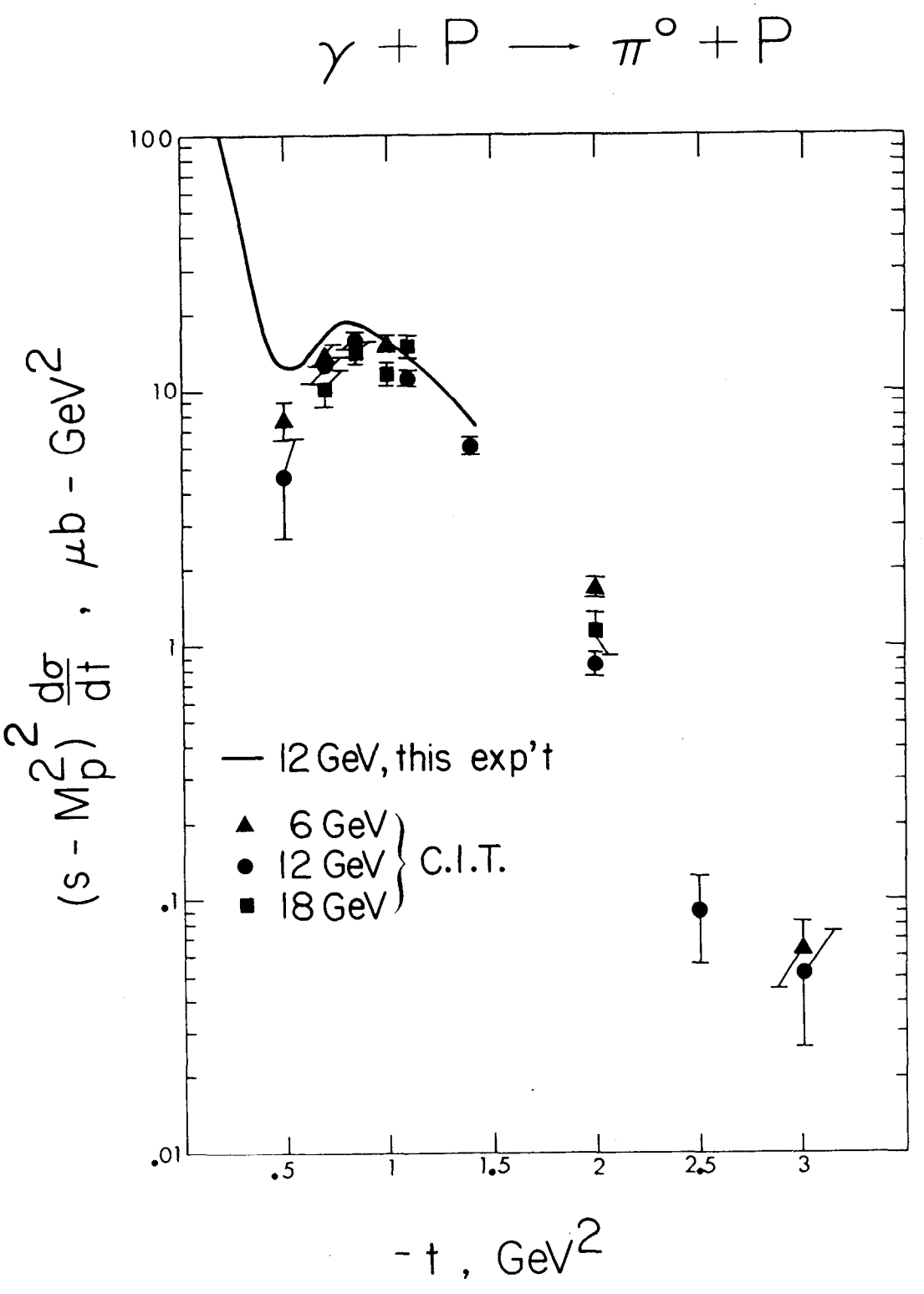

FIG. 19--Comparison with π^0 results from C.I.T.

their permission) of subtracting a correction for the Compton effect measured as described earlier. The solid line represents the 12 GeV π^o angular distribution from this experiment. For $|t| \geq 0.7$ the agreement is good with respect to the behavior of the cross section with t, and the CIT results show no further structure out to t=-3. However, there appears to be a normalization difference, which then invalidates a direct subtraction of the Compton cross sections, since they contain essentially the same normalization as the π^o in this experiment. This is especially evident at t =-0.5, where the Compton effect is the major contribution to the yield at high energies.

Figure 20 shows a comparison of the π^o results with a curve representing the 17 GeV Compton scattering cross sections. It is apparent that the Compton effect is a very important correction for $|t| \leq 0.6$ or so, but becomes negligible at low energies and high $|t|$.

B. η Results

The final cross sections for η photoproduction are given in Table III, and have been plotted versus t in Fig. 21. $d\sigma/dt$ has been multiplied by $\left(s-M_p^2\right)^2$, with the result that points at different energies fall together; thus the energy dependence appears consistent with E_0^{-2} for all t-values covered. The angular distribution shows a smooth decrease over the t-range studied, with no sign of a "dip" or local minimum around $t = -0.5$ $(GeV/c)^2$. The difference between this and the π^o behavior is quite striking.

Figure 22 shows a comparison of these values with recent (preliminary) η photoproduction results from DESY (Ref. 22) in the same t-range, also multiplied by $\left(s-M_p^2\right)^2$. To avoid confusion, and considering the agreement between energies in the previous figure, the results from this experiment have simply been averaged at each t. The agreement between the two experiments

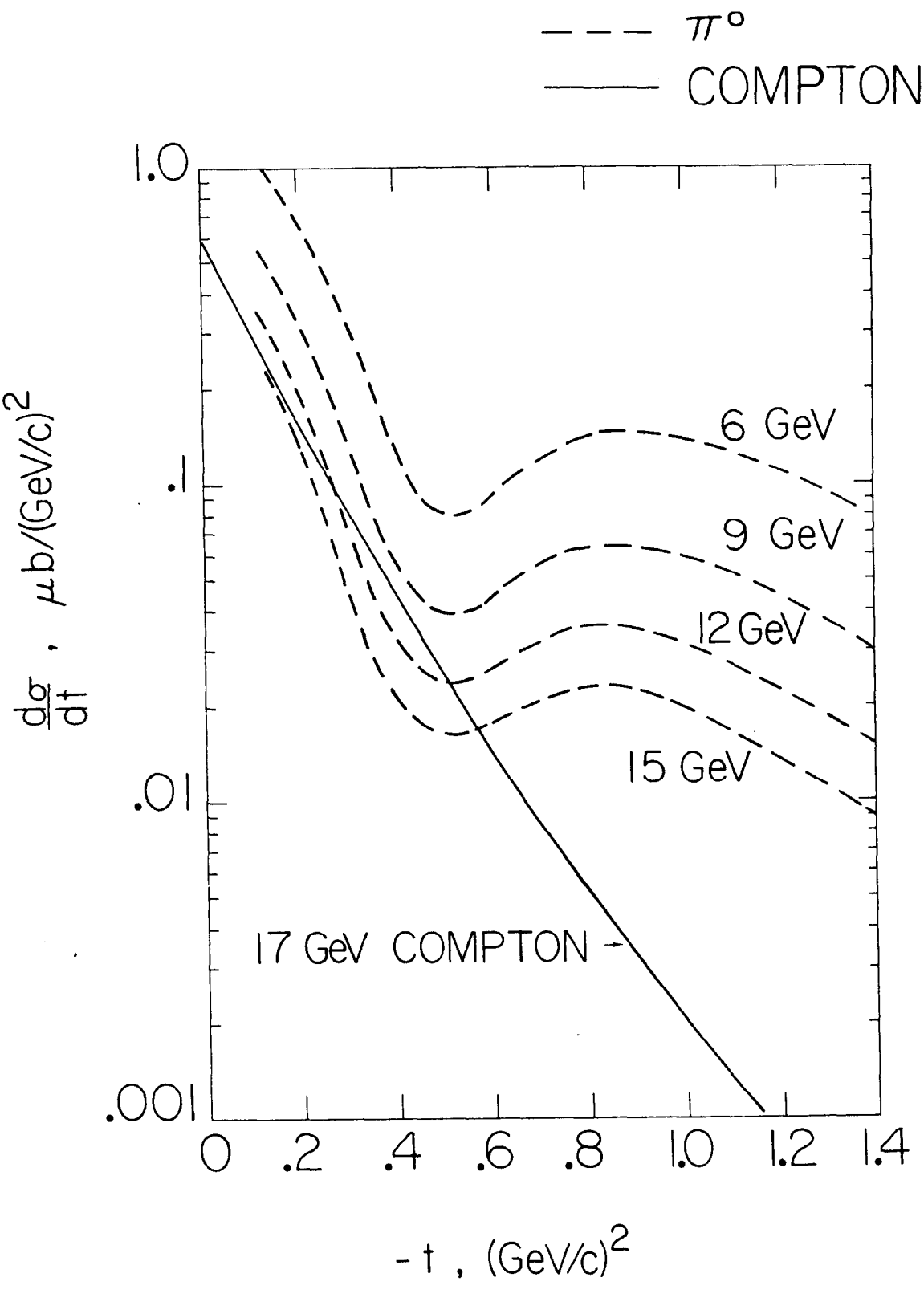

FIG. 20--Comparison with π^0 and Compton cross sections.

TABLE III

$\gamma + p \rightarrow \eta + p \quad \left(s-M_p^2\right)^2 \, d\sigma/dt \,, \quad \mu b\text{-}(GeV/c)^2$

$\lvert t \rvert$ $(GeV/c)^2$	4 GeV	5.5 GeV	6 GeV	6.5 GeV	9 GeV
.3	29 ± 8		30 ± 10		
.4)		21 ± 4.2		17 ± 7	
.5		13.9 ± 2.5		14.5 ± 5	
.7		9 ± 2		8.0 ± 1.6	7.2 ± 2.8
.9		3.9 ± 1.5		3.5 ± 1	3.9 ± 2
1.1			2.75 ± .8		2.6 ± 1.4
1.38				2.2 ± 1	1.95 ± 1

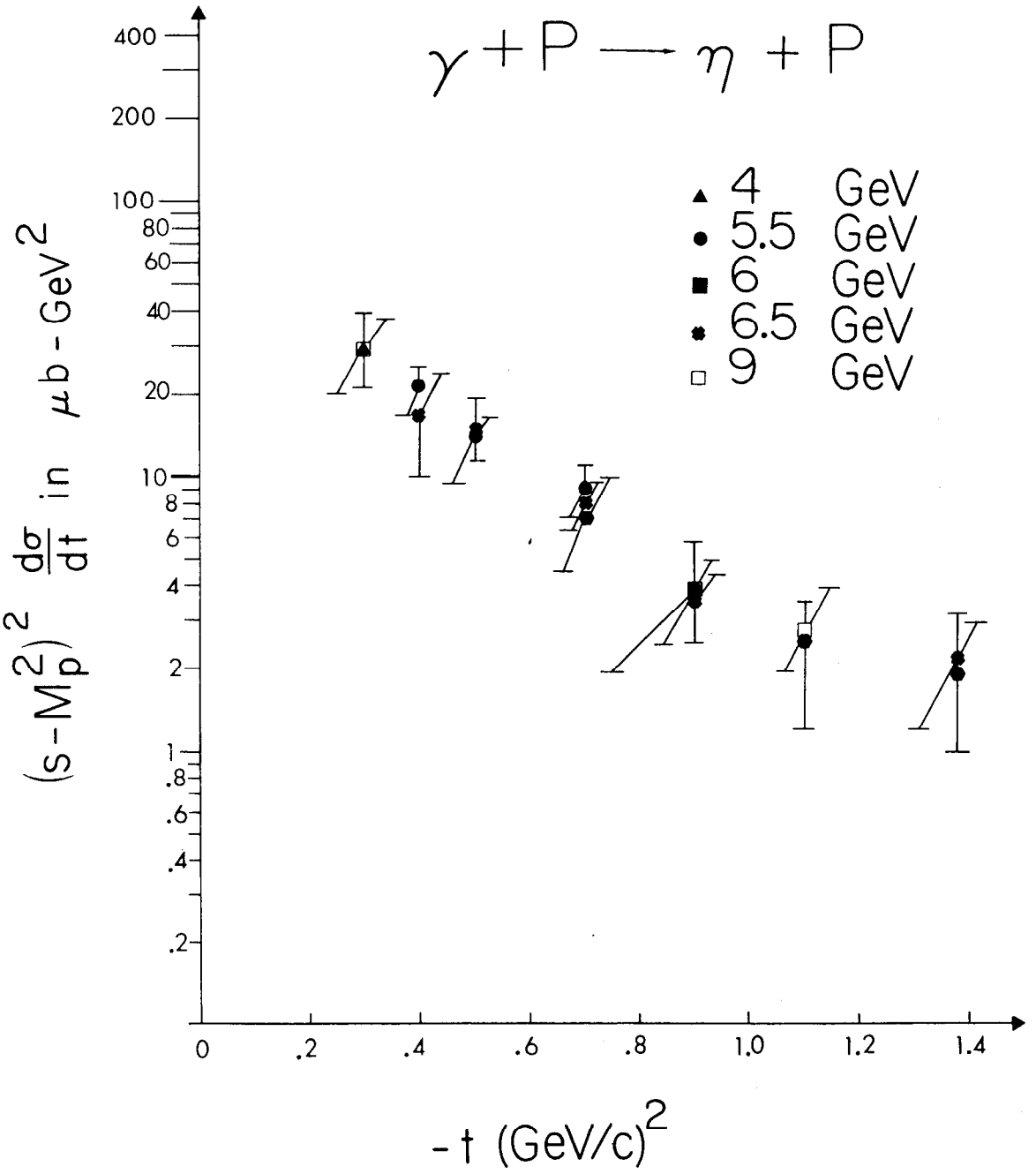

FIG. 21--Cross sections for $\gamma + p \rightarrow \eta + p$.

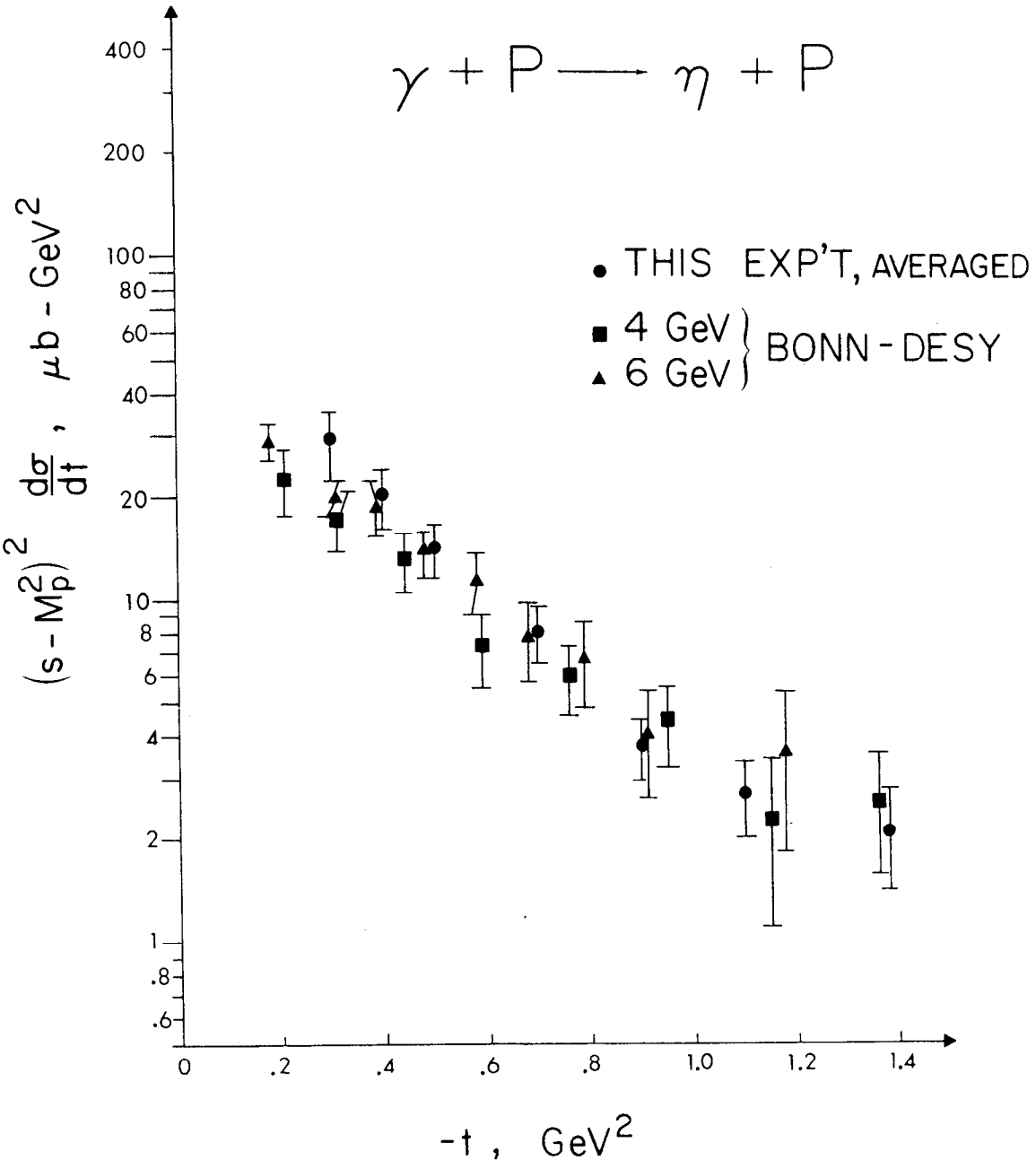

FIG. 22--Comparison with η results from DESY.

is remarkable. The DESY experiment was performed by detecting the η through its two-photon decay mode, thus the methods of the two experiments could hardly be less similar.

C. Discussion

The final π^o photoproduction results presented in this thesis have not been available long enough for theorists to have published any studies. However, a considerable amount of work has been done to develop models which would explain previously published results from other groups (Refs. 4, 5) and partial results from this experiment (Ref. 6), and the basic conclusions do not appear to have changed. Also, the η results given here are not essentially different from those presented in the previous publications.

As mentioned in the introduction, early models (Ref. 2) assumed "Reggeized" particle exchange alone would describe π^o photoproduction at forward angles. The ω meson was assumed to be the dominant exchange except near $t = -0.5$ $(GeV/c)^2$, where $\alpha_\omega = 0$ so that the amplitude was supposed to have a "nonsense zero". This predicted a "dip" in the cross section at $t = -0.5$, assumed to be partly filled in by contributions from exchange of B^o mesons (as mentioned in the introduction, only ρ^o, ω, ϕ, B^o exchanges are allowed, and of these the ρ also has $\alpha_\rho = 0$ near $t = -0.5$, and the ϕ contribution should be negligible). The dip was then expected to become more pronounced at higher energies, as the B^o exchange amplitude was thought to drop more rapidly than the ω. This model was in reasonable agreement with the data from DESY and CEA up to 6 GeV, but appears to be ruled out by higher energy results from this experiment. Figure 17 shows no very significant change in the appearance of the dip between 6 and 15 GeV, and the effective $\alpha(t)$ shown in Fig. 16 bears no resemblance to the accepted ω-trajectory ($\alpha_\omega = 0.45 + 0.9\,t$).

More successful fits have been obtained using models which include Regge cuts in addition to simple Regge particle exchange. In these models the cut terms fill in the dip. The simplest model is that proposed by Capella et al. (Ref. 23) and assumes only ω exchange plus a cut term corresponding to exchange of the Pomeranchukon P together with the ω, leaving five free parameters which are uniquely determined by a fit to the data. Work with this basic model has also been done at DESY (Ref. 20). Contogouris et al. (Ref. 24) achieved reasonable agreement with the data using a similar model, but with the values of the parameters calculated a priori under various assumptions. More complicated models have been introduced, including also ρ^0 exchange and a ρ-P cut, by Frøyland (Ref. 25) and by Henyey et al. (Ref. 26). Blackmon et al. (Ref. 27) assumed ω, ρ^0, and B^0 exchange with absorption, which is equivalent to including cuts. In general, all these models seem to be flexible enough to reproduce the basic features of combined π^0 photoproduction results, at least for $|t| \leq 1$ (GeV/c)^2.

η photoproduction has not been studied as extensively by the theorists. Predictions have been made using the vector dominance model to relate this process to other reactions. Dar and Weisskopf (Ref. 28) assumed only ρ^0 exchange to relate η photoproduction cross sections to those for the process $\pi^- + p \rightarrow \omega + n$. The data follow their prediction reasonably well for $|t| > 1$ GeV^2, at least with respect to the t-dependence. Gorczyca and Hayashi (Ref. 29) assumed ρ, ω, and B exchange, and used SU(3) in addition to vector dominance to make a connection between η photoproduction and strong vector meson production processes. Their prediction appears to deviate sharply from the measured results for $|t| > 0.7$ GeV^2, but is in reasonable agreement for smaller $|t|$.

Neither of these calculations explains why η photoproduction should look so different from π^o production. Ideally, the models used to describe the one process should work equally well for the other. The difficulty is that η photoproduction must not be dominated by particle exchange, since the largest contribution would be from the $\rho(\omega)$ and would result in a dip around $|t| = 0.5$ GeV^2. Fits have been made at DESY (Ref. 22) using a model assuming particle exchange plus cut, for both π^o and η production. The π^o fits required dominant particle (ω) exchange with only a correction from the cut; for the η, the cut term was forced to be by far the greatest contribution.

A natural qualitative explanation of the difference has been pointed out by Harari (Ref. 30). Some other reactions presumed to be dominated by ω or ρ exchange show dips at $t = -0.5$ GeV^2, still others do not, so the puzzle extends beyond this experiment. He notes that in every case a dip is correlated with a total dominant helicity flip equal to 1, and no dip with helicity flip 0 or 2. In absorption models the correction to a helicity flip 1 amplitude involves a J_1 Bessel function, but an absorbed amplitude of helicity flip 0 or 2 contains a J_0 Bessel function. For reasonable values of the interaction radius, the J_1 function will have a zero around $t = -0.5$ or -0.6 GeV^2, but the J_0 will not. This is then further evidence for the importance of including absorption or cuts in the calculation of π^o and η photoproduction and other processes.

APPENDIX

Consider observing a process $\gamma + p \rightarrow X^o + p$ having a differential cross section $d\sigma/dt$ for photon energy k and four-momentum-transfer-squared t, with a detection system accepting a range of azimuthal angles $\Delta\phi$ and a range of momentum transfers Δt about t. Then by definition, the yield of events from photons in an energy range dk about k, incident on a hydrogen target, is given by

yield = (number of incident photons in dk) $\times$

$$\text{(number of target protons/cm}^2\text{)} \times \left(\frac{d\sigma}{dt}\Delta t\right)\left(\frac{\Delta\phi}{2\pi}\right)$$

For a bremsstrahlung photon beam such as that used in this experiment, the number of photons in dk is given by

$$n(k)\ dk = EQ \times B(k, E_0) \times dk/k$$

where EQ is the number of incident equivalent quanta, defined as the total energy in the beam (measured by the SEQ in this case) divided by the endpoint energy E_0 (equal to the primary electron energy). $B(k, E_0)$ is the reduced bremsstrahlung function, equal to zero for $k > E_0$ and approximately unity for $k < E_0$. This function was calculated by the SLAC computer program BREM (Ref. 31) for the energies used in this experiment, and was typically about 0.93 at the tip.

The yield of recoil protons is to be calculated for one hodoscope counter in the focal plane of the 1.6 GeV/c spectrometer. $\Delta\phi$ is then determined by the vertical aperture to the spectrometer; t is defined by the spectrometer momentum setting p, and Δt by the acceptance $\Delta p/p$ of a hodoscope counter:

$$t = -2M_p T_p = -2M_p\left(\left(p^2 + M_p^2\right)^{1/2} - M_p\right)$$

$$\Delta t = (dt/dp)\ \Delta p = 2M_p p^2/E_p\ (\Delta p/p)$$

where M_p, T_p, and E_p are the protons' mass, kinetic energy, and total energy. The range of photon energies is then defined by the acceptance in proton production angle $\Delta\theta$ of the hodoscope counter: for a given missing mass M_x and recoil proton momentum, k is related to θ by equation (III.2)

$$k = \frac{|t| + M_x^2}{2(p \cos \theta - T_p)}$$

so that

$$\Delta k/k = 1/k\,(dk/d\theta)\ \Delta\theta = \frac{2kp \sin \theta\ \Delta\theta}{|t| + M_x^2} \quad .$$

The mass widths for π^o and η are ignored as being small compared to the experimental resolution. Here it is assumed that the hodoscope has been oriented along lines of constant k, as described in section III. The acceptances $\Delta p/p$ and $\Delta\theta$ of each counter are determined by its dimensions and the momentum and angle dispersions of the magnet; the product $(\Delta p/p)\ \Delta\theta$ is independent of hodoscope orientation.

Combining the factors discussed so far, the expression for the yield becomes

$$\text{yield} = EQ \times B(k, E_0) \times (\text{target protons/cm}^2) \times \frac{2M_p kp^3}{\pi E_p \left(|t| + M_x^2\right)} \times \frac{\Delta p}{p} \Delta\Omega \times d\sigma/dt \quad . \tag{A.1}$$

The effective target length viewed is given by the horizontal aperture to the spectrometer, divided by the sine of the spectrometer angle relative to the beam line (along which the target cylinder is aligned). Thus

$$\text{protons/cm}^2 = \frac{6.02 \times 10^{23}}{A_H} \times \rho \times \frac{L\ (\text{in cm})}{\sin \theta}$$

where A_H is the atomic weight of hydrogen (1.008), ρ is the density of the particular target (0.07 gm/cm^3 for liquid hydrogen, 0.01 gm/cm^3 for the gas target), and L is the horizontal spectrometer aperture (usually 6 or 7 inches).

If the relatively slow variation of 1/sin θ is ignored, the dependence of the yield on k (or θ) is found to be

$$\text{yield} \sim B(k, E_0) \times k \times \frac{d\sigma}{dt}(k)$$

for fixed p and M_x. Thus as a function of proton production angle, the yield in the hodoscope from photoproduction of π^o, for example, will show the "step" nature of $B(k, E_0)$ at threshold and for smaller angles (or energies) a variation chiefly due to the net energy dependence of $\left(k \frac{d\sigma}{dt}\right)$.

If the actual yield curve has been fit with the right functions and the rise in yield at a particular threshold has been extracted, this may be converted to a cross section by inverting the equation A.1. For the hodoscope counters in this experiment, $\frac{\Delta p}{p} \Delta\Omega = 0.85 \times 10^{-5}$ sr, and assuming a liquid hydrogen target and a horizontal spectrometer aperture of 6 inches, a typical conversion would be

$$\frac{d\sigma}{dt}(\text{in } \mu b/\text{GeV}^2) = 1.0 \times \frac{\pi E_p \sin\theta \left(|t| + M_x^2\right)}{M_p k p^3} \times$$

$$\text{step height in counts per } 10^{11} \text{ equivalent quanta .}$$

REFERENCES

1. T. Regge, Nuovo Cimento 14, 951 (1959) and 18, 947 (1960).
2. J. P. Ader, M. Capdeville, and Ph. Salin, Nucl. Phys. B3, 407 (1967).
3. D. Bellenger et al., Phys. Rev. Letters 21, 1205 (1968).
4. M. Braunschweig et al., Phys. Letters 26B, 405 (1968).
5. G. C. Bolon et al., Phys. Rev. Letters 18, 926 (1967).
6. R. Anderson et al., Phys. Rev. D1, 27 (1970).
7. R. L. Anderson et al., to be published.
8. SLAC Users Handbook;
   R. B. Neal, Physics Today 20, 27 (1967).
9. R. L. Anderson, Nucl. Instr. Methods 65, 195 (1968).
10. G. Fischer and Y. Murata, Report No. SLAC-PUB-605, Stanford Linear Accelerator Center (1969).
11. D. Horelick and R. Larsen, Report No. SLAC-PUB-398, Stanford Linear Accelerator Center (1968).
12. R. L. Anderson, Nucl. Instr. Methods 70, 87 (1969).
13. J. Grant and B. H. Wiik, to be published.
14. R. L. Anderson et al., Nucl. Instr. Methods 66, 328 (1968).
15. K. L. Brown et al., Report No. SLAC-91, Stanford Linear Accelerator Center (1970).
16. Power Designs Pacific, Inc., Palo Alto, California.
17. Chronetics, Inc., Mount Vernon, New York.
18. Transistor Specialties, Inc., Plainview, New York.
19. Scientific Data Systems, Santa Monica, California.
    A discussion of the use of this computer is given by D. B. Gustavson, Ph.D. thesis, Stanford University, December 1968.

20. M. Braunschweig et al., Report No. DESY 70/1, (January 1970).

21. R. Gomez, private communication.

22. K. Lübelsmeyer, private communication.

23. A. Capella and J. Tran Thanh Van, Nuovo Cimento Letters 1, 321 (1969).

24. A. P. Contogouris and J. P. Lebrun, Nuovo Cimento 64A, 627 (1969).

25. J. Frøyland, Nucl. Phys. B11, 204 (1969).

26. F. Henyey et al., Phys. Rev. Letters 21, 946 (1968); contributions to Daresbury Conference (1969).

27. M. L. Blackmon et al., Phys. Rev. 183, 1452 (1969).

28. A. Dar and V. F. Weisskopf, Phys. Rev. Letters 20, 762 (1968).

29. B. Gorczyca and M. Hayashi, Preprint TPJU 14/68.

30. H. Harari, "Photoproduction Mechanisms," Proceedings of the 4th International Symposium on electron and Photon Interactions, Liverpool (1969).

31. R. A. Early, Report No. SLAC-TN-66-15, Stanford Linear Accelerator Center (March 1966).